

# Status of the Heavy Photon Search Experiment at Jefferson Laboratory

P. Hansson Adrian, C. Field, N. Graf, M. Graham, G. Haller,  
R. Herbst, J. Jaros<sup>a</sup>, T. Maruyama, J. McCormick, K. Moffeit,  
T. Nelson, H. Neal, A. Odian, M. Oriunno, S. Uemura, D. Walz  
*SLAC National Accelerator Laboratory, Menlo Park, CA 94025*

A. Grillo, V. Fadeyev, O. Moreno  
*University of California, Santa Cruz, CA 95064*

W. Cooper  
*Fermi National Accelerator Laboratory, Batavia, IL 60510-5011*

S. Boyarinov, V. Burkert, A. Deur, H. Egiyan, L. Elouadrhiri, A. Freyberger, F.-X.  
Girod, V. Kubarovsky, Y. Sharabian, S. Stepanyan<sup>a,b</sup>, M. Ungaro, B. Wojtsekhowski  
*Thomas Jefferson National Accelerator Facility, Newport News, Virginia 23606*

R. Essig  
*Stony Brook University, Stony Brook, NY 11794-3800*

M. Holtrop<sup>a</sup>, K. Slifer, S. K. Phillips  
*University of New Hampshire, Department of Physics, Durham, NH 03824*

A. Fradi, B. Guegan, M. Guidal, S. Niccolai, S. Pisano, E. Raully, P. Rosier and D. Sokhan  
*Institut de Physique Nucleaire d'Orsay, IN2P3, BP 1, 91406 Orsay, France*

P. Schuster, N. Toro  
*Perimeter Institute, Ontario, Canada N2L 2Y5*

N. Dashyan, N. Gevorgyan, R. Paremuzyan, H. Voskanyan  
*Yerevan Physics Institute, 375036 Yerevan, Armenia*

---

<sup>a</sup>Co-spokesperson

<sup>b</sup>Contact person

M. Khandaker, C. Salgado

*Norfolk State University, Norfolk, Virginia 23504*

M. Battaglieri, R. De Vita

*Istituto Nazionale di Fisica Nucleare, Sezione di Genova e*

*Dipartimento di Fisica dell'Università, 16146 Genova, Italy*

S. Bueltmann, L. Weinstein

*Old Dominion University, Norfolk, Virginia 23529*

G. Ron

*Hebrew University of Jerusalem, Jerusalem, Israel*

P. Stoler, A. Kubarovsky

*Rensselaer Polytechnic Institute, Department of Physics, Troy, NY 12181*

K. Griffioen

*The College of William and Mary, Department of Physics, Williamsburg, VA 23185*

(Dated: May 7, 2012)

The Heavy Photon Search Test Run is the first stage of the Heavy Photon search experiment, which will search for a new heavy vector boson, aka "heavy photon", at Jefferson Laboratory. The HPS Test Run was approved by the Jefferson Laboratory PAC37 on January 14, 2011, and was subsequently approved and funded by DOE HEP. The Test Run apparatus has since been built, and was recently installed in Hall B, where it is currently running parasitically with the HDice experiment. In this Status Report, we summarize our progress over the past year in designing, constructing, installing, commissioning, and running the HPS Test Run Experiment. The technical challenges in mounting this experiment have been met. It remains to demonstrate that trigger rates and tracker occupancies agree with our simulations, which will substantiate our original reach estimates. We believe this will be possible with the parasitic run data we are just now taking, and plan to present results at the upcoming PAC39 meeting. With this data in hand, we will have satisfied the contingencies placed on approving full HPS by PAC37, and will request full HPS be approved.

## CONTENTS

1. Introduction	6
2. Motivations for Searching for Heavy Photons	8
2.1. Theory	9
2.2. Motivation	9
2.2.1. Heavy Photons and Dark Matter	9
2.2.2. Heavy Photons and Muon $g - 2$	13
3. HPS Physics with True Muonium	14
3.1. Motivation	14
3.2. HPS Prospects	14
4. Experimental Setup	18
4.1. Overview	18
4.2. Beamline Elements	20
4.2.1. Layout	20
4.2.2. Vacuum chambers	23
4.2.3. Targets	25
4.2.4. Beam Diagnostics	27
4.2.5. Running Conditions	28
4.3. Tracking and Vertexing System	31
4.3.1. Design Considerations	31
4.3.2. Detector Layout	31
4.3.3. Sensor Modules	33
4.3.4. Support, Cooling and Cabling	35
4.3.5. Power and Motion Control	37
4.3.6. Assembly, Testing, Shipping and Installation	37
4.4. Electromagnetic Calorimeter	38
4.5. Electronics and DAQ	40
4.5.1. SVT DAQ	42
4.5.2. ECal Front End Readout	44



	5
4.5.3. Trigger System	45
5. Simulation of Trigger Rates and Tracking Performance for Electron Running	48
5.1. Event Generation and Detector Simulation	48
5.2. Trigger Simulations	48
5.2.1. Geant4 simulations of the ECal	49
5.2.2. Hit Rates in the Calorimeter	51
5.2.3. Level 1 trigger simulations	53
5.3. Simulated Tracker Occupancies and Acceptance	57
5.4. Simulated Tracking Performance	61
5.4.1. Tracking Efficiency, Pattern Recognition and Fake Rates	62
5.4.2. Track Momentum and Spatial Resolution	62
6. Test Run Status	67
6.1. Parasitic Run Conditions	67
6.2. Experimental controls	69
6.3. Performance of the Test run Apparatus	71
6.3.1. SVT Calibrations	71
6.3.2. SVT Performance	74
6.3.3. ECal Calibration and Monitoring	76
6.3.4. ECal trigger calibration	78
7. Requested Action and Future Plans	81
References	84

## 1. INTRODUCTION

Our Proposal to Search for Heavy Photons at Jefferson Laboratory was submitted to PAC 37 in December, 2010 [1]. The proposal first explained the physics motivations for heavy photon searches, described the full HPS experiment, detailed the experimental design, and showed the reach of the experiment, evaluated in full Geant4 simulation. Second, it proposed a two-staged approach, the first stage, a test run, to demonstrate that the HPS technical approach was sound and to measure the actual tracker occupancies and trigger rates the full experiment would encounter. This would ensure that our reach estimates are realistic and give us valuable experience. The second stage would be the full HPS experiment. In January, PAC 37 approved the test run experiment and conditionally approved the full HPS, contingent upon the outcome of the test run experiment.

In recommending that HPS be conditionally approved (C2), PAC 37 approved and emphasized the need for the test run, and urged that it be completed before the 6 GeV shutdown. Regarding the conditions for approval, the PAC did make clear that the success of the test run should be at such a level that it essentially ensures that the proposed goals would be met and that only after a successful test run that demonstrates the needed detector capabilities, will full approval be appropriate.

Since that time, we have submitted a detailed Heavy Photon Search Test Run proposal to DOE HEP [2], which was reviewed March 1, 2011, approved in June, and funded in July. Work has been ongoing since then at both Jefferson Laboratory and SLAC, which have shared designing and constructing the apparatus with help from Orsay, Fermilab, and UC Santa Cruz. JLAB has developed the Ecal, Ecal DAQ, Ecal Trigger, some beamline elements, and the overall DAQ architecture. SLAC has developed the Silicon Vertex Tracker (SVT) and related systems, the SVT DAQ, SVT related beamline elements, and the overall simulation/reconstruction/analysis framework. As the DOE reviewers correctly commented, the construction schedule was quite aggressive, but a good deal of work and development at both JLAB and SLAC has led to a completed experiment, which arrived at JLAB in early April and was installed in Hall B on April 19, 2012. The HPS Test Run experiment was designed to be run with a dedicated electron beam, but JLAB has been unable to assign dedicated electron beam running because of a scheduling conflict with a previously approved experiment in Hall B, HDice. Accordingly, we have chosen to install the HPS Test

Run experiment to run parasitically with the HDice experiment, and make use of HDices photon beam to commission HPS and take data from photon conversions occurring just upstream of our apparatus in the Hall B pair spectrometer. The SVT tracker sits inside the vacuum chamber of the pair spectrometer, and the ECal, used to trigger it, resides just downstream. While photon running wont answer all our questions about full HPS running directly, it will allow a quantitative understanding of the tracker occupancies and provide detailed comparisons of simulated and actual trigger rates which can test our simulations and give confidence in our estimates of electron beam trigger rates.

Since at the time of writing this proposal, we have just begun our test run, we are not yet in the position to make the case for the approval of the full HPS experiment. We can show the considerable technical progress weve made, and do so below. While we cant present final performance data at this time, we have included some early results and we expect to present mature results at the time of the PACs meeting in mid June. We do not yet know with certainty if we will have a chance for electron beam running before the 6 GeV down, but we will do whatever is possible with photon beam running, to demonstrate how the HPS detector would perform in an intense electron beam. There are of course some aspects of running that we can only evaluate with an electron beam, e.g., experience with setting up small, stable beam spots with minimal halo or experience in moving silicon detectors very close to the beam. In fact, as discussed below, we have already demonstrated that Hall B can produce very small and very stable beam spots with essentially no halo. But of course we dont yet have direct experience putting our detectors very close to that beam.

Even if we are restricted to photon beam running, we expect to be able to make a credible case for full HPS approval. Necessarily, it will rely to some degree on Geant4 and EGS5 simulations, but these are well tested codes, and our dependence on them will be more qualitative than quantitative. These simulation codes have shown that the occupancy problems in the tracker occur only at the very smallest angles, and are due to multiply Coulomb scattered beam electrons. Our photon running includes conversions made in a thin target upstream of the HPS detector; the angular distribution of these electrons can be measured in the HPS test run, and is sensitive to this same multiple Coulomb scattering, and can therefore test our understanding of occupancy in the tracker. The simulation codes also indicate that most of the occupancy in the Ecal is due to these same multiply Coulomb scattered beam electrons. To the extent that we can demonstrate that we have accurately

modeled both the scattering and the response of the detector to high energy electrons which hit in and around the crystals, we demonstrate that our estimates of trigger rates in full HPS are accurate.

The physics case for heavy photons has been made extensively in our original proposal, and has recently been updated in the Intensity Frontier Workshop Proceedings. It was well received by PAC 37 and it has even garnered some attention at Workshops and in the press since then. In short, the physics case is alive and well and better known than it was at the time of the PAC37 meeting. For the sake of completeness, we include an overview and update of the physics case below.

In the remainder of this document, we summarize the status of the HPS Test Run beam-line and apparatus, review simulated trigger and tracking performance, present the status of our ongoing run, and make our request for full approval.

## 2. MOTIVATIONS FOR SEARCHING FOR HEAVY PHOTONS

HPS will search for heavy photons, called  $A'$ 's, which are new hypothesized massive vector bosons that have a small coupling to electrically charged matter, including electrons. The existence of an  $A'$  is theoretically natural and could explain the discrepancy between the measured and observed anomalous magnetic moment of the muon and several intriguing dark matter-related anomalies. As discussed in the following section, HPS should also have the capability to make the first detection of *true muonium*, a bound state of a  $\mu^+ - \mu^-$  pair predicted by Quantum Electrodynamics (QED).

The search for  $A'$ 's has generated enormous interest in the international physics community. This is evidenced, for example, by its inclusion in the recent Intensity Frontier Workshop [3] and by numerous experiments (in addition to HPS) proposed to search for them, including APEX [4, 5], MAMI [6], and DarkLight [7]. We briefly review the theory and motivation for heavy photons and then discuss updated reach estimates for the HPS  $A'$  search.

## 2.1. Theory

The  $A'$  is a new abelian  $U(1)$  gauge boson that has a weak coupling to electrically charged particles through “kinetic mixing” with the photon [8, 9]. Kinetic mixing produces an effective parity-conserving interaction  $\epsilon e A'_\mu J_{EM}^\mu$  of the  $A'$  to the electromagnetic current  $J_{EM}^\mu$ , suppressed relative to the electron charge  $e$  by the parameter  $\epsilon$ , which can naturally be in the range  $10^{-12} - 10^{-2}$  [10–13].

An  $A'$  allows ordinary matter to have a small coupling to new particles in a “hidden sector” that do not interact with the Standard Model’s strong, weak, or electromagnetic forces. These hidden sectors can have a rich structure and have thus far remained undetected. They appear in many extensions of the Standard Model, including string theory constructions [14–18] and are often required for mathematical consistency or phenomenological reasons. The photon mixing with the  $A'$  could provide the only non-gravitational window into their existence. HPS will be sensitive to  $A'$  masses between 10–800 MeV. Such  $A'$  masses can arise, for example, via the Higgs mechanism as in the models of [19–22].

Existing constraints [23] and the sensitivity of HPS are shown in Fig. 1.

## 2.2. Motivation

### 2.2.1. Heavy Photons and Dark Matter

The possible role of heavy photons in the physics of dark matter [25, 26] has provided an urgent impetus to search directly for heavy photons. Results from two classes of dark matter searches — “indirect” searches for galactic dark matter annihilation and “direct” searches for dark matter scattering off nuclei — have both been interpreted as potential signals of dark matter interacting through a heavy photon. Both fields have evolved in the last year, but not decisively. New astrophysical constraints have altered the favored parameter space for dark matter annihilation into heavy photons, but a significant region remains viable, and this overlaps considerably with the projected sensitivity of HPS. The motivation to test these theories of dark matter in a controlled laboratory experiment therefore remains strong. Several direct-detection experiments have published conflicting bounds on dark matter scattering, and putative signals. The physics of heavy-photon-mediated dark matter interaction was presented at some length in the proposal to PAC 37. Here we briefly summarize the

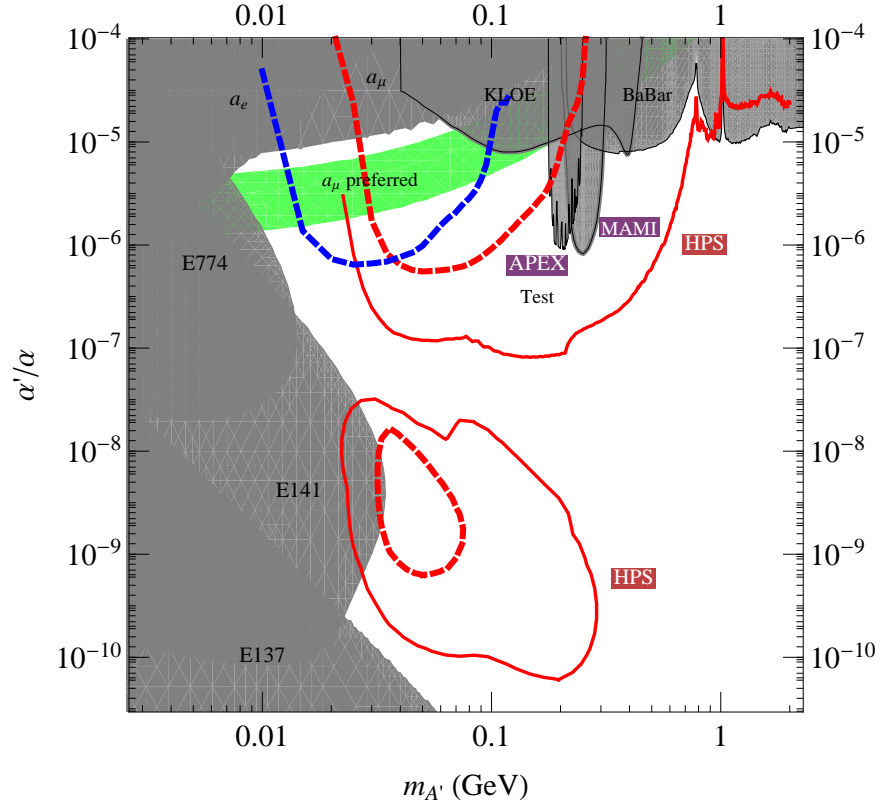


FIG. 1. Existing constraints on heavy photons ( $A'$ ) and the estimated HPS reach. Shown are existing 90% confidence level limits from the beam dump experiments E137, E141, and E774 [23, 58–60] the muon anomalous magnetic moment  $a_\mu$  [24], KLOE [61], the test run results reported by APEX [5] and MAMI [6], an estimate using a BaBar result [23, 62, 63], and a constraint from supernova cooling [23] (see also [64]). In the green band, the  $A'$  can explain the observed discrepancy between the calculated and measured muon anomalous magnetic moment [24] at 90% confidence level. Several projected sensitivities are shown for HPS. Solid red shows the  $2\sigma$  limits from the full HPS experiment, assuming 3 months of running time at each of 2.2 GeV (200 nA) and 6.6 GeV (450 nA). The upper region corresponds to a resonance search, the lower to a combined resonance plus vertexing search. Dashed red shows the limits from 1 week of running the HPS Test Run at 2.2 GeV (200 nA). The dashed blue limits corresponds to 1 week of running the Test Run at 1.1 GeV (200 nA).

status of dark matter and the case for its interactions with heavy photons, then discuss new observational constraints and theoretical developments.

The concordance model of big bang cosmology — the Lambda Cold Dark Matter ( $\Lambda$ CDM)

model — explains all observations of the cosmic microwave background, large-scale structure formation, and supernovae, see e.g. [27]. This model suggests that Standard Model particles make up only about 4% of the energy density in the Universe, while “dark energy” and “dark matter” make up 74% and 22%, respectively, of the Universe’s energy density. The concordance model does not require dark matter to have any new interactions beyond gravity with Standard Model particles. However, an intriguing theoretical observation, dubbed the “WIMP miracle”, suggests that dark matter does have new interactions. In particular, if dark matter consists of 10 GeV to 10 TeV particles interacting via an electroweak-strength force (weakly interacting massive particles or WIMPs), they would automatically have the right relic abundance consistent with the  $\Lambda$ CDM model.

If dark matter does interact with ordinary matter, it can interact in at least two ways: dark matter particles in the Milky Way Galaxy (and other bound astrophysical systems) can annihilate into visible matter, which could be detectable as energetic cosmic rays and/or gamma rays at Earth (indirect detection). Dark matter passing through Earth can also scatter off nuclear targets, causing the target to recoil. This recoil is observable in radio-pure detectors with sufficiently low background rates of nuclear recoil (direct detection).

The satellites PAMELA [28] and Fermi [29], the balloon-borne detector ATIC [30], the ground-based Cherenkov telescope HESS [31, 32], and other experiments have all reported an excess in the cosmic-ray flux of electrons and/or positrons above backgrounds expected from normal astrophysical processes. The evidence for this excess has only grown, with new measurements of the cosmic-ray electron flux by PAMELA [33] and confirmation by Fermi of the positron excess [34]. It is expected that results from AMS-II will eventually shed more light on the spectrum of these excess cosmic-rays. However, the origin of these excess positrons and electrons remains unknown. It may plausibly arise from any of three possibilities: pair creation in nearby pulsars, acceleration in supernova shocks, or dark matter annihilation or decay.

If the excess arises from dark matter annihilation, two features are incompatible with annihilation of “conventional” thermal WIMP dark matter charged under the Standard Model weak interactions, but compatible with an alternative explanation, namely that dark matter is charged under a new  $U(1)'$  and annihilates into  $A'$  pairs, which decay directly into electrons and positrons, and/or into muons that decay into electrons and positrons (see e.g. [25, 26, 35–37]):

- The annihilation cross-section required to explain the electron signal is  $50 - 1000$  times larger than the cross-section favored for the “WIMP miracle”. This can be explained if dark matter interacts with an  $\mathcal{O}(\text{GeV})$ -mass  $A'$ , which mediates a new moderate range force and enhances the annihilation rate at low velocities (the relative velocity of dark matter in the Galactic Halo,  $v \sim 10^{-3}c$ , is much lower than in the early universe, and the relative velocity in self-bound dark matter subhalos is lower still). We refer the reader to [38, 39] for a recent discussion.
- The PAMELA satellite did not see any anti-proton excess [40], which implies that, if dark matter annihilation is responsible for the positron/electron signals, it does not produce baryons. This contradicts expectations for dark matter annihilating through Standard Model interactions, but is expected if dark matter decays into light  $A'$ , which (for  $m_{A'} \lesssim \text{GeV}$ ) are kinematically unable to decay into protons and anti-protons.

Important constraints on the dark matter interpretation of these excesses arise from dark matter annihilation in other astrophysical systems (including dwarf galaxies [41], the outer Milky Way [42], Galactic Center (e.g. [43, 44] and references therein), and distant galaxies [44, 45] and clusters [46]), and in the epoch of atomic recombination in the early universe, which leaves an imprint in the cosmic microwave background radiation [47]. Unfortunately, the most sensitive of the astrophysical constraints are also quite dependent on numerous astrophysical uncertainties, including the gamma-ray background fluxes and the phase-space distribution of dark matter.

The status of models with light mediators ( $\lesssim 200 \text{ MeV}$ ), the target region for HPS, is particularly difficult to assess, because small, self-bound “subhalos” of dark matter with low velocity dispersions can easily enhance annihilation signals, both locally and in other galaxies. The enhancement from subhalos in distant galaxies strengthens constraints on  $A'$  models. On the other hand, local enhancement lowers the couplings needed to explain the Fermi and PAMELA excesses, and these lower couplings are in turn less constrained by other systems. Many analyses neglect the possibility of local subhalos, thereby overstating their exclusions of light  $A'$  models.

Fits to N-body simulations do appear to favor a significant local substructure component [3, 48, 49] which, in light  $A'$  models, would easily dominate the local cosmic-ray signal.

Accounting for substructure at the level suggested by e.g. [3], light- $A'$  regions easily avoid



constraints from the CMB, galactic center, dwarf galaxies, and dark matter self-interaction (though improved measurements of the CMB by Planck could severely constrain even these scenarios) [39]. Constraints on dark matter annihilation in distant galaxies (which would give rise to a diffuse and isotropic gamma-ray signal over the entire sky) are potentially severe even for these light- $A'$  models, but subject to theoretical uncertainties of several orders of magnitude. In summary, light- $A'$  models of dark matter annihilation are consistent with all other data, but their viability depends on aspects of the dark matter distribution that are not yet reliably understood.

The search for dark-matter-nuclear scattering has also seen considerable developments recently, but remains equally ambiguous. Three experiments have reported excesses that *may* be attributable to dark matter: DAMA/Libra [50]; CoGeNT [51], which also reported an annual modulation signal [52], and CRESST [53]. While these experiments' signals are most readily attributed to light dark matter ( $\sim 10$  GeV), results from CDMS [54], XENON10 [55], and XENON 100 [56] appear to exclude the same parameter regions. Some model parameter space remains moderately consistent with all of these results [57]. Though the evidence for light dark matter is spotty, it does raise a puzzle: dark matter with such low masses and high couplings cannot easily interact through Standard Model forces (such as  $Z$  exchange), without being excluded by measurements of the total  $Z$  width at LEP. If indeed dark matter is light, then it seems most likely to interact through a new mediator, a possibility that HPS will probe.

### 2.2.2. Heavy Photons and Muon $g - 2$

Besides being theoretically natural and having a possible connection to dark matter, an  $A'$  could explain the discrepancy between the measured and calculated value of the anomalous magnetic moment of the muon ( $a_\mu = g - 2$ ) [24]. This long-standing puzzle has several possible resolutions, but among the simplest new physics explanations is the existence of a new force mediator that couples to muons, like the  $A'$ . The contribution to  $a_\mu$  of the  $A'$  is like that of the photon, but suppressed by the mixing parameter  $\epsilon^2$  and dependent on the  $A'$  mass. The green region in Fig. 1 is the  $2\sigma$  band in which the  $A'$  can explain the discrepancy. This is an intriguing region, which the HPS experiment will probe.

### 3. HPS PHYSICS WITH TRUE MUONIUM

The proposed HPS experiment has the potential to discover “true muonium”, a bound state of a  $\mu^+\mu^-$  pair, denoted here by  $(\mu^+\mu^-)$ . In this section, we review the motivation for such a search and discuss the experimental design considerations.

#### 3.1. Motivation

Positronium and muonium, bound states of  $(e^+e^-)$  and  $(\mu^+e^-)$  pairs, respectively, have been produced and studied [65–67], but true muonium has not yet been detected (see e.g. [68–78]). Together with tauonium  $(\tau^+\tau^-)$  and tau-muonium  $(\tau^\pm\mu^\mp)$ , true muonium is among the most compact pure QED systems. While  $(\tau^+\tau^-)$  and  $(\tau^\pm\mu^\mp)$  are difficult to detect since the  $\tau$  has a weak decay that competes with the QED decay, the  $\mu$  is very long lived so that the decay of true muonium is purely a QED process.

The detection of true muonium would be a significant discovery and would constitute a further important test of QED. A number of applications of true muonium measurements have been highlighted in [70], designed to exploit true muonium as a perturbative laboratory for QCD bound state physics. These include measuring dissociation cross-sections as a function of energy and lifetimes of the various states. More speculatively, the discrepancy between theory and experiment for  $g - 2$  of the muon [79] and the discrepant measurement of the charge radius of the proton using muon bound states [80] suggest that further measurements of muon properties would be useful to resolve these puzzles.

#### 3.2. HPS Prospects

We expect that HPS will discover the 1S, 2S, and 2P true muonium bound states with its proposed run plan. The detection of these states should demonstrate the capability of the HPS experiment to identify rare separated vertex decays, and will provide a natural calibration tool for improving searches for heavy photons. We will discuss how HPS can reach this first milestone, and comment on possible follow-up measurements of true muonium properties.

The  $(\mu^+\mu^-)$  “atom” can be produced by an electron beam incident on a target such as tungsten [68, 69], although we will see below that high Z targets are not required. The

$(\mu^+\mu^-)$  atom is hydrogen-like, and so has a set of excited states characterized by a principal quantum number  $n$ . The binding energy of these states is  $E = -1407 \text{ eV}/n^2$ .

Relative to the  $n=1$  state, production cross-sections scale as  $1/n^3$ , so that higher- $n$  states will be more difficult to produce [70]. In practice, only the  $n=1, 2$  states will be important for this discussion. The  $n=1$  state is produced either in a triplet or singlet state, which have very different decay properties. The singlet states decay to  $\gamma\gamma$  with a proper lifetime  $\tau$  of  $0.602 \text{ n}^3 \text{ ps}$ , or  $c\tau = 0.181 \text{ n}^3 \text{ mm}$ , while the triplet states decays to  $e^+e^-$  with  $\tau = 1.81 \text{ n}^3 \text{ ps}$ , or  $c\tau = 0.543 \text{ n}^3 \text{ mm}$ . The triplet state thus decays exactly like an  $A'$  and can be searched for in the same way. Of course, since its mass is known to be  $2m_\mu$  within resolution, a precise search window can be specified. We will not consider the singlet state any further in this proposal, focusing exclusively on the triplet state. At the  $n=2$  level, triplet and singlet S and P states can be produced. The P state decays with a  $15.4 \text{ ps}$  lifetime to the  $n=1$  S state, while the  $n=2$  S state decays to  $e^+e^-$  in  $14.5 \text{ ps}$ . All of these lifetimes are approximately  $n^3 = 8$  times longer than the triplet  $n=1$  states.

As will be discussed in [81], the final production of the  $n=1$  triplet state depends directly on both the production and dissociation cross sections. The triplet production cross-section is given by [68]

$$\sigma_{triplet} = 1.20 Z^2 \frac{\alpha^7}{\mu_\mu^2} \left( 1.79 \ln \left( \frac{E_{beam}}{m_\mu} \right) \right) \quad (1)$$

$$\sim 6.2 Z^2 10^{-41} \text{ cm}^2 (\text{for } E_{beam} = 6.6 \text{ GeV}). \quad (2)$$

We see that this cross-section scales like  $Z^2$ . However, the true muonium bound state breaks up very easily inside the target with a dissociation cross-section that is not only very large but also scales like  $Z^2$  [68]

$$\sigma_{diss} \sim 1.3 Z^2 10^{-23} \text{ cm}^2. \quad (3)$$

This means that only the bound states produced in the last fraction of the target actually make it out of the target before breaking up, and that the total production rate is effectively independent of  $Z$ . The effective thickness through which muonium can penetrate is

$$t_b = \frac{1}{N\sigma_{diss}}, \quad (4)$$

where  $N$  is the number density of atoms in the target. The choice of target thickness is not an important parameter when designing an experiment to search for true muonium. Target thicknesses larger than  $t_b$  do not help to increase the production rate of true muonium pairs,

since those created at the beginning simply will not make it out the back end of the target before breaking apart. Note that for tungsten,  $t_b = 2.2\mu\text{m}$  (0.064% r.l.), while for Carbon graphite,  $t_b = 190\mu\text{m}$  (0.01% r.l.).

As discussed in [82], the production of  $n=2$  states is not dominated by primary production, but rather by secondary production where  $n=1$  states scatter into 2S and 2P states before leaving the target. This contribution is nearly an order of magnitude larger than primary production in any target thicker than  $t_b$ . For targets such as lead or tungsten, the total yields of 2S and 2P triplet states are approximately 10% that of 1S.

With the existing proposal, HPS will search for true muonium just as it does for heavy photons with separated vertices, requiring a vertex cut at about 1.5 cm to reject almost all QED background events, then searching for a resonance at  $2 m_\mu$ . An additional cut on the total energy of the  $e^+e^-$  pair of  $E_{e^-} + E_{e^+} > 0.8 E_{beam}$  will also be required for triggering.

Based on [81], the total production yield for 1S, 2S, and 2P (including secondary production) leaving a target of thickness  $t_b$  (or larger) and satisfying the above requirements is,

$$N_{(\mu^+\mu^-)} = 600 \left( \frac{I}{450 \text{ nA}} \right) \left( \frac{t}{3 \text{ months}} \right) \quad (5)$$

where a beam energy  $E_{beam} = 6.6 \text{ GeV}$ , and the nominal conditions of 450 nA beam current for 3 months ( $\sim 7.8 \times 10^6 \text{ s}$ ) on a single foil has been assumed. The vertices near the cut of 1.5 cm will be dominated by the 1S state, while a tail of vertices extending out beyond a few cm is dominated by 2S and 2P.

Accounting for all the efficiencies associated with a separated vertex search, we would expect to see about 60–100 true muonium events (we caution that the acceptance parameterization here is uncertain at the 50% level). The production of true muonium events can be increased in several ways. While increasing the target thickness does not help (as discussed above), the production rate scales linearly with both the current and the number of target foils (spaced by 2 or more cm so that true muonium decays between foils). Seeing the  $n=2$  state (which has a  $c\tau = 0.44 \text{ cm}$ ) will be more difficult, as we would produce only 10% as many of these states as of the 1S states. However, the large boosted decay length would increase the efficiency for detecting separated vertices, and many decays would be virtually background free, so that even a small number may be sufficient for detection.

The HPS experiment should be able to identify enough events to claim a discovery, and in addition, should be able to measure the mass of true muonium. There are certainly

other properties of true muonium that would be interesting to measure. A measurement of the lifetimes would be interesting, as the lifetimes are sensitive to physics that couples to leptonic currents. With enough statistics, it should be possible to perform a measurement of the lifetimes of the 1S, 2S, and 2P states; work is ongoing to investigate this possibility. With a dedicated target, dissociation cross-sections as a function of energy could be studied. And finally, if true muonium were produced in sufficient quantities, a Lamb shift measurement could be possible, which may constrain explanations of the proton charge anomaly. Work is ongoing to explore these possibilities.

## 4. EXPERIMENTAL SETUP

### 4.1. Overview

The HPS Test Run is a simplified, bare bones version of the full HPS apparatus, which has been described in detail in our proposal to PAC37 [1]. The HPS Test Run experiment was designed to demonstrate the technical feasibility of full HPS and confirm that backgrounds and trigger rates are as simulated and therefore manageable. The HPS Test Run is still powerful enough to provide real tracking and vertexing, reasonable acceptance, high rate data acquisition, and stand-alone physics capability. The HPS Test Run experiment has been designed to provide the proof of principle for the full HPS, and to have the potential to extend the search for heavy photons to as yet unexplored regions of parameter space.

Like the full experiment, the Test Run experiment ultimately relies upon the precision measurement of two quantities: the invariant mass of the  $A'$  decay products and the position of the decay vertex. By placing a tracking and vertexing detector immediately downstream of the target inside an analyzing magnet, the complete kinematic information required for  $A'$  reconstruction can be obtained from a single system, whose proximity to the target naturally maximizes the acceptance of a relatively compact detector and provides excellent momentum and vertexing resolution. A finely segmented, fast electromagnetic calorimeter, just downstream of the tracker, provides a powerful high rate trigger, identifies electrons, and augments the electron energy measurement. Very high rate data acquisition systems, for both the tracker and Ecal, make it possible to trigger and transfer data at 10s of kHz, and run with negligible dead time.

The Test Run Tracker replaces the six layer, 120 microstrip sensor design of the full experiment with a five layer system using just 20 sensors overall. Doing so has somewhat diminished the acceptance and tracking precision, but has retained excellent track finding, good momentum measurement, and good vertexing capability. Placement of the detectors mimics that of the full design. Placing the planes of the tracker in close proximity to the target means that the primary beam must pass directly through the middle of the tracking detector. For standard electron beam running, this has necessitated that the sensors don't encroach on a dead zone, where multiple Coulomb scattered beam particles and radiative secondaries are bent into a horizontal plane, the so-called "wall of flame". However, since

the energy released in the decay of a low mass  $A'$  is small relative to its boost, the opening angle between decay daughters can be quite small. To maximize the acceptance for low mass  $A'$ s, the vertical extent of the dead zone must be minimized and sensors placed as close as possible to the beam, so our design incorporates precision movers that can bring the silicon detectors to the required positions. Since interactions of the primary beam with air or even helium at atmospheric pressure gives rise to low-momentum secondaries that generate unacceptable occupancies, we have chosen to place the entire tracking and vertexing system in vacuum, in the Hall B pair spectrometer's magnet vacuum chamber. Running high speed silicon module readout in vacuum further requires a vacuum compatible cooling system, and data and power vacuum feedthroughs. All these features are incorporated in the apparatus we've constructed, as described below.

High luminosities are needed to search for heavy photons with small couplings and masses in the 100 MeV range. Utilizing CEBAFs essentially continuous duty cycle, the experiment can simultaneously maximize luminosity and minimize backgrounds by employing detectors with short live times and rapid readout. Silicon microstrip sensors are used in the tracker/vertexer because they collect ionization in 10s of nanoseconds and produce pulses as short as 50-100 ns. The sensors are read out continuously at 40 MHz using the APV25 chip, developed by the CMS experiment at the LHC. The Ecal  $\text{PbWO}_4$  crystals, reconfigured from the CLAS Inner Calorimeter, are read out by the APDs and amplifiers developed for the IC, and have similarly short pulse widths, so can also run at very high rates. The Ecal data is digitized in the JLAB FADC250, a 250 MHz flash ADC developed for the 12 GeV Upgrade detectors, but put to good use here and tested. The full analogue information from the FADCs coupled with the fine spatial information of the calorimeter is available to the trigger, which uses energy deposition, position, timing, and energy-position correlations to reduce the trigger rate to a manageable  $\sim 30$  kHz, in the electron beam mode. Like the tracker system, the electromagnetic calorimeter is split to avoid impinging on the dead zone. The beam and radiative secondaries pass between the upper and lower ecal modules, which are housed in new temperature-controlled enclosures, needed to stabilize the energy calibration.

The HPS test run was designed to run with 100 nA electron beam, but is presently installed in a parasitic mode with the HDice experiment, and utilizes their photon beam for initial checkout. In this configuration, the nominal HPS target, which is located just 10 cm

upstream of the first silicon layers, is fully withdrawn, and a  $\sim 0.2\%$  radiator is inserted into the photon beam roughly a meter upstream of the silicon, at the harp location. This radiator is used by HDice to convert a small fraction of the incident photons for measurement in the pair spectrometer, as a cross-check of the photon beam energy. It doubles as a target for the HPS test run, where conversions generate electrons and positrons which can trigger the ECal and be measured in the tracker, albeit at very low rates compared to the electron beam running needed for heavy photon searching. In this parasitic mode, the silicon detectors are all retracted roughly 1 cm from the beam center. This keeps them from interfering with the photon beam, while at the same time making them sensitive to the multiple scattering of electrons produced in the target by photon conversions.

In the following, the various elements of the experiment are discussed in more detail, beginning with the beamline, continuing with the tracker/vertexer, electromagnetic calorimeter, data acquisition systems, trigger, and calibration system.

## 4.2. Beamline Elements

### 4.2.1. Layout

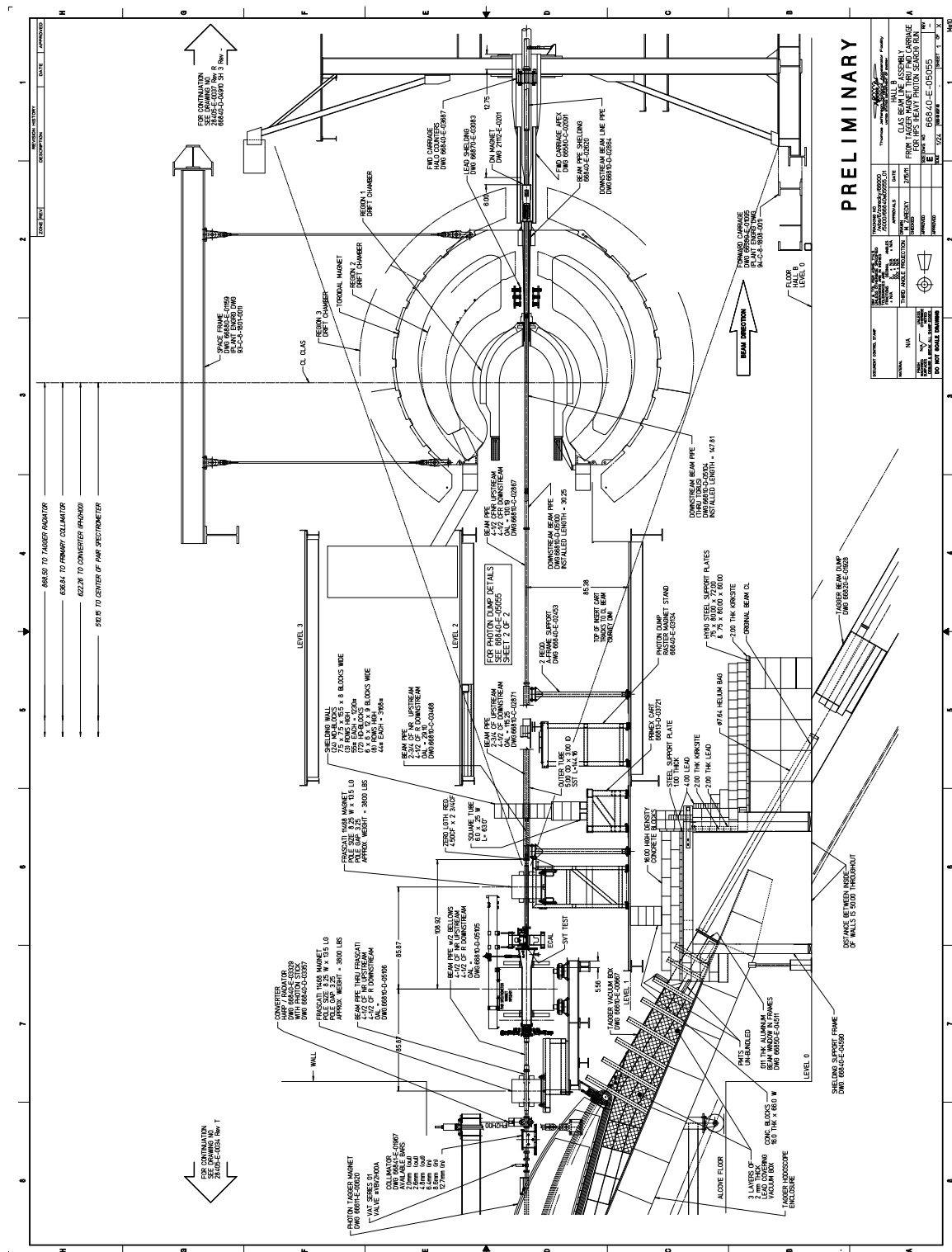
For electron beam running, the HPS Test Run experiment will use the same three magnet chicane that was used for the CLAS Two Photon Exchange experiment (TPE). The layout of the beam line and the chicane is shown in Figure 2. The Hall B pair spectrometer magnet, 18D36 (pole length 91.44 cm, max-field 1.5 T), will serve as the analyzing magnet. The dipole field direction (Y) is perpendicular to the horizontal (XZ) plane. A Hall B Frascati H magnets (pole length 50 cm, max-field 1.2 T) will be used as the first and the last dipoles of the chicane. The analyzing magnet will be operated at a 0.5 T-m field. The two bending magnets will be set to 0.25 T-m fields. The distance between the centers of the magnets and the location of the chicane will be exactly the same as for the TPE run. The only change that will be made to the TPE chicane layout is a transverse displacement of the analyzing magnet by about 4 inches (to beam left) in order to optimize the detector acceptance for  $e^+$  and  $e^-$ , see Figure 3.

The detector package includes the Silicon Vertex Tracker, which is described below, and a foil target, which are mounted inside the existing pair spectrometer vacuum box in the



FIG. 2. Beam line configuration for the HPS test run with electron beams. Chicane configuration is similar to previously run CLAS experiment.

high field region of the analyzing magnet, see Figure 4. The target foil is positioned at the



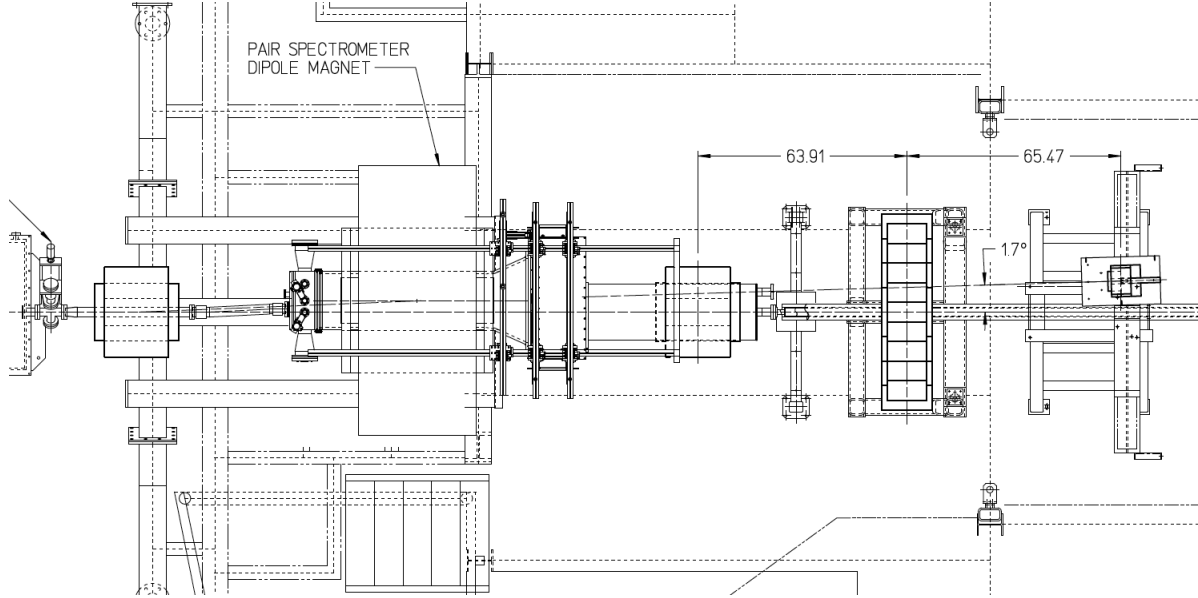


FIG. 3. Top view of the beam line configuration for the HPS test run with electron beams. The analyzing magnet is shifted by 4 inches to beam left to get optimal acceptance for both  $e^+$ s and  $e^-$ s.

upstream edge of the magnet's pole face. The distance from the target to the first layer of the silicon tracker is 10 cm, and to the face of the electromagnetic calorimeter downstream, 137 cm. There is continuous vacuum for the electron beam throughout the entire setup ending in the Hall B electron beam dump. The analyzing magnet, the Hall B pair spectrometer dipole, has its own power supply. The Frascati H magnets will use one common power supply that will be borrowed from the Hall B Moller polarimeter. There will be a shunt installed between the two Frascati magnets to allow independent small changes in currents on those two magnets (as it was done during the TPE experiment). Both power supplies are bipolar, so the magnets can be degaussed when needed.

The SVT vacuum box is mounted on the upstream end of the analyzing magnet vacuum chamber to provide connections for the SVT motion system, the cooling system, power and signal cables, and the target motion system. For electron running, the Ecal vacuum chamber is attached to the downstream end of the analyzing magnet vacuum chamber, above and below which are placed the Ecal modules. Downstream of the Ecal vacuum chamber, another vacuum chamber is attached, leading through the downstream chicane magnet. For the beam line upstream of the SVT vacuum box and downstream of the chicane magnet,

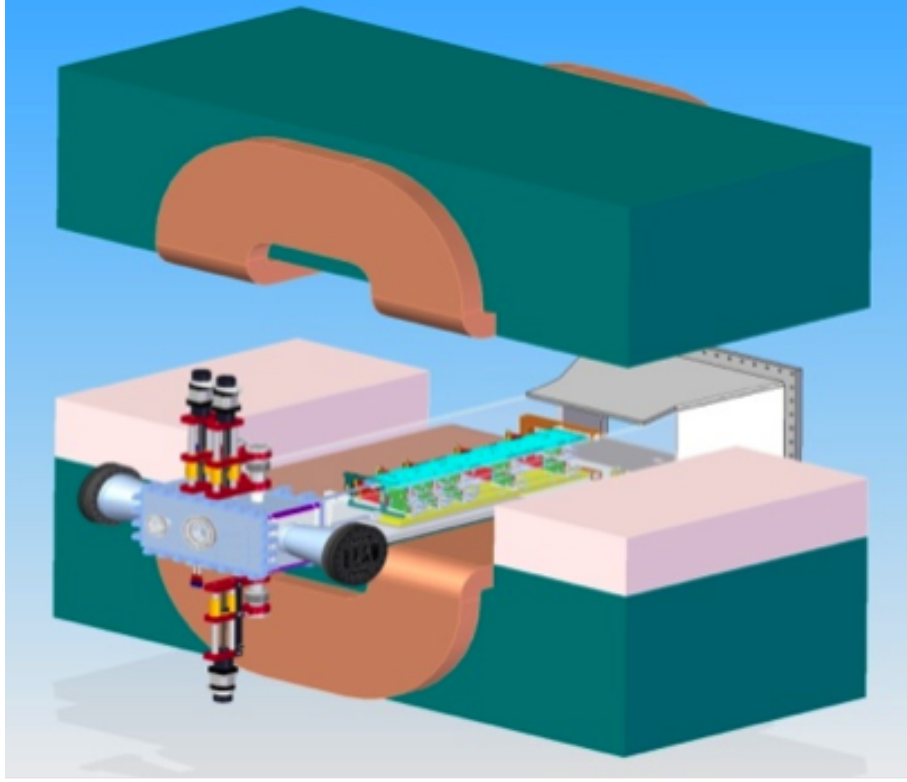


FIG. 4. Rendering of the SVT-vacuum chamber-magnet assembly.

the standard vacuum beam line of Hall B, with a few small modifications, will be used.

#### 4.2.2. Vacuum chambers

The SVT vacuum box, Figure 5, has been attached to the existing magnet vacuum chamber as shown in Figure 6. Two new flanges have been fabricated for it to accommodate connections to the upstream beampipe for either the parasitic photon run or for the electron run. Power, high voltage, and data signals to and from the hybrids are connected through two 8" flanges on the sides of the vacuum box, which each have six 50-pin vacuum rated D-connectors. Two vertical linear motion mechanisms driven by stepper motors are used to position the SVT upper and lower modules with a precision of  $1.25 \mu\text{m}/\text{step}$ . A third linear motion mechanism is used to position the target (Section 4.2.3) on or off the beam. All the stepper motors are placed at a large enough distance from the magnet to avoid any ill effect from the magnetic field. An existing stepper motor driver and EPICS-based control software are used. Two 2-3/4" flanges separately accommodate the cooling line feedthroughs for the

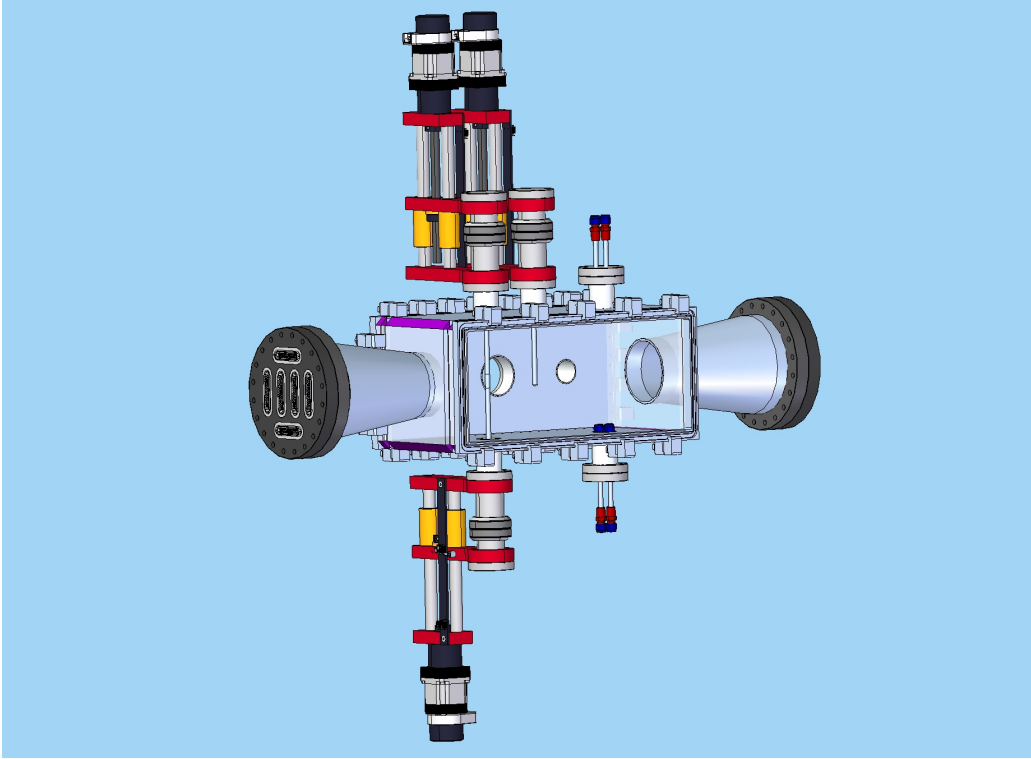


FIG. 5. Rendering of the SVT inside the Hall-B pair spectrometer vacuum chamber and the upstream vacuum box with SVT and target connections.

SVT upper and lower modules. The cooling line has a flow switch which is interlocked with the SVT power supply crate such that the power supply can be enabled only when cooling flow is present. The cooling line inlet and outlet temperatures are monitored and recorded.

For electron running, the scattering chamber between the top and bottom parts of the ECal is a critical beamline element. In order to keep the calorimeter as close as possible to the beam plane, include sufficient thermal insulation for the ECal (which must be temperature controlled), and maintain as wide a vacuum gap as possible, the top and bottom plates of the scattering chamber must be quite thin. At the location where the primary beams ( $e^-$  and  $\gamma$ ) exit, the openings in the chamber have been enlarged. In Figure 7 a rendering of the scattering chamber in between two halves of the ECAL is shown. The front flange of the chamber connects directly to the magnet vacuum chamber. Vacuum is maintained only on the electron side (beam right). This design is based on detailed GEANT4 simulations of background rates and acceptance of the ECal and allows crystals to be within 20 mm from the beam plane. Figure 8 shows how the vacuum chamber cavity meshes with the bottom

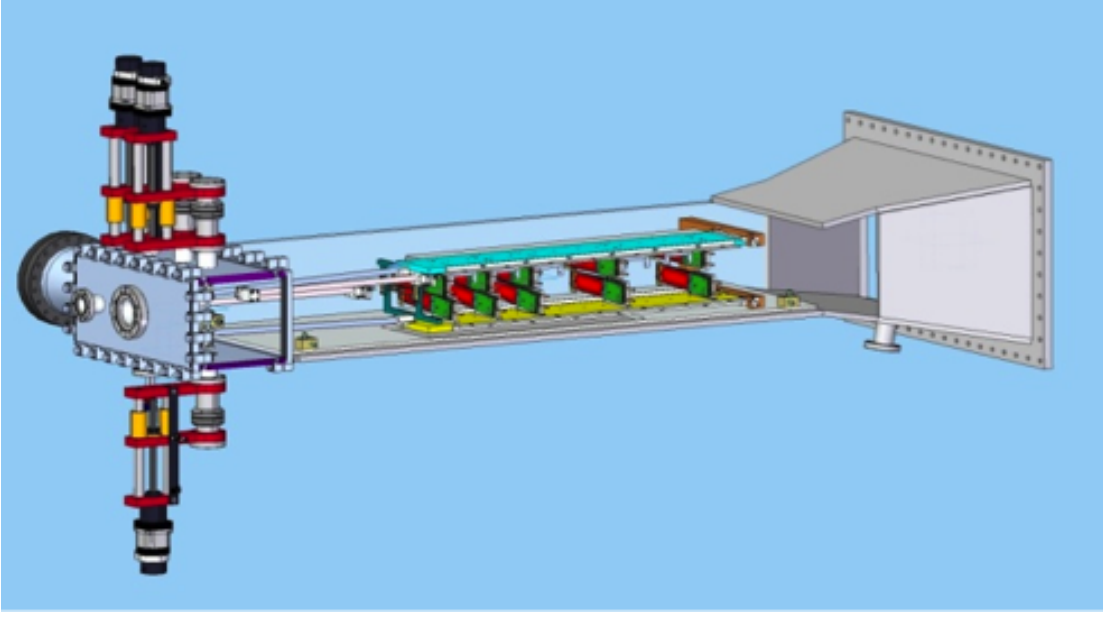


FIG. 6. Rendering of the SVT inside the Hall-B pair spectrometer vacuum chamber and the upstream vacuum box with SVT and target connections.

part of the ECal before the flanges were welded. In order to avoid excessive deformation of the thin walls of the vacuum chamber, an aluminum honeycomb support is inserted between the upper and lower walls, to beam's right.

#### 4.2.3. Targets

A thin tungsten foil is used as the target. High  $Z$  material is chosen for its short radiation length, to minimize the hadronic production relative to the electromagnetic trident and  $A'$  production. The target is located 10 cm in front of the first plane of silicon strip detectors. The primary target, 10 mm square, is 0.00125 radiation lengths (approximately 4 microns tungsten). Mounted immediately above it is a similar area of 0.0025 radiation lengths, available for some of the data taking, adjusting the beam current as appropriate.

The foil can be fully retracted from the beam, and is inserted on to the beam line from above, using a stepping motor linear actuator. The bottom edge of the foil is free-standing so there is no thick support frame to trip the beam when the target is inserted. Its position is adjustable vertically, allowing either thickness to be selected, and different sections of the tungsten can be used in the event of damage.

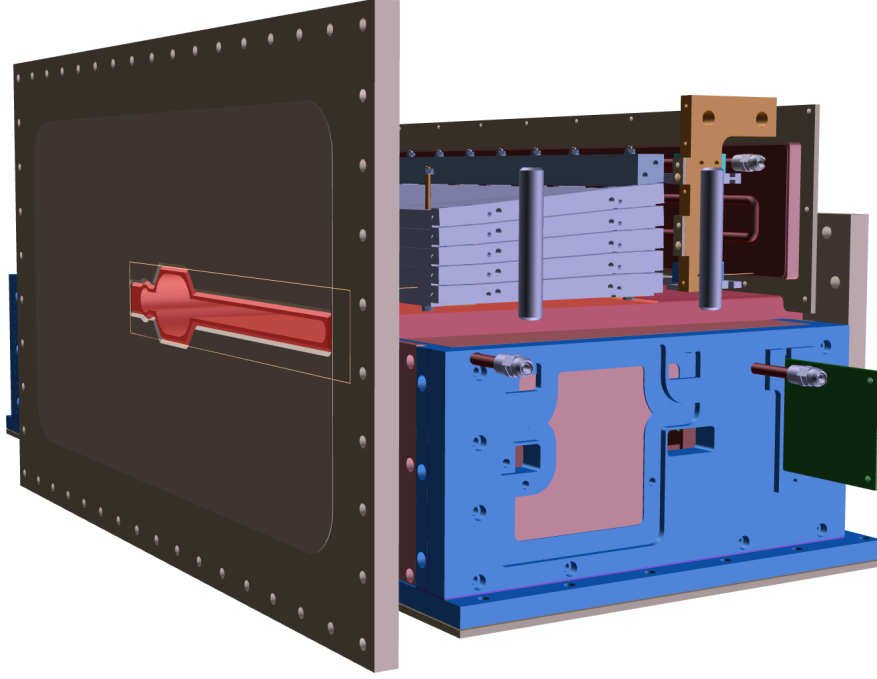


FIG. 7. Rendering of the ECal and the ECal vacuum chamber.

The target is designed to operate with beam currents up to 200 nA, which produce strong local heating. The strength of tungsten drops by an order of magnitude with temperature increases in the range of 1000 C. In addition, the material re-crystallizes above this range, which increases the tendency for cracking where thermal expansion has caused temporary dimpling. For these reasons, it was decided to keep the temperature rise below about 1000 degrees, which is accomplished by keeping the rms beam radius above 70 microns (for a round beam spot). However, a strongly elliptical beam spot is advantageous for constraining the vertex position during data analysis. A spot of, for example, 20 by 250 microns will also have an acceptable temperature rise.

In addition to the target, a set of tungsten beam-fiducial wires has been installed immediately in front of the silicon detectors. One horizontal wire, 20 micron diameter, and one 30 micron wire at 9 degrees to the horizontal, are mounted on a frame attached to the upper silicon support plate, and similarly for the bottom plate. The frames for the wires are wide enough that they do not occlude the silicon active area. The wires can be used to locate the position of the beam relative to the silicon. To accomplish this safely, the vertical separation between the front silicon sensor and its nearest wire is 8 mm. This separation,

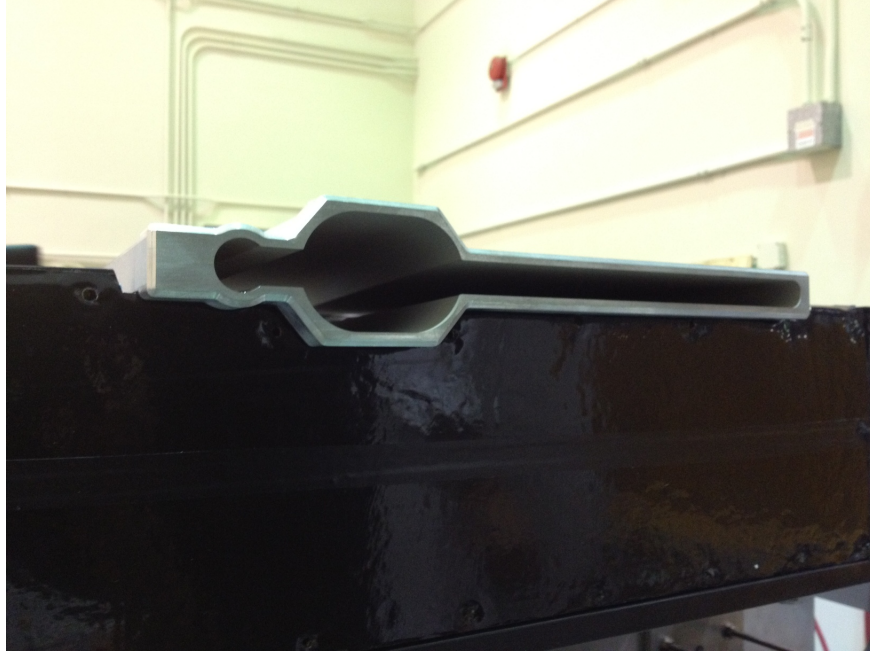


FIG. 8. Trial fit of the bottom ECal and the ECal vacuum chamber before welding of flanges.

and their small diameters, also means that, when the sensors are positioned for data taking, the wires have a negligible effect on acceptance.

The wires are also available for use as a fairly conventional wire scanner. In particular they can provide information about the minor and major axes, and the tip angle (roll), of a strongly elliptical beam

#### *4.2.4. Beam Diagnostics*

The HPS test run uses the Hall-B beam line as is. For electron running, beam position and current will be controlled by two sets of cavity beam position monitors (BPMs) that are located in the upstream tunnel. Sets of corrector dipoles and quadrupoles are routinely used to tune the beam for Hall B. A pair of BPMs will define the incoming trajectory of the beam and are included in the fast feedback loop. Readings from these BPMs will be used to maintain stable beam positions and currents.

The beam profile will be measured using two wire scanners, one installed in front of the first chicane dipole, another about 8 meters upstream. These two profilers will be used to establish the required beam parameters during setup. The wire scanner attached near the silicon modules and be used to check the beam profile at the target location.

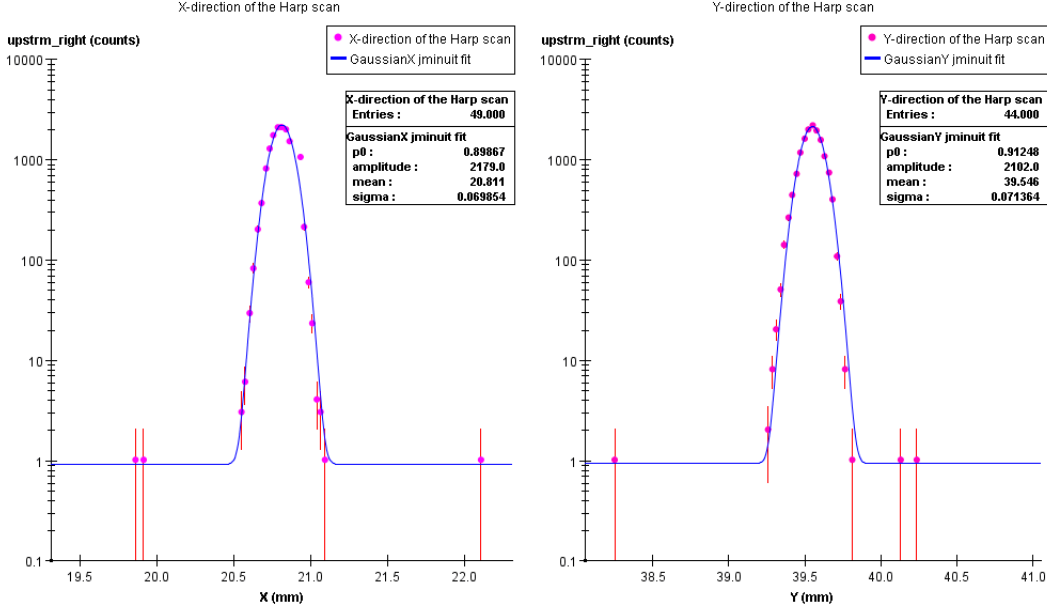


FIG. 9. Typical profile measured during one of electron beam experiments in Hall-B at 2.2 GeV.

A set of beam halo counters mounted along the beam line provides fast monitoring of the beam conditions. These counters are like those used for beam profile measurements. Excess noise in the beam halo counters triggers the machine fast shutdown system (FSD) in order to terminate beam in the event of beam excursions which could damage the HPS detectors.

#### 4.2.5. Running Conditions

For electron running, the HPS test run will use  $\sim 2.2$  GeV electron beam of up to 200nA incident on a tungsten (W) target. Operational experience shows that the CEBAF beam is very clean, and is contained within  $\pm 0.5$  mm with halo at the level of less than  $10^{-5}$ , so it will easily pass through the dead zone gap. In Figure 9 the beam profile measured using a wire harp during one of the recent CLAS experiments at 2.2 GeV is presented. Beam sizes of  $< 100\mu\text{m}$  are typical for the B-line. It should be noted that the profile measured with the wire scanner includes not only the actual beam size but also any  $> 100$  Hz beam motion.

The beam sizes routinely achievable in Hall B are suitable for much of the test run. However, for checking the vertexing performance and acquiring physics data, an asymmetric beam profile is desirable. Since the vertex resolution in the non-bend plane will be high, beam sizes of  $20 - 30\mu\text{m}$  in the Y direction are preferable. The momentum measurement



will not benefit from small beam sizes in the X direction, and small beam sizes in both dimensions will overheat the target foil. For these reasons the required beam sizes for full HPS will be  $\sigma_X \sim 250\mu m$  and  $\sigma_Y \sim 30\mu m$ .

The HPS beam parameter requirements are presented in Table I.

Parameter	Requirement/Expectation	Unit
E	2200	MeV
$\delta p/p$	$< 10^{-4}$	
Current	$< 200$	nA
Current Instability	$< 5$	%
$\sigma_x$	$< 300$	$\mu m$
$\sigma_y$	$< 40$	$\mu m$
Position Stability	$< 30$	$\mu m$
Divergence	$< 100$	$\mu rad$
Beam Halo ( $> 5\sigma$ )	$< 10^{-5}$	

TABLE I. Required beam parameters.

Since there was no experience with such small ( $20 - 30\mu m$ ) beam sizes, the optics program ELEGANT [83] was used to determine the optimized B-line parameters needed to achieve an asymmetric beam size at the HPS test run target location. Results of this optimization are presented in Figure 10. An asymmetric beam profile with  $\sigma_X \approx 250\mu m$  and  $\sigma_Y \approx 20\mu m$  is achievable.

Beam tests were conducted in Hall B to validate these optics simulations during the Two Photon Exchange experiment when 2.2 GeV beam was available (February of 2011). Parameters were set for a beam profile of  $\sigma_X \approx 300 \mu m$  and  $\sigma_Y \approx 10\mu m$  at the Hall B tagger beam profiler ( $\sim 8$  meters upstream of the proposed HPS target location). Several beam profile scans with different scanner speeds and data readout were performed to check for systematics. One of the scans is shown in Figure 11. As can be seen from the figure, the required profile can be reliably achieved. Several scans performed over two hours resulted consistent, stable beam profile. Based on the width of the Y-profile, beam position stability is  $< 20\mu m$ . Note: any beam motion with more than  $10 \mu m$  amplitude and faster than 1Hz is included in the scan.

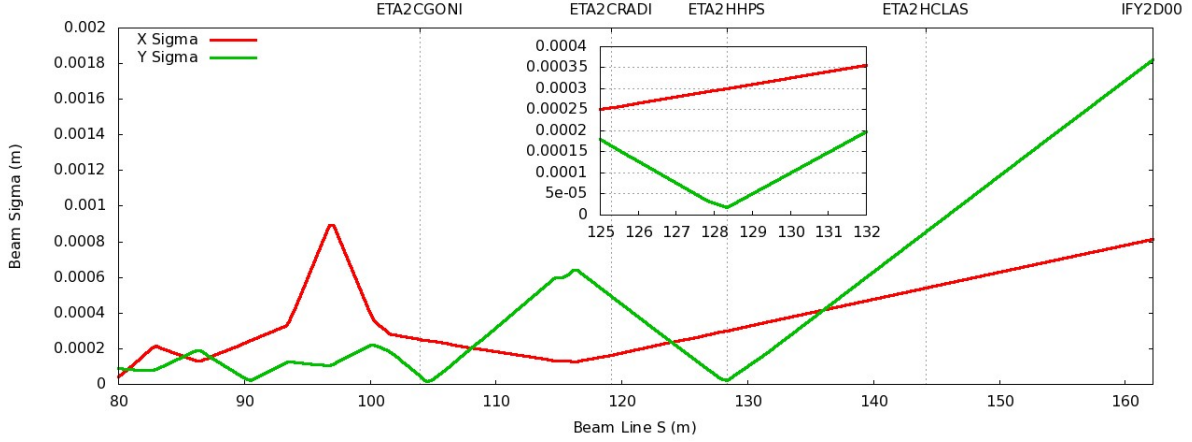


FIG. 10. Beam sizes in X and Y along the B-line in the upstream tunnel and in the region of the HPS test run setup. At the HPS target asymmetric beam profile  $\sigma_X = 300\mu\text{m}$  and  $\sigma_Y = 20\mu\text{m}$  can be achieved with existing B-line optics.

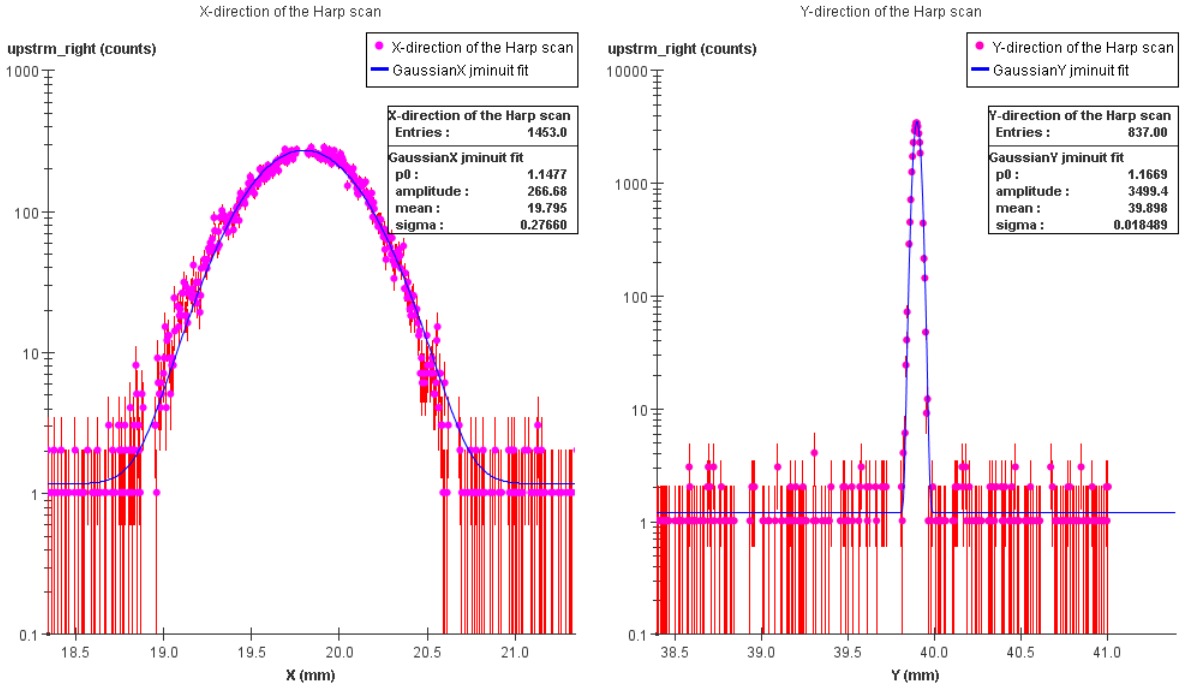


FIG. 11. Wire harp scan after loading optics parameters from optimization using ELEGANT program. The wire scan speed was 0.1mm/s, readout speed is 15Hz. Based on the width of the Y-profile, beam position stability is  $< 20\mu\text{m}$ . Note: any beam motion with more than  $10\mu\text{m}$  amplitude and faster than 1Hz is included in the scan.

### 4.3. Tracking and Vertexing System

#### 4.3.1. Design Considerations

Critical objectives of the test run are establishing that the tracker can be built as conceived and that the backgrounds it encounters are acceptable for the full experiment. The more ambitious goal of achieving sensitivity to a hidden sector photon with data from the test run naturally promotes these objectives and presents additional challenges. At the beam energies necessary to achieve sensitivity to  $A'$  in the interesting mass range, the decay products will be electrons with momenta on the order of a few GeV/ $c$ . Consequently, multiple scattering dominates the key measurement uncertainties for any feasible material budget and, for both the mass and vertexing resolutions, the radiation lengths of material must be minimized throughout the tracker. To minimize the impact of beam backgrounds, the tracker is split into upper and lower half-planes which avoid the “dead zone” defined by the beam envelope and those electrons which have radiated in the target. To avoid secondary backgrounds which would arise from the passage of the beam through gas, the beam must be transported in vacuum and the entire tracker placed within a vacuum chamber. Finally, the position and tails of the beam profile may not be exactly known and there are uncertainties in the background estimates and the radiation tolerance of the sensors for the background environment. So, it will be important to be able to adjust the position of the tracking planes remotely. It is also sensible to provide for access to the tracker with minimal intervention, to accommodate repairs or replacement of tracking planes.

#### 4.3.2. Detector Layout

The silicon tracking and vertexing detector for HPS Test, or SVT, operates in an existing vacuum chamber inside the pair spectrometer analyzing magnet in Hall B at JLab. The design principles of the SVT are described in further detail in the HPS Test Run Proposal [2]. There are five measurement stations, or “layers”, placed immediately downstream of the target. Each layer comprises a pair of closely-spaced planes and each plane is responsible for measuring a single coordinate, or “view”. Introduction of a stereo angle between the two planes of each layer provides three-dimensional tracking and vertexing throughout the acceptance of the detector with one redundant layer.

In order to accommodate the dead zone, the SVT is built in two halves that are mirror reflections of one another about the plane of the nominal electron beam. Each half consists of five double-sided modules mounted on a support plate that provides services to the modules and allows them to be moved as a group relative to the dead zone. Each module places a pair of silicon microstrip sensors back-to-back at a specified stereo angle with independent cooling and support.

The vacuum chamber being used for HPS Test cannot accommodate the 90-degree stereo layers planned for the full experiment to optimize the vertex resolution [1]. Instead, 100 milliradian stereo is used in the first three layers to provide higher-resolution 3-d space points for vertexing. The 50 milliradian stereo of the last two layers breaks the tracking degeneracy of having five identical layers and minimizes fakes from ghost hits, improving pattern recognition while still providing sufficient pointing resolution into Layer 3 for robust hit association in the denser environment there. The details of the five layers are shown in Table II and a solid model of the detector layout is shown in Figure 12. Figure 13 shows a photograph of both completed detector halves prior to final assembly. Altogether, this layout comprises 20 sensors and hybrids and 100 APV25 chips for a total of 12780 readout channels.

Layer	1	2	3	4	5
nominal $z$ , from target (cm)	10	20	30	50	70
Stereo Angle (mrad)	100	100	100	50	50
Bend plane resolution ( $\mu m$ )	$\approx 6$	$\approx 6$	$\approx 6$	$\approx 120$	$\approx 120$
Non-bend plane Resolution ( $\mu m$ )	$\approx 6$	$\approx 6$	$\approx 6$	$\approx 6$	$\approx 6$
# sensors	4	4	4	4	4
Nominal dead zone	$\pm 1.5$	$\pm 3.0$	$\pm 4.5$	$\pm 7.5$	$\pm 10.5$
Power consumption	6.9	6.9	6.9	6.9	6.9

TABLE II. Layout of the HPS SVT.

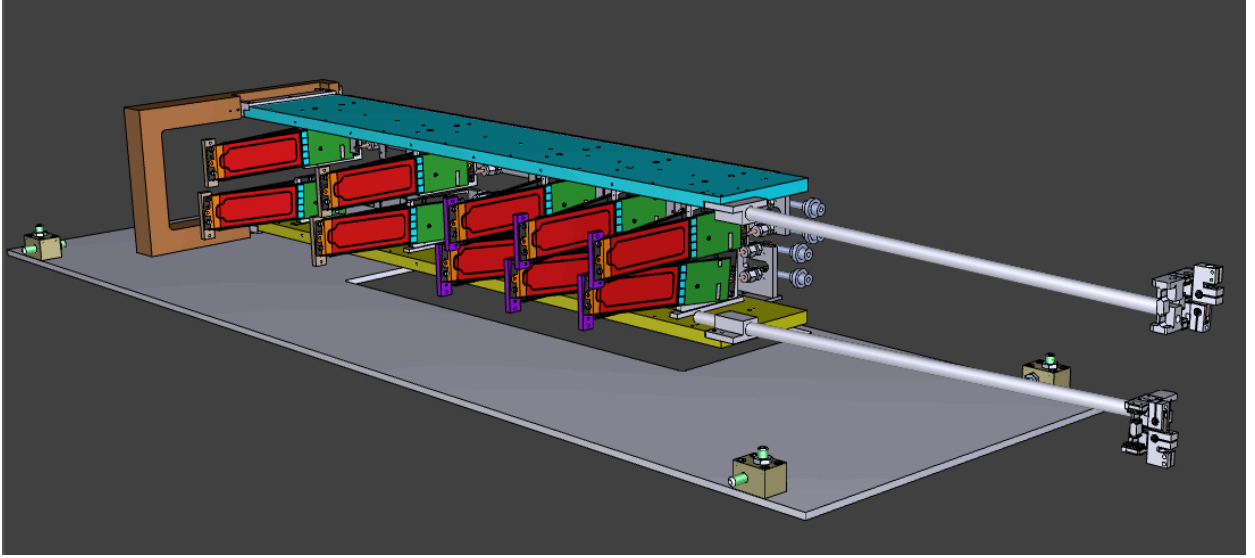


FIG. 12. A partial rendering of the HPS Test SVT solid model showing the modules of the upper and lower half-detectors on their support plates, the hinged C-support, the motion levers, the cooling manifolds on their strain relief plate and the baseplate with its adjusters. The sensors are shown in red and the hybrids in green. The beam enters from the right.

#### 4.3.3. Sensor Modules

The sensor modules for the SVT consist of a pair of identical half-modules, sandwiched back-to-back around an aluminum cooling block at one end and a similar PEEK spacer block at the other. Figure 14 shows a prototype module assembly. The cooling block provides the primary mechanical support for the module as well as cooling via copper tubes pressed into grooves in the plates. The spacer block defines the spacing between the sensors at the far end of the module, stiffens the module structure, and improves the stability of the sensor alignments.

Each half module consists of a single sensor and a hybrid electronic readout board glued to a polyamide-laminated carbon fiber composite backing. A window is machined in the carbon fiber leaving only a frame around the periphery of the silicon to minimize material. A  $50\ \mu\text{m}$  sheet of polyamide is laminated to the surface of the carbon fiber with 1 mm overhang at all openings to ensure good isolation between the backside of the sensor, carrying high-voltage bias, and the carbon fiber which is held near ground. The average support material in the tracking volume is approximately  $0.1\% X_0$  per double-sided module.



FIG. 13. Both halves of the HPS Test SVT fully assembled at SLAC.

The sensors are  $320\ \mu\text{m}$  thick,  $p^+$  on  $n$ -bulk,  $\langle 100 \rangle$ , single-sided microstrip sensors manufactured by the Hamamatsu Photonics Corporation for production of layers 2-5 of the DØ Run IIb silicon tracker. Of 33 sensors provided for the SVT, 29 had breakdown voltages in excess of 1000V and all but 4 had no bad channels.

The readout ASICs are the APV25 readout chip designed for the CMS experiment at the LHC. In addition to fast readout capability and high radiation tolerance, the APV25 is capable of delivering multiple samples of the amplifier output at a specified pipeline latency which allows asynchronous use of the chip as well as the ability to reconstruct hit time to 2 ns at our high signal-to-noise ratios [1]. Each 10-layer, polyamide hybrid readout board hosts a set of five APV25 and provides conditioned high-voltage for biasing the sensor. Power, control and data for the hybrids are connected via 30 lines of twisted pair wire: an 18 cm “pigtail” cable is soldered directly to the surface of the hybrid. Bias is provided to both top and back side via wire bonds which are also used to connect the front end reference to the carbon fiber. All wire bonds are encapsulated to prevent damage.



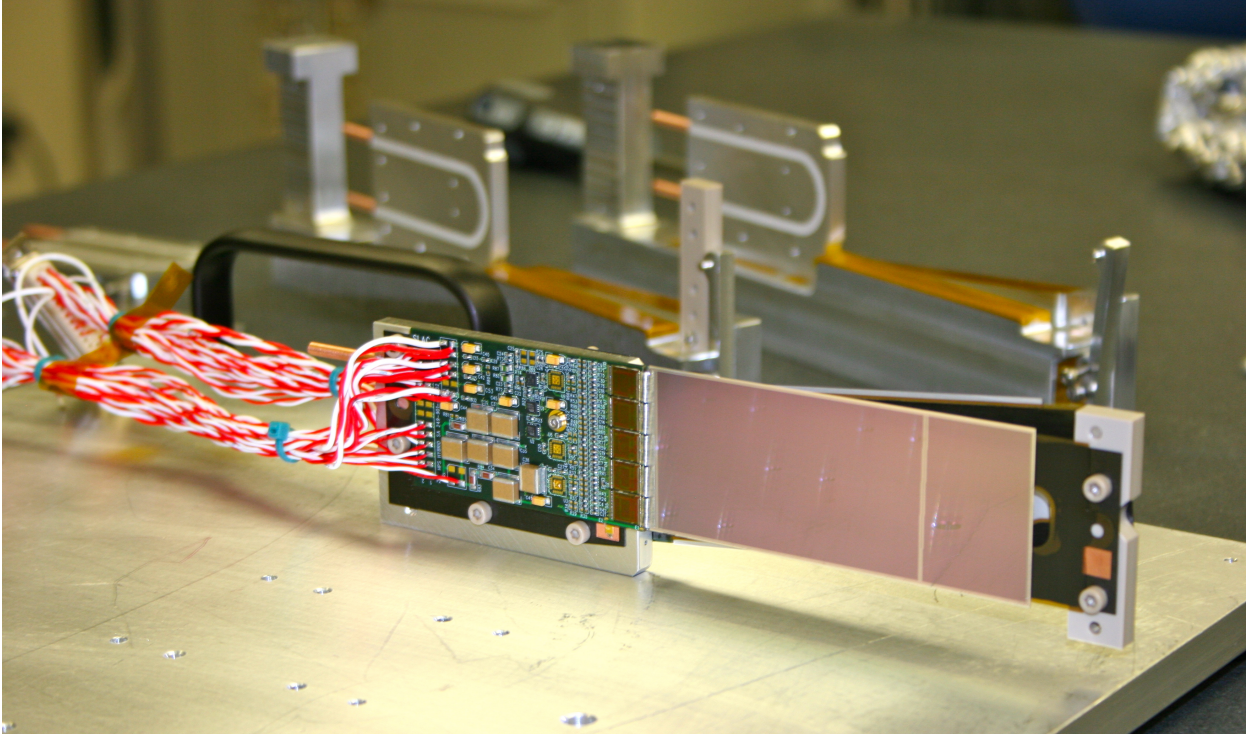


FIG. 14. A prototype module assembly (foreground) with the 50 mrad (left) and 100 mrad (right) module assembly fixtures in the background. A pair of cooling blocks and a spacer block can be seen on the fixtures.

Module yields were good for such a small production. Of 165 chips acquired, 150 were used to assemble 30 production hybrids, of which 29 passed QA testing. Of 29 modules built, 28 passed QA testing, leaving 8 spare modules after completion of the HPS Test SVT.

#### *4.3.4. Support, Cooling and Cabling*

Support for each half of the SVT is provided by an aluminum support plate. Due to the tightly constrained vertical clearance in the vacuum chamber, the support plate has a set of pockets machined to a precise depth so that the cooling blocks can be recessed into the plate while leaving the bulk of the plate thick enough to achieve the required stiffness. To isolate the cooling block thermally from the support plate and provide the relative module elevations dictated by the 15 mrad dead zone, a set of PEEK pedestals sit in the pockets beneath the cooling blocks.

The two halves of the tracker are connected to hinges mounted on a C-shaped support

just beyond layer 5 that defines the nominal spacing between the upper and lower halves of the tracker. An aluminum shaft attached to each support plate in front of layer 1 extends upstream and connects to a linear shift that transfers motion into the vacuum box through bellows to open and close the tracker around the dead zone. The C-support is mounted to an aluminum baseplate that defines the position of the SVT with respect to the vacuum chamber.

Each half of the SVT uses a pair of welded, stainless cooling manifolds to provide coolant to the modules. The manifolds are welded to flexible cooling lines that allow for the motion of the tracker. The pigtail cables and cooling manifolds are strain relieved with a pair of PEEK plates that hold both in place along the back ends of the modules. The pigtail cables attached to each module connect to a set of internal cables that are built into covered cable trays that run along the edges of the support plates to the feedthroughs on the vacuum flange. Figure 15 shows a number of these key details on the upper and lower support plates.

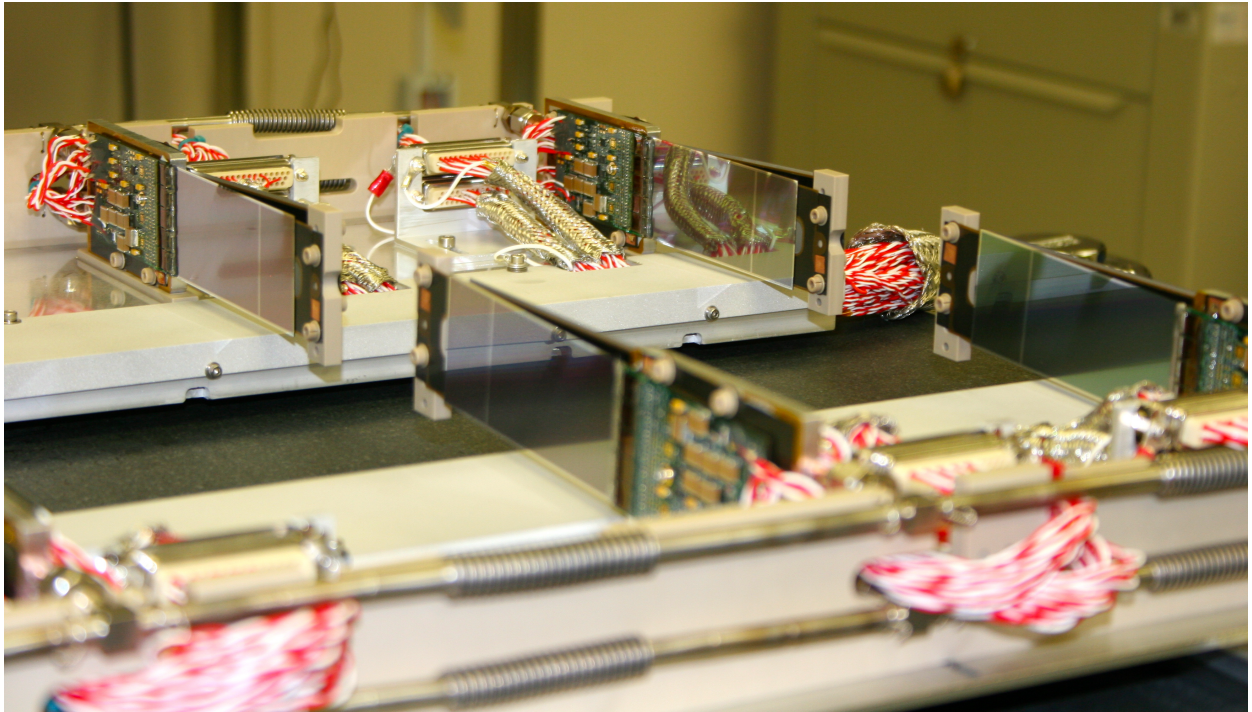


FIG. 15. A closeup of the SVT support plates showing the modules mounted to their pockets atop the PEEK pedestals, the pigtails and cooling manifolds routed along their strain reliefs and the pigtails connected to the shielded internal cables that pass into the cable trays.



#### 4.3.5. *Power and Motion Control*

Power is provided to each hybrid using CAEN power supplies provided by Fermilab. Three low voltages are supplied for the APV25 and one high voltage to reverse bias the sensor. The supplies that provide sensor bias are capable of 500V operation and can be used to test operation at high voltage in close proximity to an electron beam. The total power consumption of each hybrid during normal operation is about 2 W, which is removed with the cooling system. Care was exercised in selecting power and data cables, to ensure vacuum compatibility and sufficient radiation hardness. The teflon-coated twisted pair copper wires selected are rated for 400kRad, well above the expected exposure of 20kRad/week. A special purpose junction box interfaces the CAEN power supply output channels to the SVT hybrids. Control of the supplies is provided via an EPICS graphical user interface, which allows monitoring of the detector and interlock protection as well.

The linear shifts that define the opening of the SVT are controlled by a pair of stepper motors located in low field regions at the ends of the analyzing magnet. For photon running, these are locked in the open position, but for electron running they will be connected and controlled through EPICS so that the distance between the beam and the sensors can be adjusted to balance detector occupancies and acceptance.

#### 4.3.6. *Assembly, Testing, Shipping and Installation*

Hybrids and half-modules were assembled at SLAC. Mounting APV25 chips and all wire-bonding and QA testing were performed at UCSC. All 29 production modules were assembled between mid-February and the end of March, 2012. Hybrids underwent quick QA testing and each half-module was run at low temperature ( $\approx 5^\circ \text{C}$ ) and fully characterized for pedestals, gains, noise and time response after assembly. Full-module assembly and mechanical surveys were performed at SLAC in early April before final assembly, testing and shipping of the SVT to JLab on April 11.

At JLab, the entire detector was integrated with the full DAQ and the power supplies for the first time in the cleanroom, before moving the module-loaded support plates to Hall B for final mechanical assembly and installation inside of the vacuum chamber on April 19. Figure 16 shows the assembled tracker just prior to installation and Figure 17 shows the

tracker installed inside the vacuum chamber in Hall B. All of the detector appears to be functioning and commissioning continues at the time of this writing.

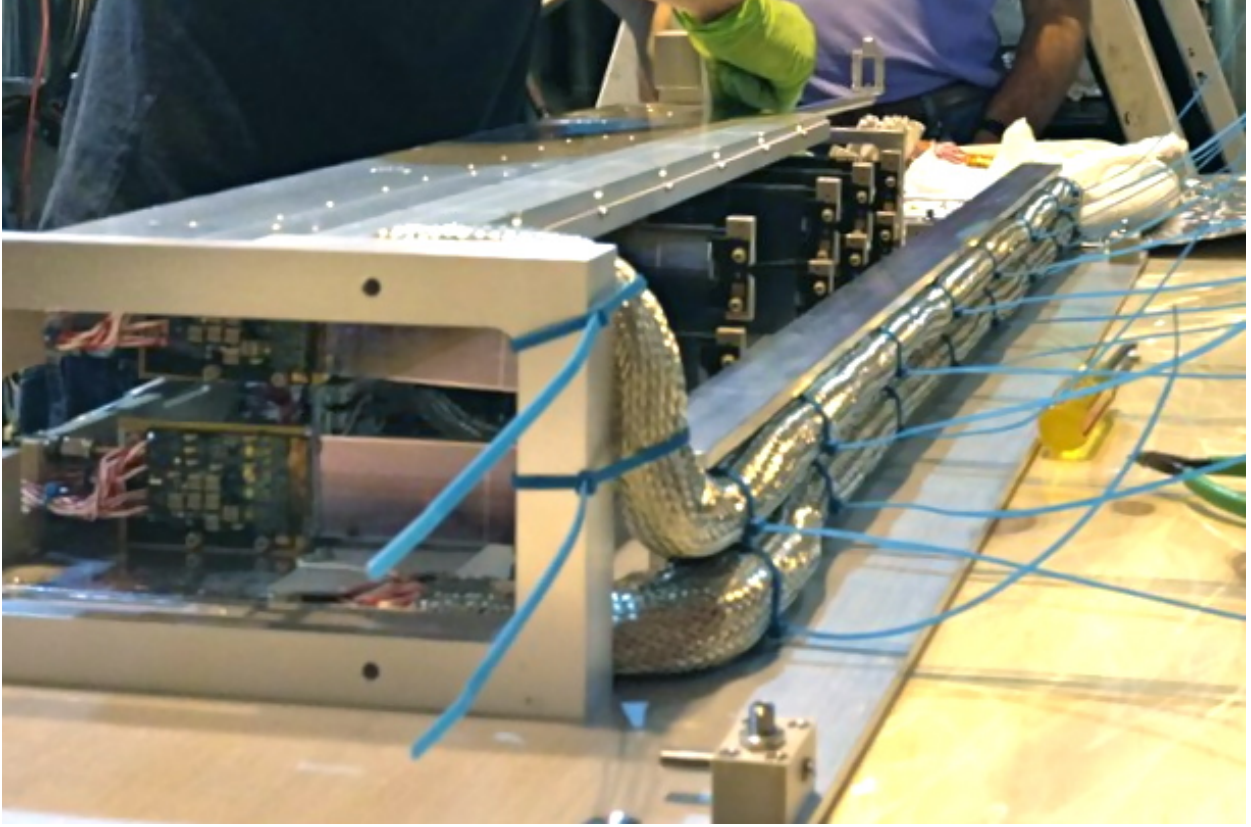


FIG. 16. The SVT fully assembled immediately prior to insertion in the vacuum chamber in Hall B. Note the shielded cable bundles passing upstream on the I-beam stiffener for the base plate.

#### 4.4. Electromagnetic Calorimeter

The HPS Test Run electromagnetic calorimeter (ECal) consists of 442 lead-tungstate ( $\text{PbWO}_4$ ) crystals with avalanche photodiode (APD) readout. Modules from the CLAS Inner Calorimeter (IC) have been reconfigured for the HPS ECal. They include crystals read out with Hamamatsu APDs S8664-55 and pre-amplifier boards (see Figure 18). The IC crystals are 160mm long and are tapered. The dimensions of the front (back) face of the crystal are  $13.3 \times 13.3 \text{ mm}^2$  ( $16 \times 16 \text{ mm}^2$ ).

New enclosures with temperature stabilization, support frames, connection boards and mother boards have been fabricated for the ECal. Crystals in the ECal are arranged in two

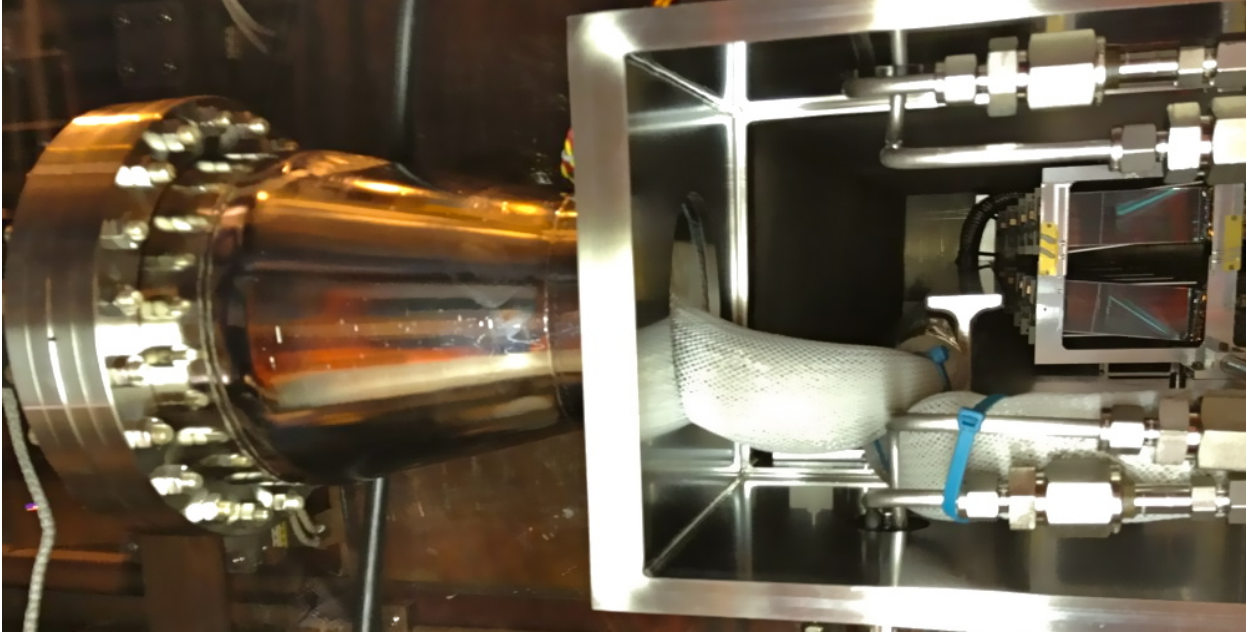


FIG. 17. The SVT installed inside the vacuum chamber. The upper cable bundle can be seen exiting the vacuum flange at left. Note the dielectric breaks on the cooling lines in the foreground.

modules. There are 5 layers in each module; four layers have 46 crystals and one has 37. The ECal is mounted downstream of the analyzing dipole magnet at the distance of  $\sim 137$  cm from the target. The two Ecal modules are positioned just above and below the beam plane such that the edge of the crystal closest to the beam is 25mm from it. As was described in Section 4.2.2 a vacuum chamber will be installed in between the two ECal modules for the electron test run.

In order to maintain stable performance of the  $\text{PbWO}_4$  calorimeter, the crystals and APDs are enclosed within a temperature stabilized environment, held constant at the level of 1 °F. The expected energy resolution of the system from operational experience with the IC is  $\sigma_E/E \sim 4.5\%/\sqrt{E(\text{GeV})}$ . As in the IC,  $\text{PbWO}_4$  modules are connected to a motherboard that provides power to and transmits signals from individual APDs and pre-amplifier boards. Crystals inside the box are supported by aluminum frames, Figure 19.

The ECal makes use of the existing low and high voltage systems from the IC, as well as signal cables and splitters. Connectors on the existing signal cables have been rearranged to accommodate the new layout of the channels.

In Figure 20 ECal is shown in its installed position for the parasitic run with photon beams. It centered relative to the beam that passes in between two parts of ECal through



FIG. 18. ECal crystal module consisting of a  $\text{PbWO}_4$  crystal, and APD and a pre-amplifier board.

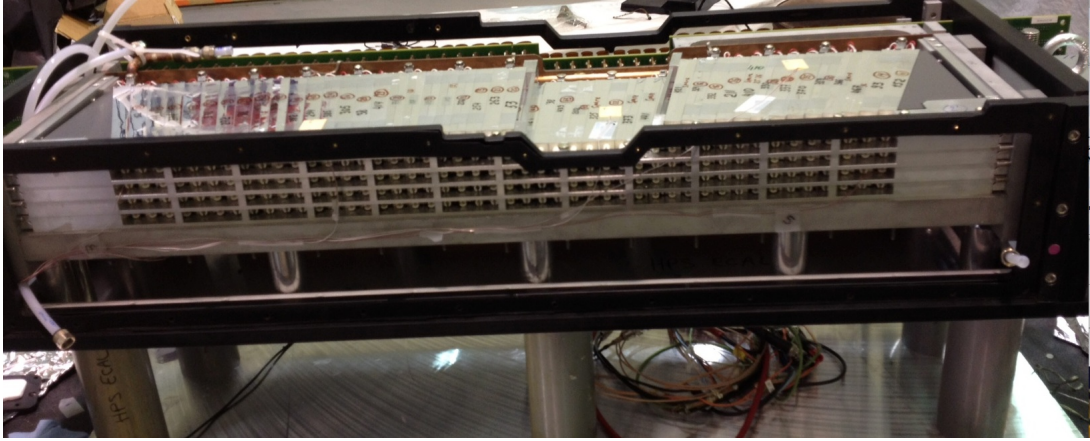


FIG. 19. Assembly of the ECal bottom module.

3 inch beam pipe. Cooling lines, as well as signal, HV and LV cables are visible.

#### 4.5. Electronics and DAQ

There are two front-end electronics systems, an Electromagnetic Calorimeter (ECal) system and a Silicon-Vertex Tracker (SVT) system. A level 1 hardware trigger selects events to be read out. Only the ECal provides inputs to the Level 1 trigger system. The triggered



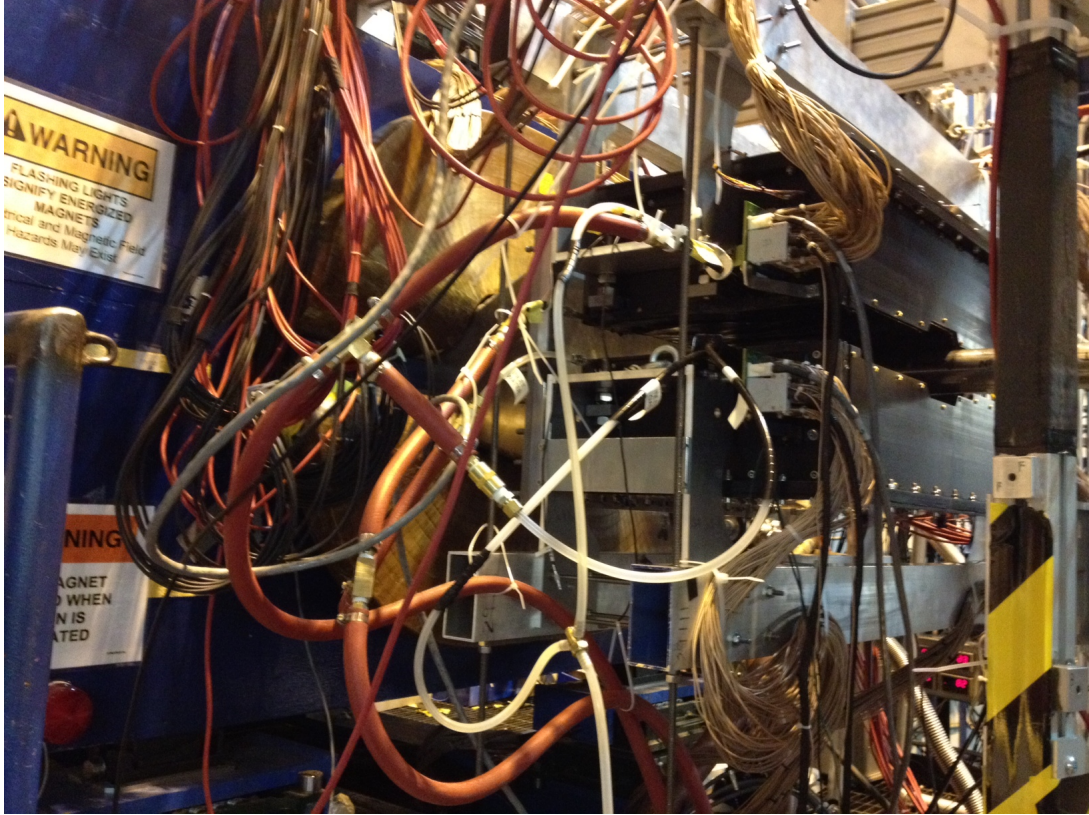


FIG. 20. ECal mounted downstream of the Hall-B pair spectrometer for the parasitic run with photon beams. Hoses for the cooling system, and the power and signal cables for beam-right side of both modules are visible.

events from the two sub-systems are acquired and processed in the data acquisition and processing system. The generic scheme for the HPS DAQ system hardware is shown in Figure 21.

Readout Controllers (ROCs) are installed in every VME, VME64X, VXS and ATCA crate. The ROCs are collecting data from the front-end boards, processing it and sending it to the Event Builder over the network. The Event Builder is a program running on a server assembling information from the calorimeter and the tracker. Currently mvme6100 controllers with a prpmc880 or pmc280 co-processor modules are employed. That configuration is fast enough to meet the HPS requirements.

A Foundry Router is currently used as the backbone of the DAQ system, providing 1Gbit and 10Gbit connections between components and to the JLAB Computer Center. The Event Builder, Event Recorder, and other critical DAQ components are running on

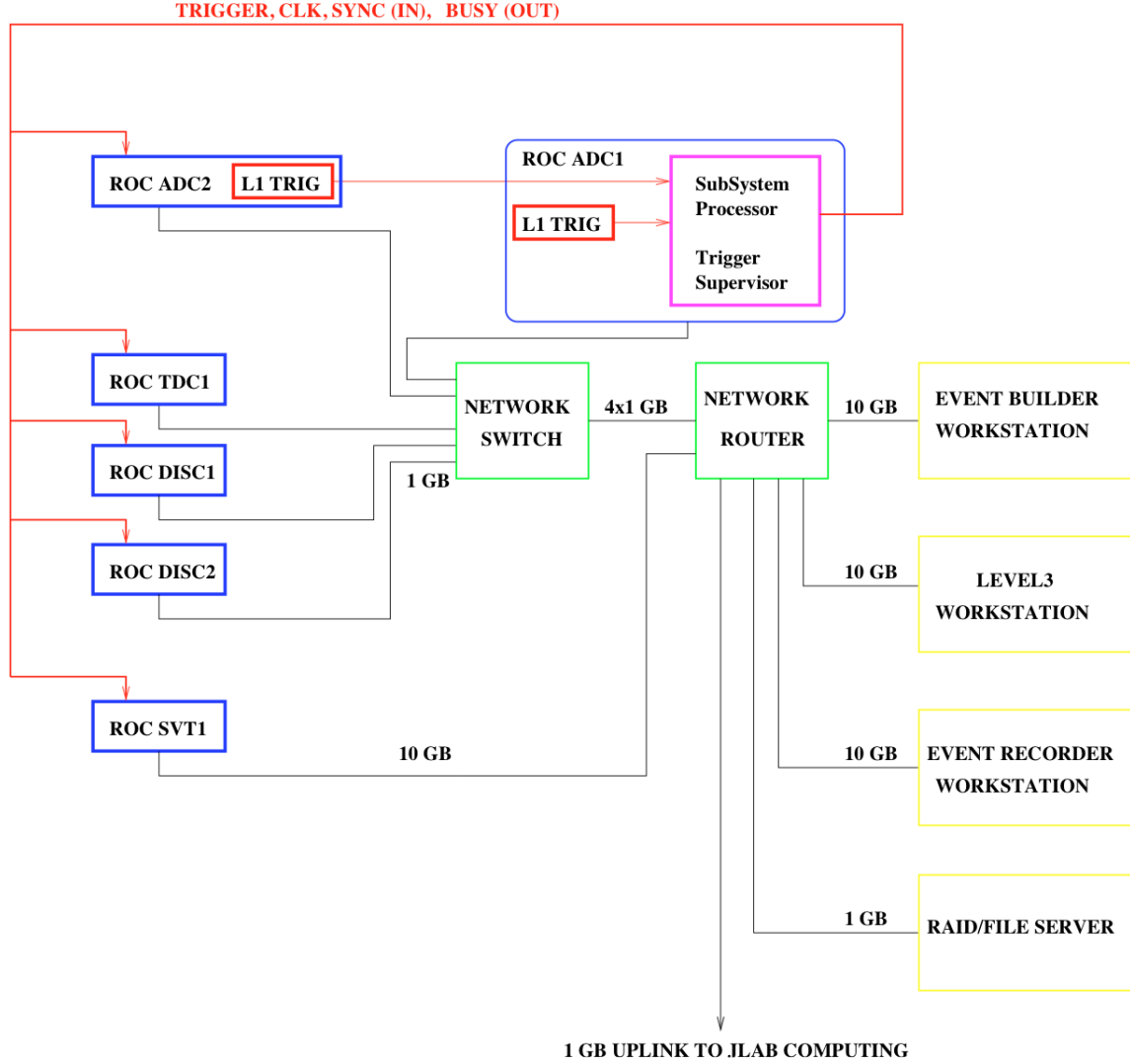


FIG. 21. Readout and processing system block diagram.

4-CPU Opteron-based servers, and that configuration is sufficient for HPS as well. ROCs are linked to the Foundry Router through smaller 1Gbit switches with 4Gbit uplinks. The HPS data storage system (RAID5) is sufficient for up to a 100 MByte/sec data rate.

#### 4.5.1. SVT DAQ

The SVT DAQ is a SLAC built data acquisition system utilizing the Advanced Telecommunication Computing Architecture (ATCA) for high speed data transfer. It is designed to readout data continuously at 40 MHz from the silicon detector modules, and transfer data to the JLab DAQ once a trigger signal is received. It can support a trigger rate of a few 10s

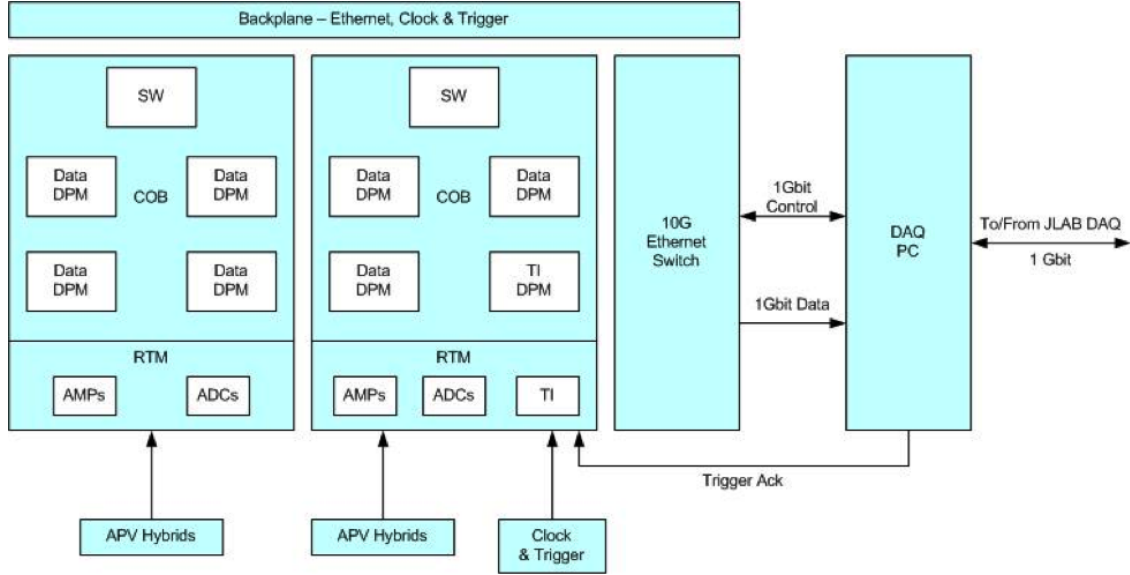


FIG. 22. Schematic of the SVT DAQ showing input from the hybrids mounted on the silicon detector to the RTM, its connection to the COB, and the Ethernet switch used to transfer data a 1 Gbit/sec to the DAQ PC and ultimately to the JLAB DAQ. Details are given below.

of kHz.

There are a total of 20 silicon strip sensors, each one connected to an onboard readout card called a hybrid which holds five 128-channel APV25 integrated circuits. The APV25s provide amplification, pipelining, and analog storage for trigger accepted events. There are 5 analog outputs for each 640-channel hybrid. Each hybrid will be connected via a multi-twisted-pair cable to a readout board.

The SVT readout system is shown in Figure 22. The outputs of 12 hybrids are digitized on an ATCA (Advanced Telecommunication Computing Architecture) RTM (Rear Transition Module) board. A pre-amplifier converts the APV25 differential current output to a different voltage output scaled to the sensitive range of a 14-bit ADC. The RTM is organized into 4 sections with each section supporting 3 hybrids (15 channels). The ADC is operated at the system clock of 41.667 Mhz. The RTM also includes a 4-channel Fiber Optic module and supporting logic which can be used to interface to the JLAB trigger supervisor card.

On the ATCA main board (also known as the Cluster On Board or COB), shown in Figure 23, there are 4 FPGAs each interfacing to a single section of the RTM. Each FPGA exists on a separate daughter card known as the Data Processing Module or DPM. The DPMs receive the digitized data from the RTM ADCs, apply thresholds for data reduction



FIG. 23. The Cluster on Board (COB) board, the main board of the SVT DAQ. The RTM is plugged into the COB in the back.

and organize the sample data into UDP datagrams. The DPMs also host an I2C controller used to configure and monitor the APV25 chips. One DPM in the system is configured to operate as a trigger interface module, receiving and distributing the system clock and trigger to the rest of the ATCA crate. The ATCA crate hosts 2 COB cards, one supporting 4 data processing DPMs and the other supporting 3 data processing DPMs and one trigger DPM. A total of 21 hybrids are supported, 1 more than the 20 required. The two ATCA COB cards and their DPMS are interconnected with a 10G switch card which also hosts two external 1Gbit Ethernet interfaces to a standard PC.

The external PC supports three network interfaces, 2 standard 1G-bit Ethernet and one custom low latency data reception card. The first Ethernet interface is used for slow control and monitoring of the 8 DPM modules. The second Ethernet interface serves as the interface to the JLAB data acquisition system. The third custom low latency network interface is used to receive data from the SVT ATCA crate and supports a low latency, reliable TTL trigger acknowledge interface to the trigger DPM. This PC hosts the SVT control and monitoring software as well as the JLAB ROC (Read Out Controller) application.

#### 4.5.2. *ECal Front End Readout*

Signals from each module are sent to a signal splitter. One of the outputs of the splitter is fed to a discriminator that also has an internal scaler, and then to a TDC channel. The





FIG. 24. FADC250 VXS module.

other output is sent to the Jefferson Lab FADC250 VXS module, Figure 24. Two FADC crates are required for the two modules. The trigger from the ECal is based on FADC information and includes a cluster finding algorithm using FPGA modules. It is described in Section 4.5.3. With the FADCs, the energy of clusters will be determined at the crate trigger level and will be used in making the trigger decision.

#### 4.5.3. *Trigger System*

A block diagram of the HPS tests run trigger processing is shown in Figure 25. A gigabit bandwidth is used to transport all the individual FADC250 channel sums (5-bits) and clock (3-bits) encoding bits to resolve a 4 ns period within a 32 ns frame. The clock encoding bits report the time when the input signal crosses the programmable threshold within the 32 ns frame. If the input signal does not cross threshold for a given 32 ns frame, then the channel data is reported as zero.

The reported 5-bit channel sum value is extracted from the 17-bit register that contains

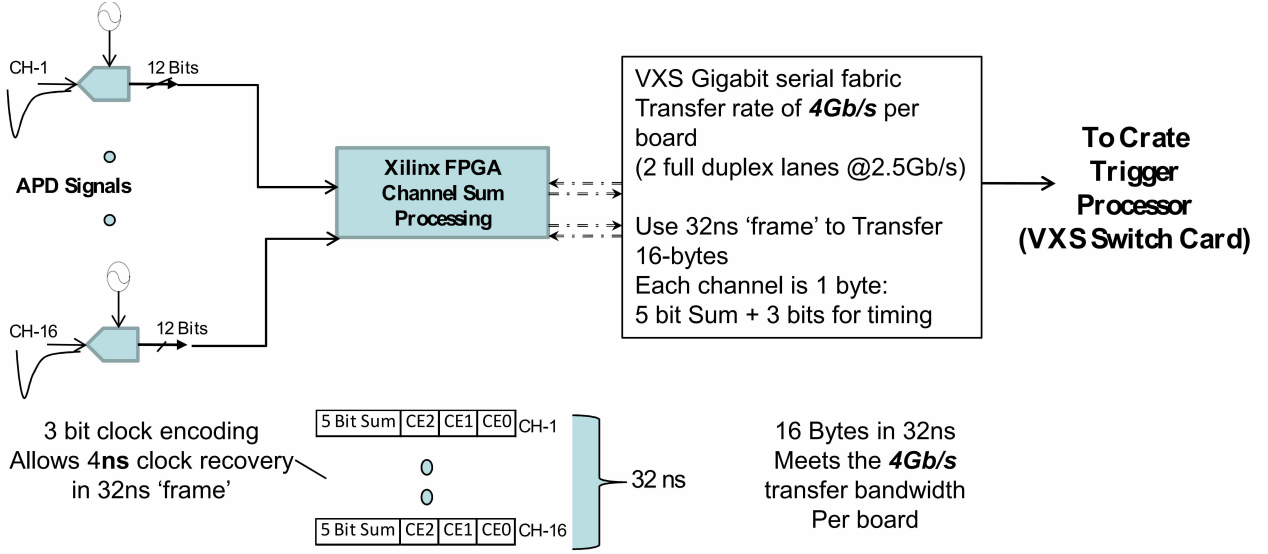


FIG. 25. Block diagram for the trigger system.

the integrated (sum) signal value of the input channel. The channel integration occurs only if the input signal crosses the programmable threshold level. The samples that are included in the channel integration are those that are above threshold. The number of samples for a given channel integration will not be larger than the frame report latency time (MAX=128ns or 32 samples). Samples of the input signal are shown in Figure ???. The point where the input signal crosses threshold determines which frame the integrated value is reported. The time where the input signal crosses threshold is captured within the frame and reported with the three clock encoding bits to a 4ns time stamp of the threshold crossing time.

In the example, the pulse for channel 2 crosses multiple frames. The point where the signal crosses threshold determines the frame where the integration value will be reported for the given channel. The number of points that are over threshold will be limited to 32. If multiple pulses within a 32 ns frame they will not be resolved will crate pile-up effect. The trigger application will only process a single falling edge or single rising edge per 32ns frame. Multiple pulse signals may be recoverable from the readout data offline.

Information from each FADC channel will be reported to the Crate Trigger Processor (CTP) through Gigabit serial data streams. The sixteen serial data streams will be processed on a frame by frame basis, and the cluster finding algorithm will produce a serial data stream that will be processed by the Sub-System Processor (SSP) to create a readout trigger signal that can be distributed to the front end FADC250 for Physics event readout. The system is

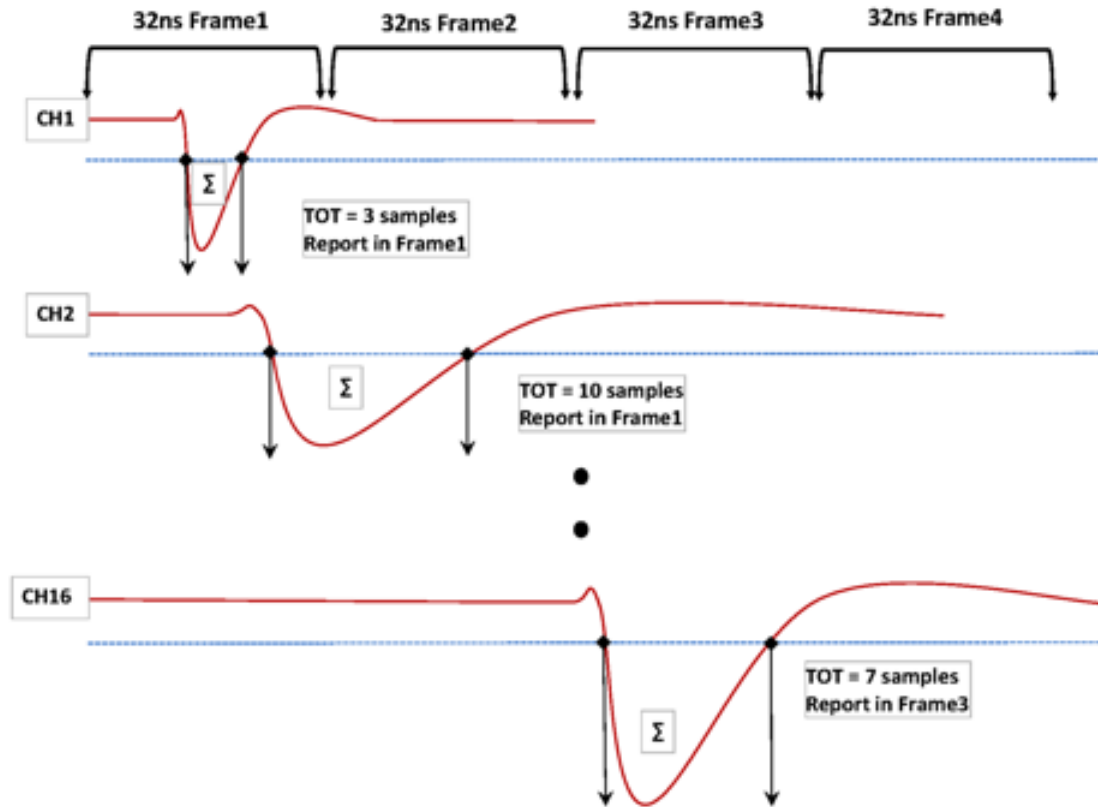


FIG. 26. Example of input signals.

designed for maximum trigger accept rate of 50 KHz.

## 5. SIMULATION OF TRIGGER RATES AND TRACKING PERFORMANCE FOR ELECTRON RUNNING

### 5.1. Event Generation and Detector Simulation

We use two generators to produce events: MADGRAPH for signal and trident events, and EGS5 for beam electrons that interact in the target. In MADGRAPH, we have produced large samples of signal events at various  $A'$  masses as well as large samples of Bethe-Heitler and radiative trident events. The passage of the electron beam through the target is simulated using EGS5; electrons that interact or scatter more than 5 mrad are saved for propagation to the detector. The beam is generated in 2 ns bunches where the number of electrons is chosen according to the desired beam current.

We use a GEANT-4 based simulation[84] to propagate events through the detector and model the energy deposition. We include the SVT sensors and Ecal  $PbWO_4$  crystals as well as a realistic accounting of the dead material for each sensor, the vacuum flange in front of the ECal, and the Ecal vacuum chamber. The energy deposits are converted to realistic digitized hits using algorithms to simulate the APV25 and FADC response for the SVT and ECal respectively. These digitized hits are handed to the reconstruction code to form clusters, tracks, etc. just as recorded data is.

### 5.2. Trigger Simulations

We have presented full simulations of the trigger rates expected for full HPS in our original proposal to PAC 37, and additional work in our HPS Test Run proposal for DOE. Both simulations demonstrated that trigger rates in realistic conditions are manageable. However, neither simulation included possible pileup effects deriving from the finite pulse width of the Ecal signals, or the fact that the beam arrives at 500 MHz. Both of those deficiencies have now been corrected with more detailed simulations, which are described here. The bottom line is that the results of the earlier simulations are confirmed, and that the trigger rates are manageable.

First we discuss the trigger algorithm and the expected Level-1 trigger rates based on Geant4 simulations of the detector.

The test run will be looking at  $(e^+e^-)$  final states. The level-1 trigger algorithm will

search for two clusters of energy in opposite segments of the ECal (with respect to the beam direction), since the heavy photon is produced predominantly in the direction of the beam and thus pairs of oppositely charged leptons will be well separated in opposite segments of the ECal.

The Bethe-Heitler process will generate most of the electron pairs; however, due to high rates and overlapping phase space, accidental coincidences of processes such as elastic scattering, photon bremsstrahlung and Møller scattering will contribute in the trigger (accidental final states  $(\gamma e^-)$  and  $(e^- e^-)$ ). The coincidence time used by the clustering algorithm for grouping hits in individual counters into clusters will play a crucial role in reducing the trigger rate.

#### 5.2.1. *Geant4 simulations of the ECal*

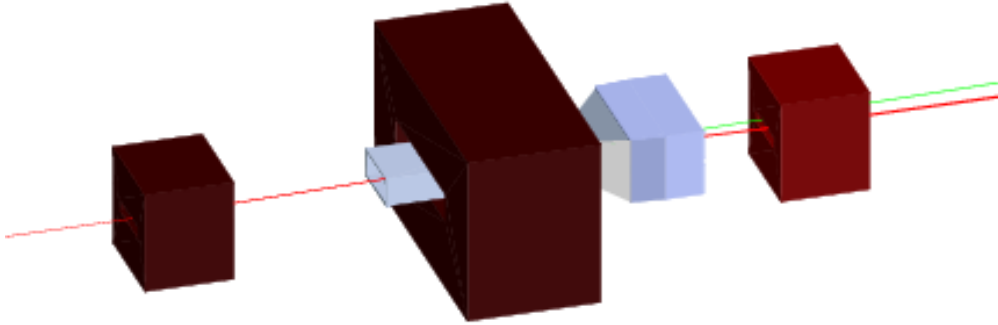


FIG. 27. Rendering of the Geant4 simulation showing the three magnets in red and in gray the vacuum box for the silicon tracker system and the enclosure for the electromagnetic calorimeter. The red line represents the electron beam, the green line represents secondary photons produced in the target.

As described in the original PAC 37 proposal a full Geant4 model of the experiment has been implemented, for both full HPS and now for the HPS Test Run. The model includes all the elements for the electron run: the two steering magnets (“Frascati magnets”) and main analyzing magnet, the target, the silicon trackers, the main components of the vacuum system, and the electromagnetic calorimeter. The detector details have been given in Section

4 above. For studying the beam properties all the magnetic fields were modeled using a measured field map. For large statistics running the fields were uniform fields, tuned to reproduce the beam path of the mapped field version. Figure 27 shows a rendering of the test setup.

The Geant4 model of the calorimeter includes the positions of the lead-tungstate crystals and a CAD model of the ECal vacuum chamber. A rendering of the simulated calorimeter is shown in Figures 28 and 29.

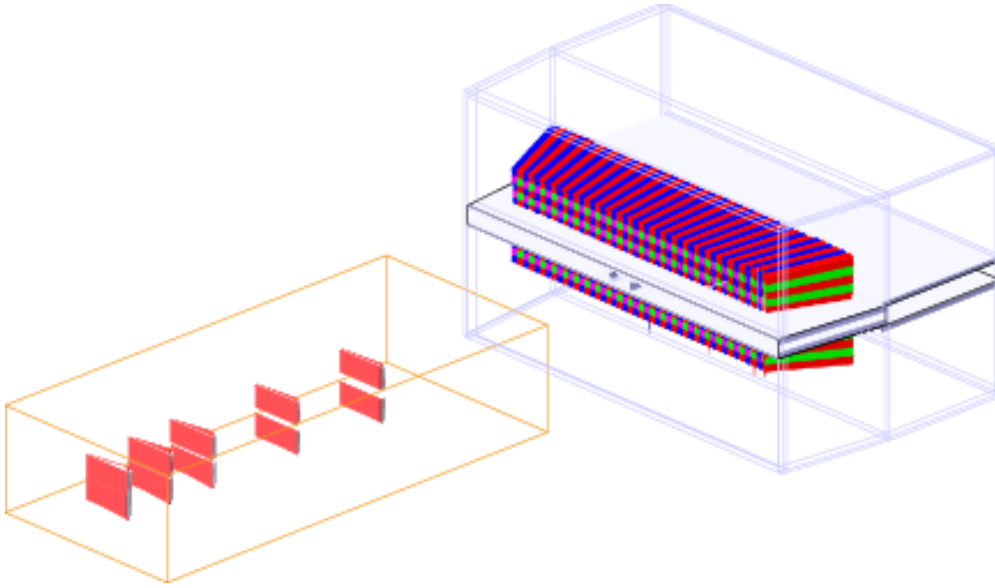


FIG. 28. Rendering of the detector simulation used for trigger studies. The orange box represents the container for the silicon trackers (outlined only), the red rectangles represent the silicon tracking layers, and the larger blue-gray outlined rectangles represent the box for the calorimeter. The final object shows the calorimeter, with the crystals colored in alternate colors for clear visibility.

To study the performance of the calorimeter and the trigger logic a large number of background events were simulated. Background events were generated by sending 2,500 2.2 GeV electrons through the 0.125%  $X_0$  tungsten target (equivalent to 2 ns — one beam bunch — of a 200 nA beam) and letting the Geant4 physics models generate the expected backgrounds (scattered electrons, produced photons and other particles). The physics models used in this simulation include all electromagnetic processes implemented in Geant4. The same background simulation was also done with EGS5. In addition, Bethe-Heitler and radiative tridents were simulated using MadGraph/MadEvent.

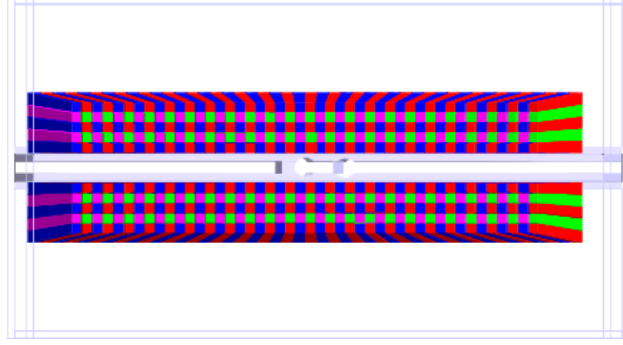


FIG. 29. A rendering of the electromagnetic calorimeter setup looking down the beam line. The front exit window and side plates are rendered transparent to permit a view of the crystals and the vacuum plates.

Beam background samples from Geant4 or EGS5 were merged with trident samples from MadGraph/MadEvent and saved as “full background” samples of particles emerging from the target. All parts of the background simulation were run with no preselection of events, or only a minimal set of cuts — only particles that were well within the beam gap, and therefore well out of the detector acceptance, were dropped from the background samples.

For the trigger studies, input signal events were used that were generated with MadGraph/MadEvent. These events simulated  $A'$  masses of 50, 75, 100, 150, 200, and 250  $\text{MeV}/c^2$ . The output files of these simulations could be merged with the “full background” samples to create realistic data samples for different scenarios.

These samples were then processed in SLIC, a Geant4-based detector simulation package, to simulate showers and energy deposition in the silicon tracker and ECal. The readout and triggering were modeled in LCSim, a Java-based simulation and reconstruction framework.

### 5.2.2. *Hit Rates in the Calorimeter*

Two aspects of the calorimeter performance were studied with the simulation. The hit rates on the individual crystals were looked at to make sure these rates will be within a reasonable range for the expected running conditions, and the expected trigger rates for simulated  $A'$  particles and for background events were studied to make sure the trigger has adequate sensitivity to signal events and adequate background rejection to stay under the maximum allowable DAQ trigger rate. This section details the hit rates, the next section

the trigger rates.

Hit rate simulations were done using an ECal model with the full 46 crystals in every row. As one would expect, the highest rates occur on the crystals that are closest to the exiting electron beam. A map of the percentage of events with at least one hit — the hit occupancy for each crystal — using a time integration window of 8 ns (representing the coincidence window of the trigger) and a hit threshold of 100 MeV, is shown in Figure 30. The maximum hit occupancy occurs for crystal number -4 and -3 in the first row, with close to 25% occupancy.

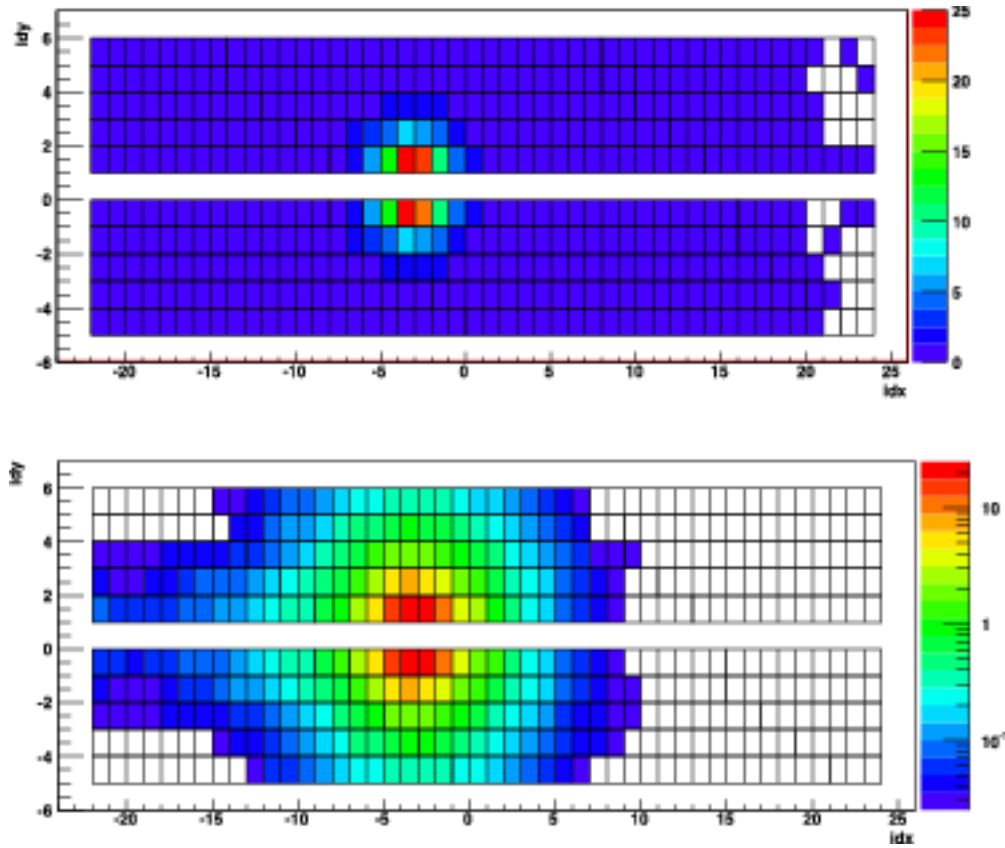


FIG. 30. Hit occupancies in the electromagnetic calorimeter for a time window of 8 ns and a threshold of 100 MeV. The figure on the top has a linear z-scale, the figure on the bottom is identical except for the logarithmic z-scale. Note that the x and y axis are the index of the crystal, not the position. The increased threshold reduces the occupancies on the hottest crystals (row 1,  $x = -3$  and  $-4$ ) to around 25%.

We control high hit rates in three ways: removing the crystals with particularly high



background rates, applying energy thresholds to crystals, and using trigger selection cuts to eliminate trigger candidates not consistent with A' events.

A more detailed picture of the running conditions for the crystals of the electromagnetic calorimeter can be obtained by looking at the hit rates. Figure 31 shows the hit rates in the first row of the ECal, at varying thresholds. The highest hit rates are for crystals numbered between -5 to -2; this motivates our decision to remove crystals -2 through -10 from the ECal entirely. In addition, it is clear that applying energy thresholds significantly reduces rates.

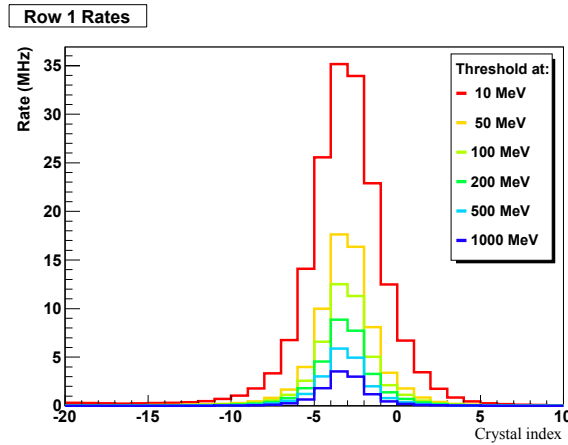


FIG. 31. Hit rates for crystals in the first row for different thresholds.

### 5.2.3. Level 1 trigger simulations

To accurately estimate trigger rates, a Level 1 trigger algorithm was developed and optimized using simulated background data and simulated A events with masses ranging from  $50 \text{ MeV}/c^2$  to  $250 \text{ MeV}/c^2$ . The events were processed with the full Geant4 based simulation described in the previous section. The full analog and digital readout chain was simulated, including time evolution of analog pulses, digitization and integration of analog signals, the FPGA-based clustering algorithm, and trigger cuts.

The ECal preamplifiers were simulated as CR-RC shapers with a peaking time of 18 ns, based on fits to oscilloscope measurements. Pileup from multiple hits was simulated; Figure 32 shows a series of hits in a single ECal channel and the resulting pulse train. The FADC algorithm for hit digitization, edge detection and integration was used to convert this pulse

train to digitized hits. The FADC threshold (used for hit time discrimination) was set to 50 MeV in simulation to minimize dead time and time walk effects.

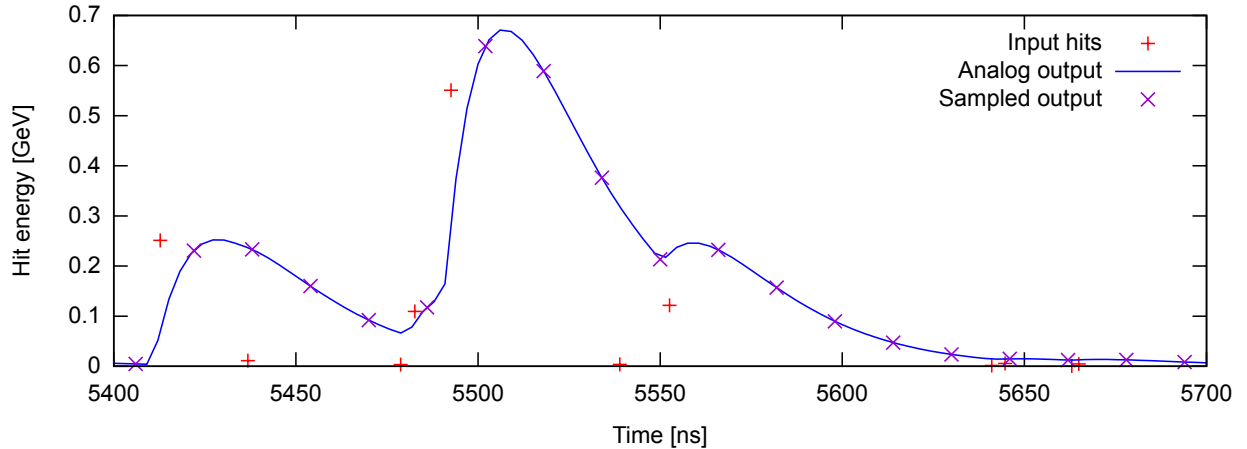


FIG. 32. Pulse shaping and pileup simulation for an ECal channel.

The Crate Trigger Processor (CTP), which produces clusters from FADC data, can be run in a mode that will generate triggers with a 4 ns jitter, and a coincidence time between channels of two 4 ns clock cycles, or 8 ns. This mode encodes the energy sum with 5 bit accuracy.

The first step in the Level 1 trigger algorithm is the identification of clusters in the electromagnetic calorimeter. Table III shows each of the subsequent cuts and their effect on the number of accepted A' trigger candidates together with the effect on the background trigger candidates. The simulated A' mass used was 75 MeV. Numbers are given as a percentage of the total number of simulated events. A more detailed description of each trigger selection cuts follows.

At the lowest level, a trigger required two good clusters in opposite quadrants of the calorimeter. Many events would have multiple clusters in at least one of the two quadrants, in which case all combinations of clusters were tried for trigger candidates. This double counting is not shown in the first row of the table, and eliminated in the last step. This accounts for the increase from the first to the second row in the table.

Since the clusterer operates with a coincidence window of 8 ns, twice the clusterer time resolution, many clusters appear in two consecutive 4-ns trigger candidates. This double-counting is eliminated in the last step of the trigger simulation, where a “dead time” is

applied to the trigger. A small value (40 ns) was used in this step; while smaller than any realistic value, this is conservative in terms of not underestimating background trigger rate, and has no effect on A' acceptance.

Trigger cut	75 MeV/ $c^2$ A' acceptance	Background rate
Pairs of clusters in opposite quadrants	59.5%	1.8 MHz
Cluster energy between 100 MeV and 1.85 GeV	45.1%	725 kHz
Energy sum less than $E_{beam}$	45.1%	431 kHz
Energy difference less than 1.5 GeV	45.1%	386 kHz
Energy-distance cut	36.1%	80 kHz
Clusters coplanar to within $35^\circ$	35.3%	46 kHz
Not counting double triggers	34.4%	43.8 kHz
Applying trigger dead time	18.8%	34.8 kHz

TABLE III. Trigger selection cuts and their effect on the A' acceptance and background rate, as a percentage of the total number of simulated events. An A' mass of 75 MeV/ $c^2$  was used for this illustration.

As the table shows, a large fraction of the background events, corresponding to a background trigger rate of 1.8 MHz, have at least two clusters in opposite quadrants of the detector. A further refinement on the trigger conditions requires that each of the clusters has an energy of at least 100 MeV, but no more than 1.85 GeV. This eliminates low energy background hits and hits from electrons with energies close to the beam energy, while having little effect on the A' acceptance. The rate of accepted background events now drops to 725 kHz. The algorithm now identifies the more energetic and less energetic hit which make up this trigger pair and requires that their sum is less than the beam energy multiplied by the calorimeter sampling fraction. This cut removes some of the pileup and accidental events. A further cut requires that the two hits do not differ in energy by more than 1.5 GeV. These cuts reduce the background rate to 386 kHz.

Next a two dimensional cut is made in distance (of the hit from the beam) plane versus the energy (of the hit). These distributions are shown in Figure 33. The previously mentioned lower energy cut for the clusters is shown as the vertical black line. The histograms show

that an additional cut for the least energetic cluster along the red sloped line ( $E + d \ 3.2$  (MeV/mm)  $< 800$  MeV), effectively eliminates background events, reducing the background rate to 80 kHz.

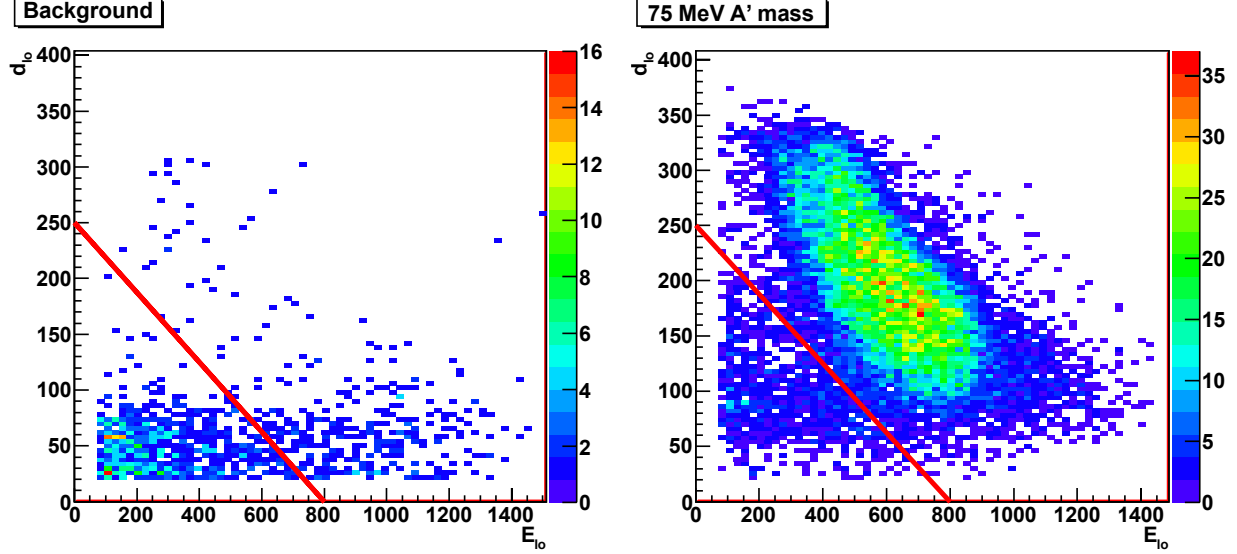


FIG. 33. The distance of the cluster center to the beam is plotted versus the energy of the cluster for the less energetic cluster of the trigger pair. The left side plot shows background events, the right side plot shows simulated  $A'$  events with a mass of  $75 \text{ MeV}/c^2$ . As can be seen from the plots, an effective cut to eliminate background events without significantly affecting the  $A'$  acceptance is indicated by the red lines.

The requirement that the two clusters are coplanar with the beam within 35 degrees further eliminates background events, leaving 46 kHz. Finally, removing the double-counting (multiple cluster pairs in a single event, and multiple triggers in consecutive events) reduces the background rate to 34.8 kHz.

These cuts leave us with a trigger rate which is acceptable to the trigger electronics, which have a maximum rate of 50 kHz. It still leaves some headroom for less than perfect beam conditions, a slight increase in the beam current, or inaccuracies in the Geant4 physics model. If an additional reduction of the trigger rate is desired, it is possible to remove a few crystals from being considered for the center of a cluster.

The same trigger algorithm was run on simulated data for a number of different  $A'$  masses. The resulting acceptance estimates are shown in Table IV and Figure 34. The proposed

trigger algorithm retains high efficiency for signal events and suppresses the background triggers by a factor of 100.

Trigger cuts were tested by running on samples consisting purely of A' events and purely of background events, but computing actual A' acceptance was done by overlaying A' events on background. This was necessary to allow for the effects of dead time, time walk and accidental coincidences. As shown in Table V, the number of A' triggers lost (an A' event that was triggered on in the absence of background was not triggered on when background was added) was generally comparable to the number of A' triggers gained, and both effects were small, assuring us that our trigger's A' acceptance is largely unaffected by the background environment.

A' Mass (MeV/ $c^2$ )	50	75	100	150	200	250
Acceptance	11.5%	19.3%	16.2%	8.1%	3.9%	2.5%

TABLE IV. Trigger acceptance estimates for different A' masses for runs with a beam energy of 2.2 GeV.

A' mass [MeV]	Acceptance, no background	Lost	Gained	Acceptance with background
50	10.2%	1.9%	3.2%	11.5%
75	18.8%	2.8%	3.3%	19.3%
100	17.8%	4.2%	2.6%	16.2%
150	6.8%	1.2%	2.4%	8.1%
200	2.8%	0.5%	1.6%	3.9%
250	2.0%	0.6%	1.1%	2.5%

TABLE V. Trigger acceptance estimates for different A' masses, before and after adding the effect of background events.

### 5.3. Simulated Tracker Occupancies and Acceptance

Full Monte Carlo tracker performance simulations were presented in our original PAC 37 proposal for HPS, and updated in our proposal to DOE for the HPS Test Run. The

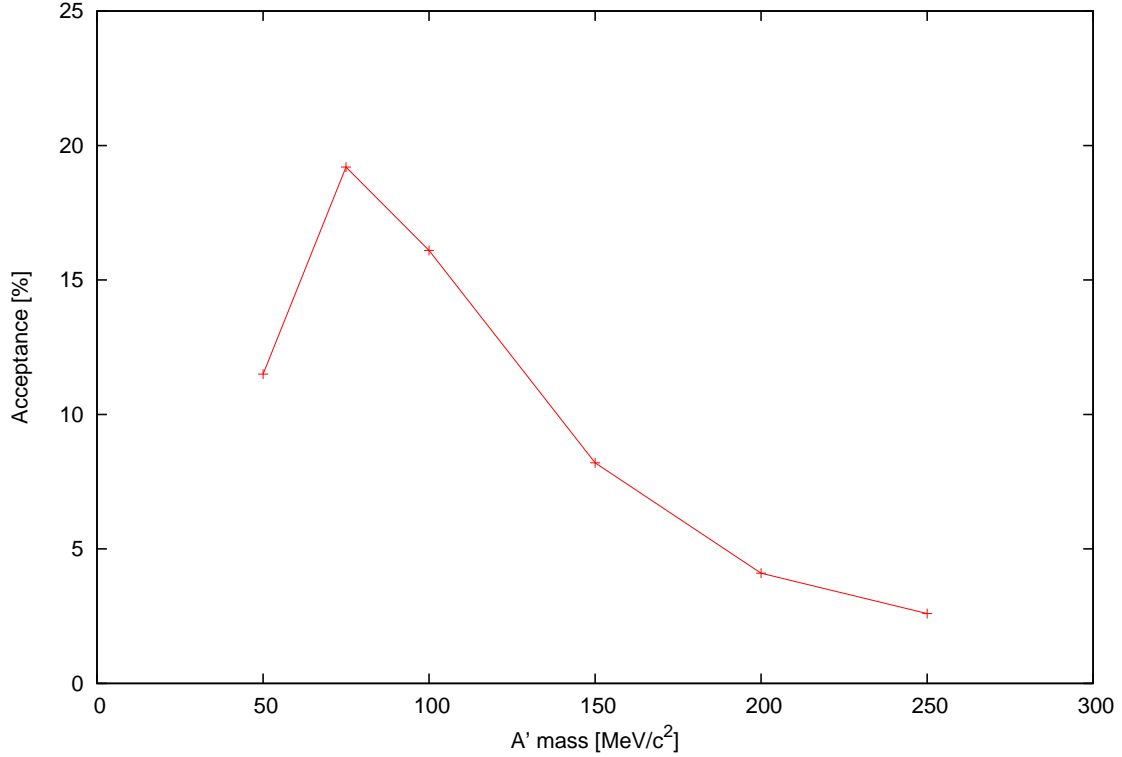


FIG. 34. Trigger acceptance estimates for different  $A'$  masses for runs with a beam energy of 2.2 GeV.

latter are included here for completeness, and to demonstrate the level of understanding we had achieved prior to data taking. Our first experience with real tracking in the Test Run experiment is discussed below in the update on the parasitic run. It will be augmented at the time of the PAC 39 meeting, as we have more data and some time to analyze it under our belt.

Figure 35 shows the distribution of charged particle hits in Si tracker layer 1 which is located 10 cm from the target as generated by EGS5 for electron running. The beam energy is 2.2 GeV, and the target thickness is  $0.125\% X_0$ . Multiple Coulomb scattered beam electrons are confined within 0.5 cm of the beam axis ( $x=y=0$ ), while the low energy Moller electrons are distributed in a parabolic shape. There are very few positrons. From

these distributions, the detector occupancy in the horizontal Si strip sensor in a 7.5 ns time window is calculated for a 200 nA beam current and five different target thicknesses,  $0.25\% X_0$ ,  $0.125\% X_0$ ,  $0.10\% X_0$ ,  $0.075\% X_0$ , and  $0.05\% X_0$ , and is shown in Figure 36. We define a "dead zone" using a criterion that the maximum occupancy in Layer 1 is 1%. For a  $0.125\% X_0$  target and 200 nA beam, the occupancy is 1% at a distance of 1.5mm from the beam in Layer 1, which corresponds to a dead zone of  $\pm 15$  mrad. As long as the product of target thickness (T) and beam current (I) is constant, the same A production rate is maintained. Since the multiple scattering and hence the effective beam size is reduced in a thinner target, it is advantageous to use a thinner target and a higher current. Using the constraint that the occupancy is 1% at 15 mrad, we find the beam current I which gives this occupancy for each of several potential target thicknesses T. The quantity  $(Im(A'[MeV])\gamma T)/2$ , which is approximately proportional to the sensitivity  $S/\gamma B$ , is given in Table VI, showing how the sensitivity improves as the target thickness decreases.

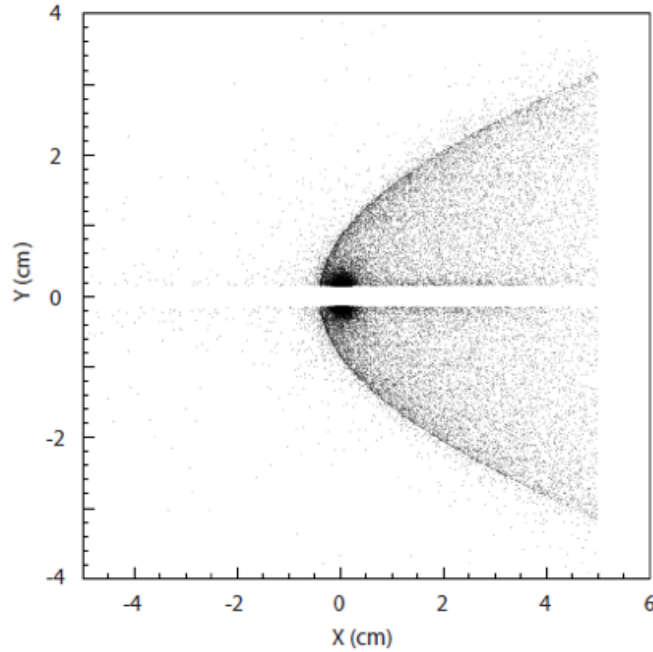


FIG. 35. Charged particle distribution in layer 1.

Once the dead zone is determined, the tracker acceptance can be calculated by requiring that both  $e^+$  and  $e^-$  from  $A'$  decay are detected in all ten silicon layers. The tracker parameters given in Table 2.3.4.1 are used. Figure 37 shows the tracker acceptance as a

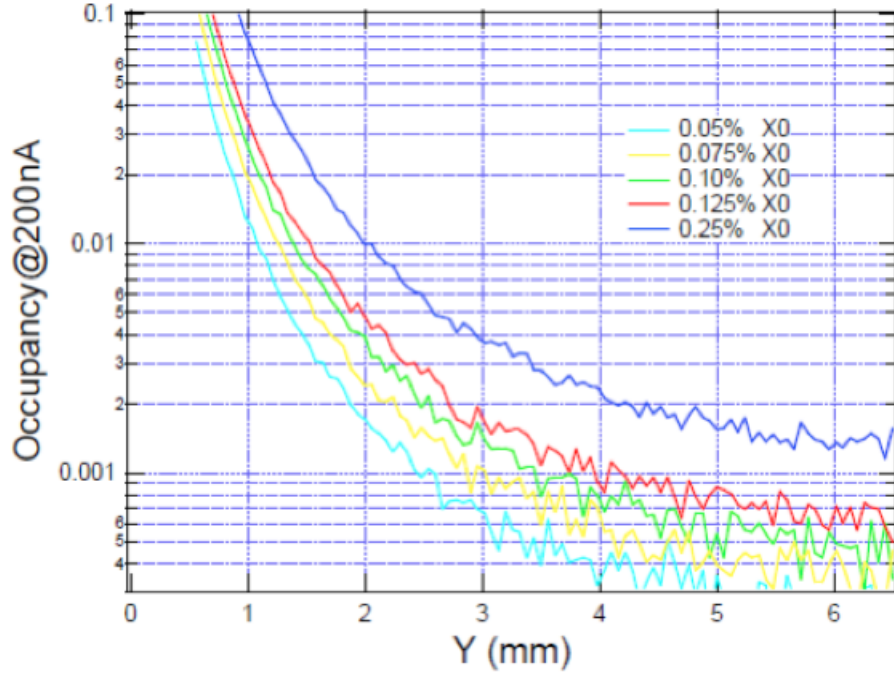


FIG. 36. Silicon sensor layer 1 occupancy at 200 nA vs distance from the beam in mm.

TABLE VI. Beam current yielding 1% occupancy in Silicon sensor layer 1 for various target thicknesses at 2.2 GeV, and the relative experimental sensitivities which result.

Target Thickness (% $X_0$ )	Beam Current (nA)	$\alpha S/\sqrt{(B)}$
0.25	85	9.2
0.125	190	13.7
0.10	250	15.8
0.075	340	18.4
0.05	530	23.0

function of  $A'$  mass at beam energy of 2.2 GeV when the  $A'$  decays at the target. The tracker has useful acceptance from 20 MeV to 250 MeV; lower (higher) beam energies can probe  $A'$ 's of lower (higher) mass. At the lower mass side, the dead zone limits the acceptance, while the transverse tracker size limits the acceptance at the higher mass side.



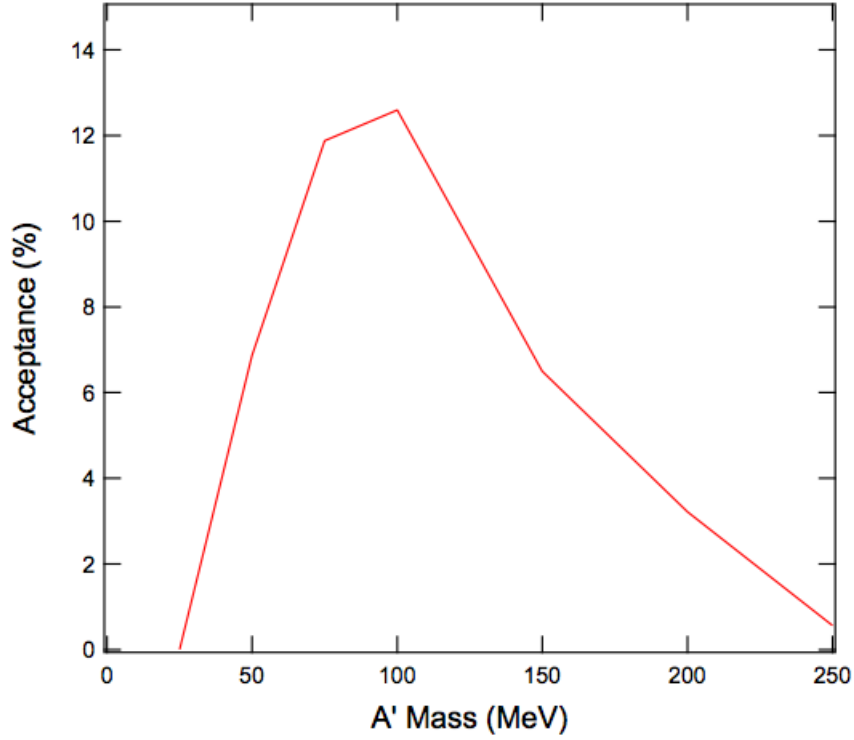


FIG. 37. Tracker acceptance as a function of  $A'$  mass.

#### 5.4. Simulated Tracking Performance

As mentioned above, we use a GEANT4 Si tracker simulation based on SLAC's org.lcsim infrastructure for full simulation of the passage of charged and neutral particles through the target and tracker. This simulation is used to get realistic estimates of tracking pattern recognition efficiencies and purities in the presence of all the expected electromagnetic backgrounds, and to evaluate momentum, invariant mass, and vertex resolution. In order to study the tracking performance of the detector (described below), we use samples of  $e^+e^-$  events at a variety of energies and decay lengths. On top of each event, we overlay backgrounds produced by the passage of  $2.2\text{GeV}/c^2$  beam electrons equivalent to  $200\text{nA}$  in  $7.5\text{ns}$  on a  $0.125\%$  W target and a beamspot of Gaussian sigma of  $20\mu\text{m}$  in the vertical direction and  $200\mu\text{m}$  in the horizontal.

#### 5.4.1. Tracking Efficiency, Pattern Recognition and Fake Rates

Due to the cuts imposed to guarantee good track quality, the efficiency for finding tracks in the geometric acceptance is not 100%. The average track reconstruction efficiency is 98% and the bulk of the inefficiency comes from the cut on the total  $\chi^2$  of the track fit. Of the reconstructed tracks, a small percentage include a hit that is not from the correct electron. These "bad" hits may be from one of the high energy beam electrons scattered from the target into the detector or from a lower energy secondary. The left plot of Figure 38 shows the number of bad hits/track for both the electron and positron from the  $A'$  decay. The number of tracks with 0 bad hits is  $> 98\%$  and the positrons are slightly cleaner since occupancy of the positron side of the detector is smaller. The right plot of Figure 38 shows the layer number of the bad hit. Hits in the first two layers are the most often mistaken, and they tend to be both incorrect. We will show how these bad hits affect the track parameters in the next section.

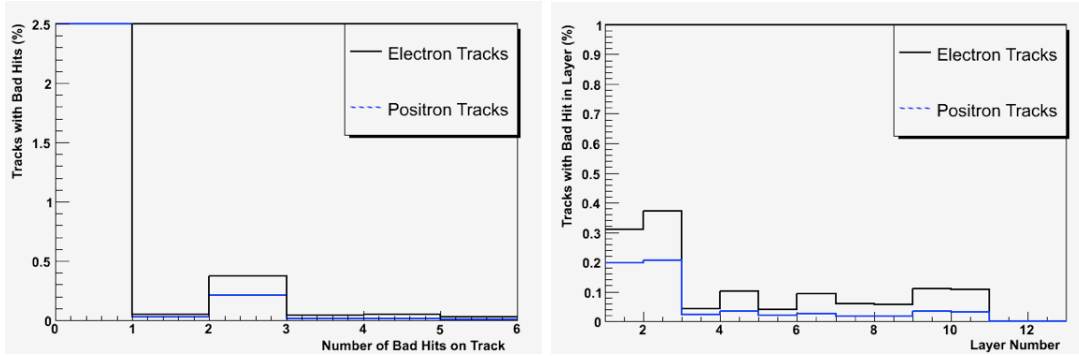


FIG. 38. The number of bad hits (left) and the layer number of the bad hit (right) for electron (black) and positron (blue) tracks prior to vertex selection.

#### 5.4.2. Track Momentum and Spatial Resolution

The momentum resolution is shown in Figure 39 as a function of momentum for tracks with 0 bad hits and for tracks with one or more. The momentum resolution for well-reconstructed tracks is  $\sigma(p)/p = 4\%$  while for hits with bad hits increases to 10%. One quantity we use to determine track quality is the distance of closest approach (DOCA) to the beam axis. We use this instead of the DOCA to the target beam spot since we are

interested in long-lived decays and tracks from those will not point back to the target. We separate the distance into the bend plane (XOCA) and non-bend plane (YOCA) distances. Below, in Figure 40, is the resolution of these quantities as function of momentum for tracks with 0 bad hits. The resolution is, on average, about  $100 \mu\text{m}$  ( $400 \mu\text{m}$ ) in the non-bend (bend) direction but increases significantly at low momentum. The position resolution for tracks with one or more bad hits is somewhat worse, depending on which layer the bad hit is in. In particular, when the bad hit is in the first non-bend layer (layer 1), the YOCA is very poorly determined as shown in Figure 40. Tracks with bad hits in layers 1 or 2 are a major contribution to the tail of the vertex position distribution. For long lived  $A'$  decays, the position of the decay vertex is an important discriminating variable. The dominant background to  $A'$  production is radiative trident events which originate in the target. Distinguishing  $A'$  decays from the background therefore depends on the vertex resolution and in particular on the tails of the vertex distribution. In order to study the tails, we use large samples of  $A'$  events decaying promptly overlaid on top of the simulated beam background events.

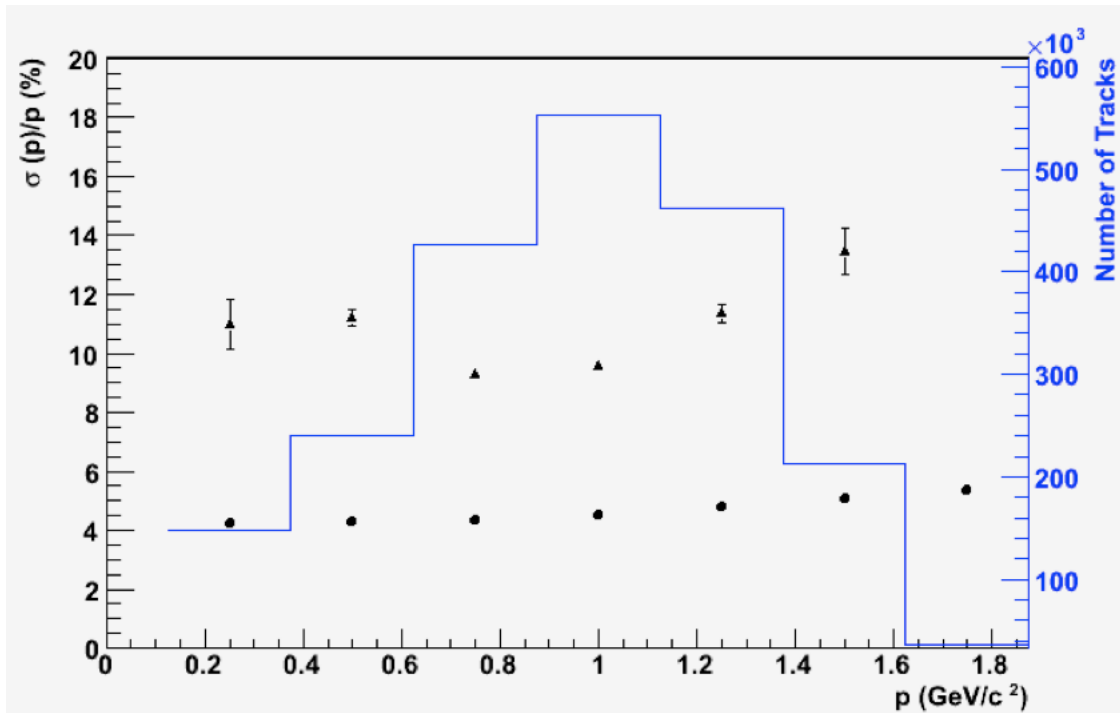


FIG. 39. Fractional momentum resolution versus momentum for 0 bad hit tracks (circles) and tracks with 1 or more bad hits (triangles).

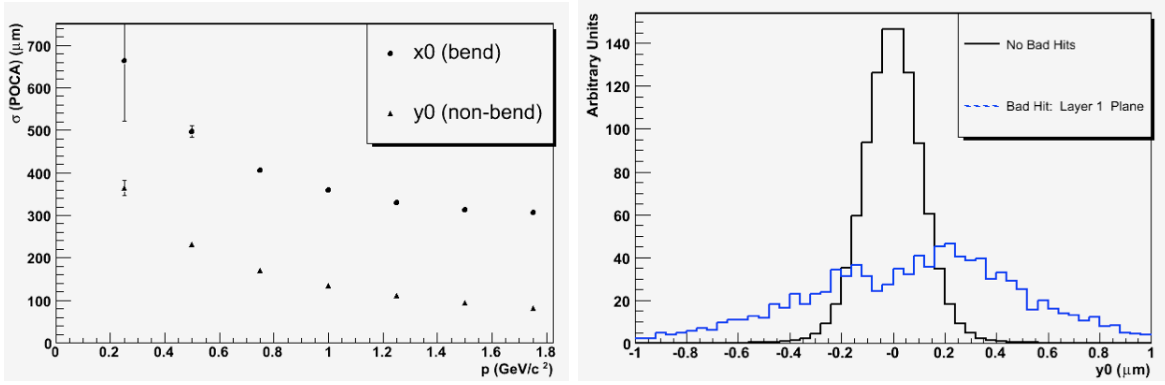


FIG. 40. LEFT: The resolution of the position of closest approach to the beam axis versus track momentum. RIGHT: The YOCA resolution for tracks with 0 bad hits (black) and with a bad hit in layer 1 (blue).

Each pair of oppositely charged tracks is fit to a common vertex using a Kalman filtering method first suggested by Billoir [85, 86] and used in many experiments. The method uses the measured helix parameters and their correlations to determine the most likely decay position of the  $A'$  and also returns fitted momenta for each particle. We actually fit each pair twice with different hypotheses of their origin. We constrain either the vertex to be consistent with an  $A'$ :

- which originates in the  $200\mu\text{m} \times 20\mu\text{m}$  beamspot at the target, and moves off in the direction given by the measured  $A'$  momentum. This fit will be used for the vertexing search.
- which originates and decays at the target within the  $200\mu\text{m} \times 20\mu\text{m}$  beamspot. This fit will be used for the bump-hunt only search.

For each electron/positron pair reconstructed in the tracker, we compute the invariant mass based on the fitted momenta of the tracks. The mass resolution depends on the invariant mass of the pair and is shown in Figure 41. The right-hand plot in Figure 41 shows the improvement in the resolution for the second fit, where the decay is assumed to occur in the target.

Even for prompt decays, the  $z$  vertex position ( $V_z$ ) distribution of all reconstructed  $e^+e^-$  pairs (solid black histogram, Figure 42) shows a long tail, still significant beyond 5cm. This

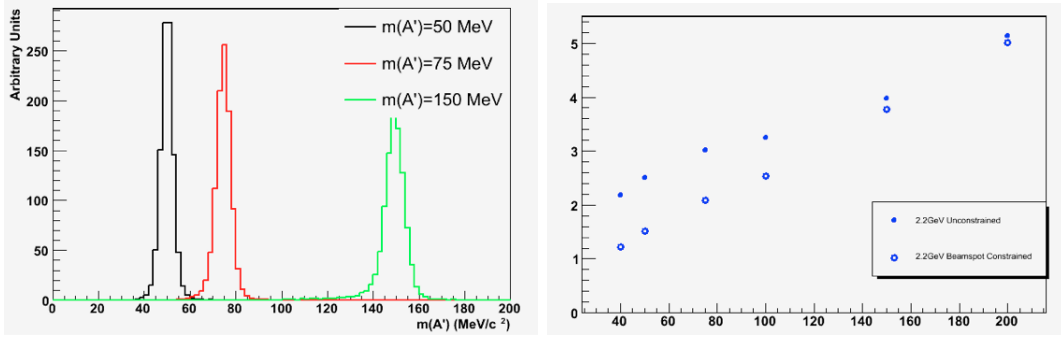


FIG. 41. LEFT: The mass distributions for different generated  $A'$  masses. RIGHT: The Gaussian width of the mass distributions ( $\text{MeV}/c^2$ ) vs generated  $A'$  mass ( $\text{MeV}/c^2$ ). The open circles are the resolutions when the decay is constrained to the target beamspot and the closed circles are without this constraint.

tail is primarily comprised of events where one or both of the tracks use one or more bad hits. Fortunately with appropriate cuts we can minimize the tails. Namely, for purposes of this proposal, we make the following cuts:

- the  $\chi^2$  of each track is less than 20
- the total momentum of the  $A'$  candidate is less than the beam energy
- a very loose cut on the reconstructed vertex position  $|Vx| < 400\mu\text{m}$  and  $|Vy| < 400\mu\text{m}$
- the clusters in layer 1 of each track must be isolated from the next closest cluster by at least  $500\mu\text{m}$
- a  $\chi^2$  cut on the vertex fit of less than 15

The vertex resolution depends on the invariant mass of the particles being vertexed. Lower masses have worse Gaussian resolutions as shown in Figure 42. This is expected since the error on the opening angle ( $\theta$ ), due to multiple scattering, scales like:  $\sigma(\theta)/\sigma \sim (1/E)/(m/E) \sim 1/m$ .

Figure 43 shows the vertex resolution for samples of 40 MeV and 80 MeV  $A'$  events. The cuts above remove almost all of the tail past  $\sim 1.5$  cm (points with errors in Figure 3.3.2.5) while retaining 50% of the  $e+e-$  pairs from the  $A'$  candidate. The events on the tail are enhanced with vertices where there are one or more bad hits on the track (represented by the

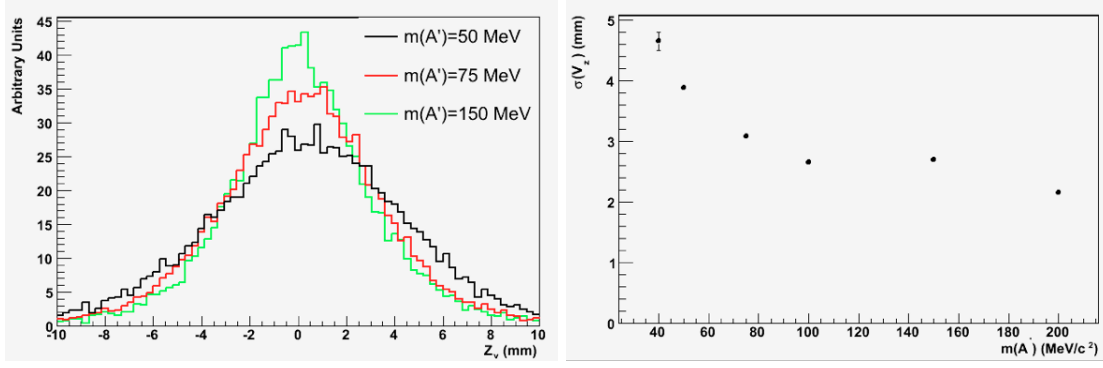


FIG. 42. LEFT: The distribution of reconstructed vertex positions for different masses of  $A'$ . RIGHT: The (Gaussian) resolution dependence versus  $A'$  mass for signal-only events.

blue histogram in Figure 43), although there is still a contribution from well-reconstructed tracks. The rejection of tracks with bad hits depends strongly on the precision of the virtual  $A'$  trajectory, which in turn depends on the size of the beamspot. Having a beamspot significantly smaller than the intrinsic tracker resolution, 100  $\mu\text{m}$  in the non-bend and 300  $\mu\text{m}$  in the bend directions, is important. In practice, there is much more we can do to clean up the vertex and mass resolution both at the track level (e.g. remove hits that are clearly from scattered beam electrons) and at the vertex level. These will be pursued in the near future.

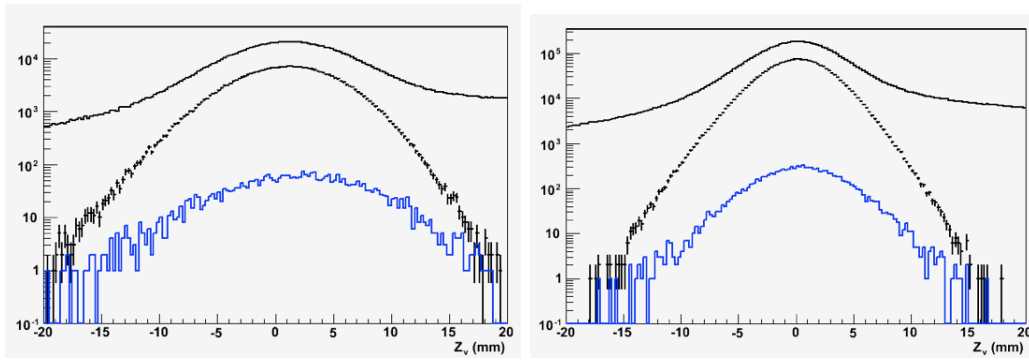


FIG. 43. Distribution of the reconstructed vertex position along the beam axis for 2.2 GeV for 40 MeV (left) and 80 MeV (right)  $A'$  events before (solid black) and after (points with errors) selection. The blue histogram shows the distribution for pairs that have at least one bad hit after selection.

## 6. TEST RUN STATUS

The HPS parasitic tests, staged over the Hall-B HDice run (g14) will accomplish the following: (1) integrate SLAC and JLAB readout systems into a single DAQ; (2) fully test the Level 1 trigger system based on FADCs; (3) test experimental monitoring and controls; (4) gain experience with running the test apparatus; (5) record and analyze photon interactions in the pair-spectrometer foil target.

The HPS test run apparatus was installed in Hall-B on April 19th during the experiment down time. Because access time to the hall was very limited, it took two weeks to debug and commission the hardware interlocks, electronics, the trigger system and DAQ. On May 4, the first production data from the HPS Test Run apparatus was recorded. HPS DAQ was triggered by the cluster finding trigger algorithm based on FADC250s from the ECal. Tracks have been reconstructed in the SVT in an off-line analysis. In this section, early results from the test run that started on April 19th are presented.

### 6.1. Parasitic Run Conditions

As noted in Section 4 the HPS test apparatus was designed and built to run in two modes, with an electron beam using the HPS target and with a photon beam using the Hall-B pair spectrometer (PS) pair converter as a target, which is located  $\sim 70$  cm from the first layer of Si-tracker. In Figure 44, the beam line configuration at the Hall-B pair spectrometer for the HPS test run is shown. the test run apparatus will be commissioned and calibrated using secondaries that are produced in the pair convertor of the PS. Both the Si-tracker and the ECal are retracted off the beam plane to allow clean passage of the photon beam through the system, and also not to obscure converted ( $e^+e^-$ ) pairs from being detected in the PS hodoscopes.

The large portion of the remainder of the run of the g14 experiment will use coherent bremsstrahlung photons with the coherent edge in the region of 1.8 to 2.0 GeV. Photon beams will be generated in the interaction of the 5.5 GeV electrons with the diamond radiator located  $\sim 20$  meters upstream of the PS pair converter. After collimation ( $D = 2$  mm), the photon beam passes through the pair converter, through the HPS system, and on to the g14 target. The thickness of the pair converter nominally is  $1.8 \times 10^{-3}$  r.l.. For tests

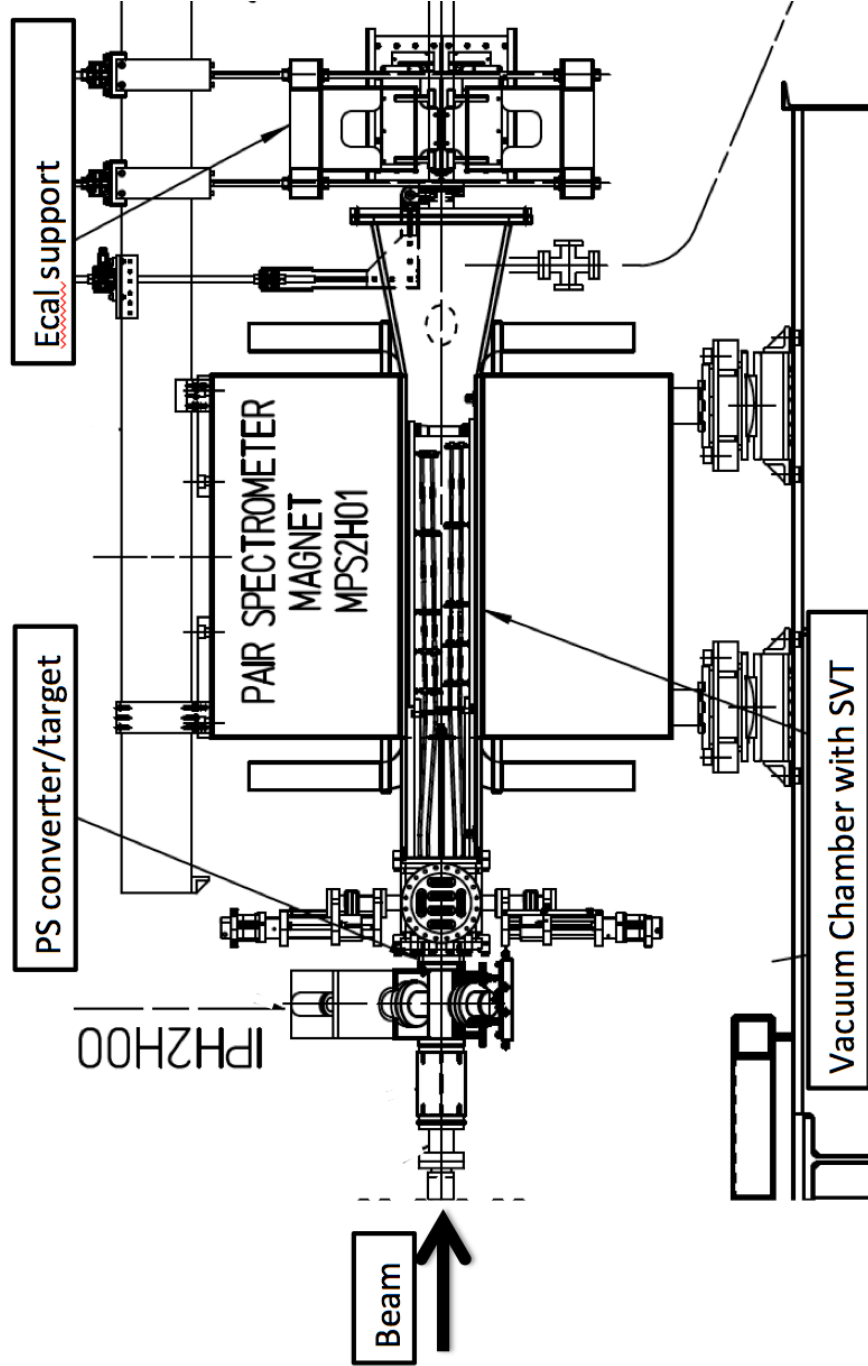


FIG. 44. Beam line configuration around the Hall-B pair spectrometer for the HPS parasitic test run.

we can also run with foils of  $4.5 \times 10^{-3}$  r.l. and  $1.6 \times 10^{-2}$  r.l. The nominal field setting for the pair spectrometer dipole for this run is  $\sim 0.75$  T. For HPS tests a few other values were used, ranging from 0.3 T to 0.75 T.



## 6.2. Experimental controls

The slow controls for the HPS beam tests were based on the Experimental Physics and Industrial Control System (EPICS) framework. This choice was primarily driven by the necessity to be compatible with the existing Hall B and CEBAF control systems. The controls for the HPS beam tests included multiple components such as control of the SVT and ECal power supplies and temperature monitoring. The existing Hall B experiment control screens were used to monitor the beam-line components of Hall B.

The ECal was connected to the same high voltage power supply modules from CAEN that were used for the CLAS Inner Calorimeter (IC). Therefore, we used the CLAS EPICS interface and the screens for the Inner Calorimeter high voltage controls.

The HPS Silicon Vertex Tracker uses custom designed power supply boards A509 and A509H which were built by CAEN for experiments at Fermilab. These boards were shipped to Jefferson Lab and EPICS support was developed for these boards to work on the VxWorks operating system. The communication to the the CAEN SY527 chassis that housed the boards went through a v288 CAENnet VME interface card. The alarms for the voltage channels were interfaced with EPICS using TTL-level outputs from the power supply boards connected to a digital input/output board. Controls screens were generated to simplify the operation of the SVT detector.

Both ECal and SVT readout electronics needed temperature stabilization, so both had cooling systems which required using two separate chillers. The temperature monitoring of the ECal used thermocouples read out using D5000 Series input modules from Omega. EPICS support for these modules was developed using the serial RS-232 interface. The temperature monitoring of the SVT was done using internal temperature sensors read out by the SVT data acquisition system and fed into the EPICS system. Since the silicon detectors were operating in vacuum it was critical to maintain the coolant flow through the system when the detectors were powered. The flow of the coolant is shut off in the event that vacuum deteriorates, as a precaution to prevent potential fluid leakage into the vacuum chamber. If the temperature or the pressure in the vacuum chamber readings exceeded their respective threshold values, the power to the SVT and the flow in the SVT cooling system was shut off using a hardware interlock system. The mass flow of the coolant, the vacuum pressure, and the status of the interlock system was readout and monitored using EPICS.

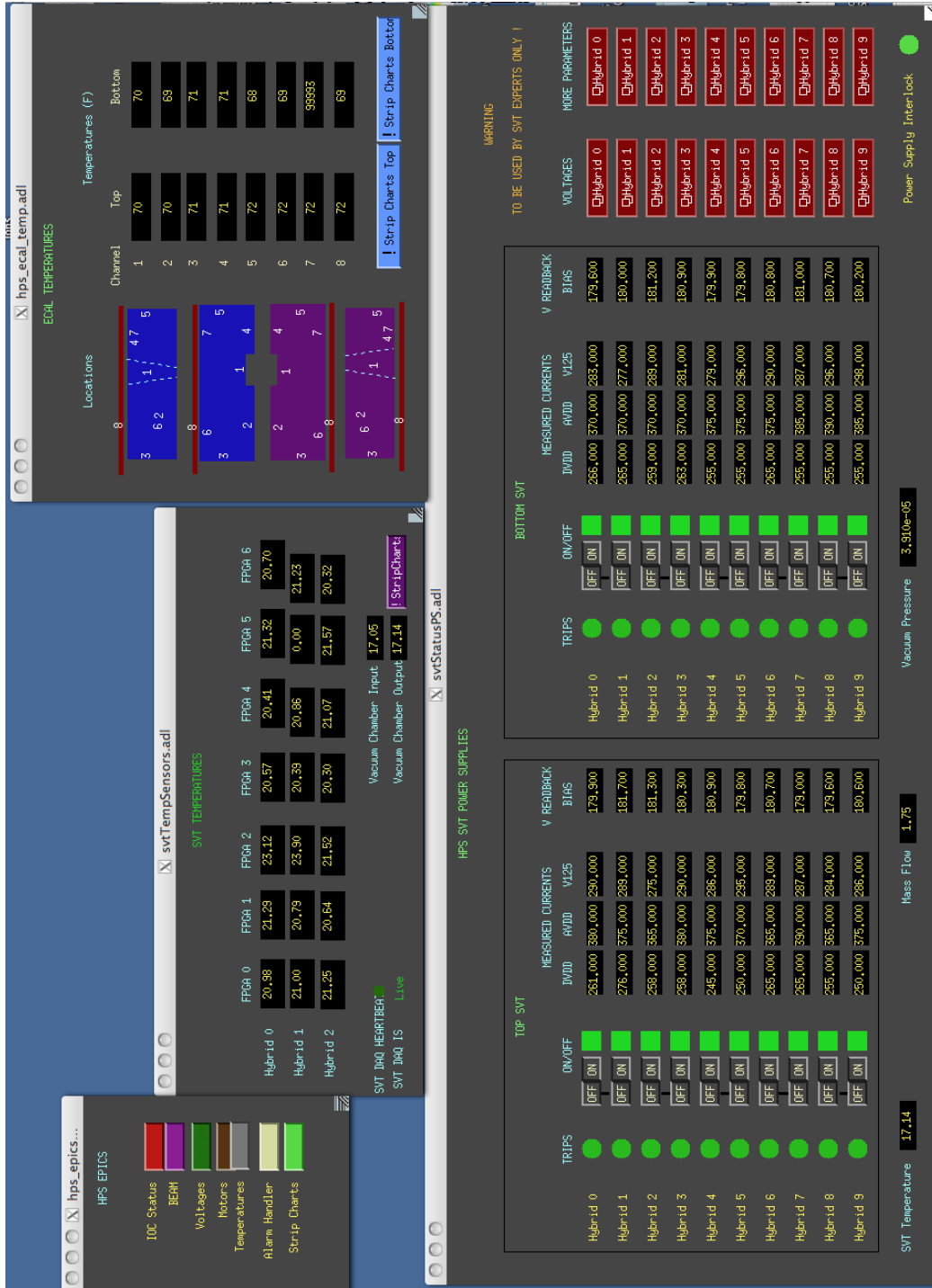


FIG. 45. EPICS GUI for operating the SVT power supplies.

In Figure 45 the EPICS GUIs for controlling the HPS SVT power supplies and monitoring the temperatures in the SVT and the ECal are shown.

### 6.3. Performance of the Test run Apparatus

#### 6.3.1. SVT Calibrations

In order to prepare the SVT for real physics data-taking, calibration of the readout system is required. This involves extraction of the mean baseline (pedestal), baseline noise and gain for each of the 12,780 SVT channels. All measurements are made with the APV25s configured to the nominal operating points [87] and all sensors biased to 180 V. The APV25s are being operated in multi-peak mode with six samples being readout per trigger. The six samples can then be used to extract the  $t_0$  and amplitude of the signal being read out.

A histogram of the pedestals for a single readout channel along with an intensity plot of the pedestals across a sensor are shown in Figure 46. The noise was then computed by

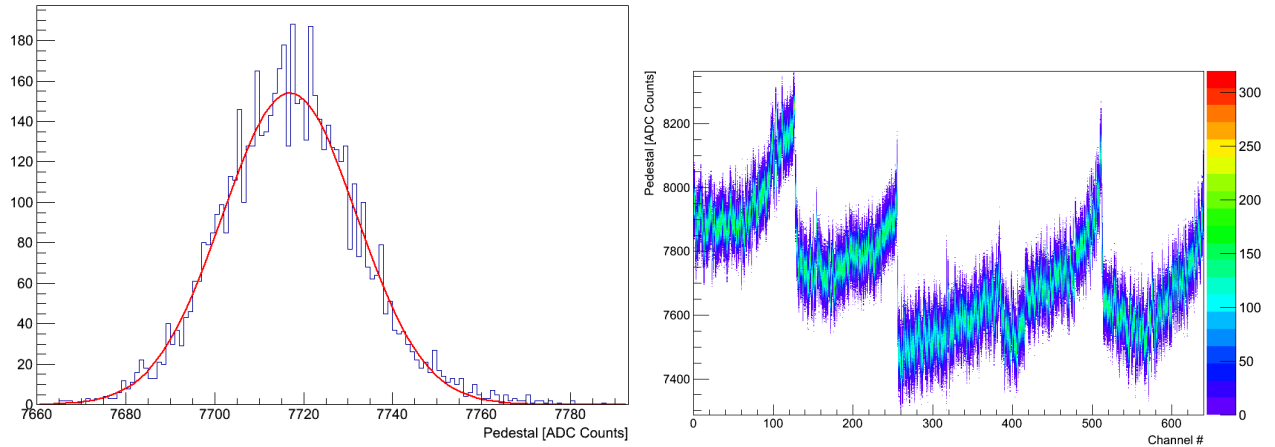


FIG. 46. Distribution of baseline values for a single readout channel. The distribution of all baseline values for a single hybrid is displayed on the plot to the right.

finding the RMS of each of the pedestal distributions. Figure 47 shows the noise charge as a function of channel number for a single hybrid. One thing to note is the large noise values at each of the chip edges. This has also been observed by the CMS collaboration and the cause is still under investigation.

The internal calibration circuitry of the APV25s allows for pre-determined signals of known charge to be injected into all channels of the APV25s. This allows for an accurate response determination by fitting the six pedestal subtracted samples using an ideal CR-RC shape. Examples of the shaper fit and amplitude distributions are shown in Figure 48.

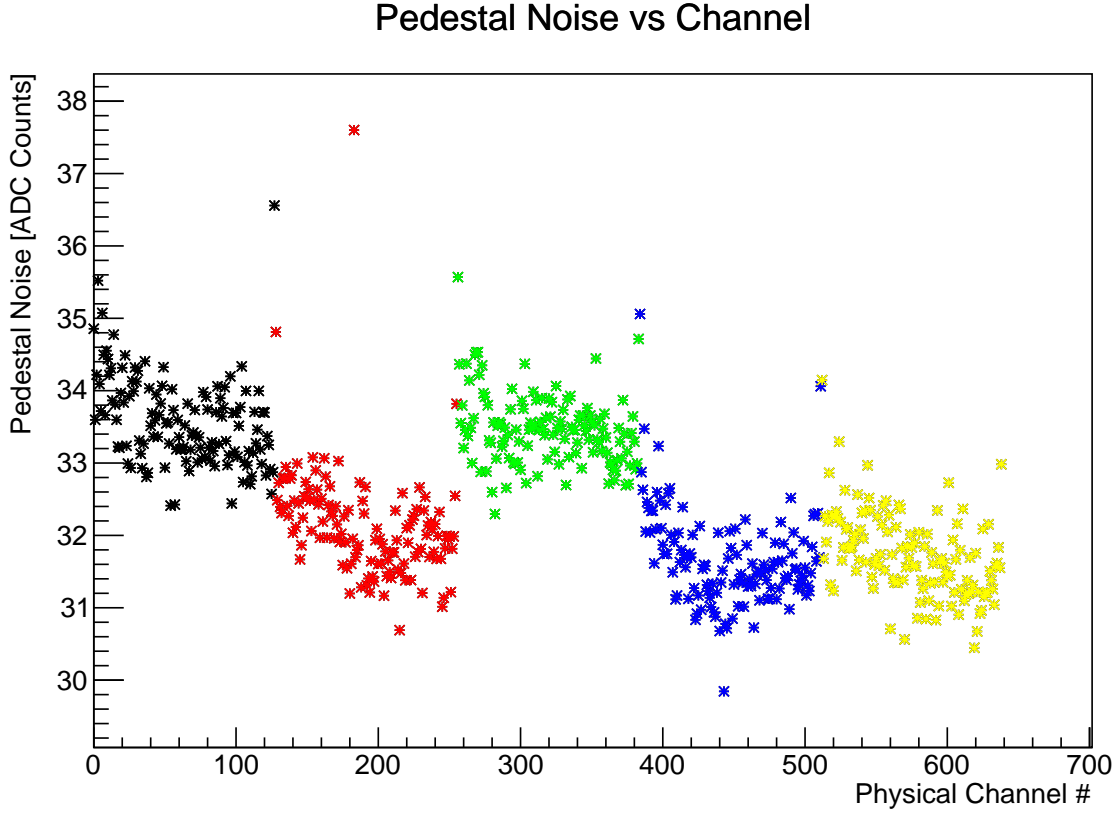


FIG. 47. Noise charge as a function of channel number for a single hybrid. Here the different colors denote a different AVP25.

The response scale obtained with the internal calibration circuitry was cross-checked with ionization source measurements.

Channel gains were then extracted by linearly fitting the response as a function of input charge as shown in Figure 49. Since the amount of charge deposited by a minimally ionizing charge particle in  $300\ \mu\text{m}$  of Si is on the order of 25,000 electrons (1 MIP), the fit was done up to a charge of 27,500 electrons. The gain has been previously shown to be linear up to approximately 3 MIPs [88].

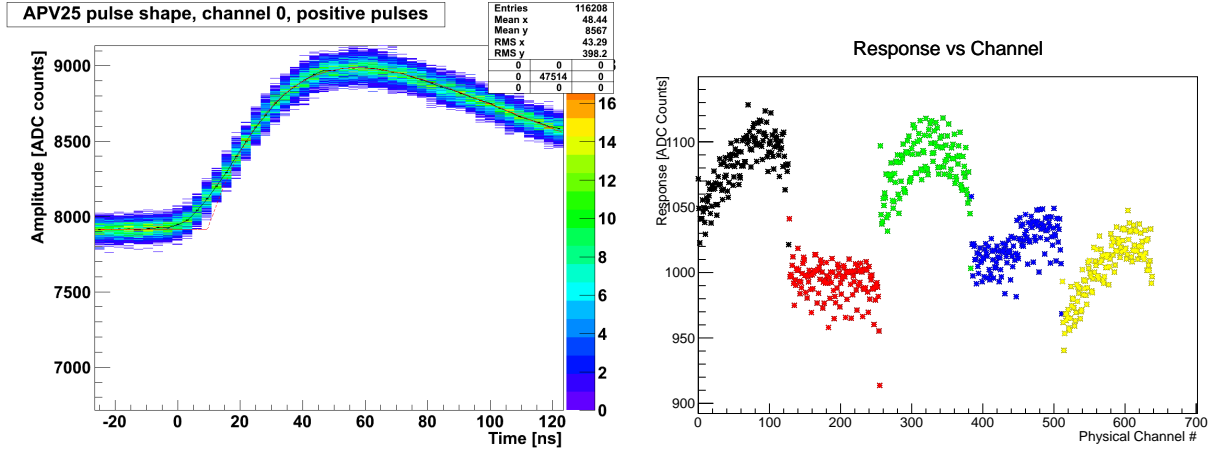


FIG. 48. The six samples which are readout are fit using an ideal CR-RC shape as shown on the left. The pedestal subtracted response extracted from the fit for each readout channel from a hybrid is shown on the right.

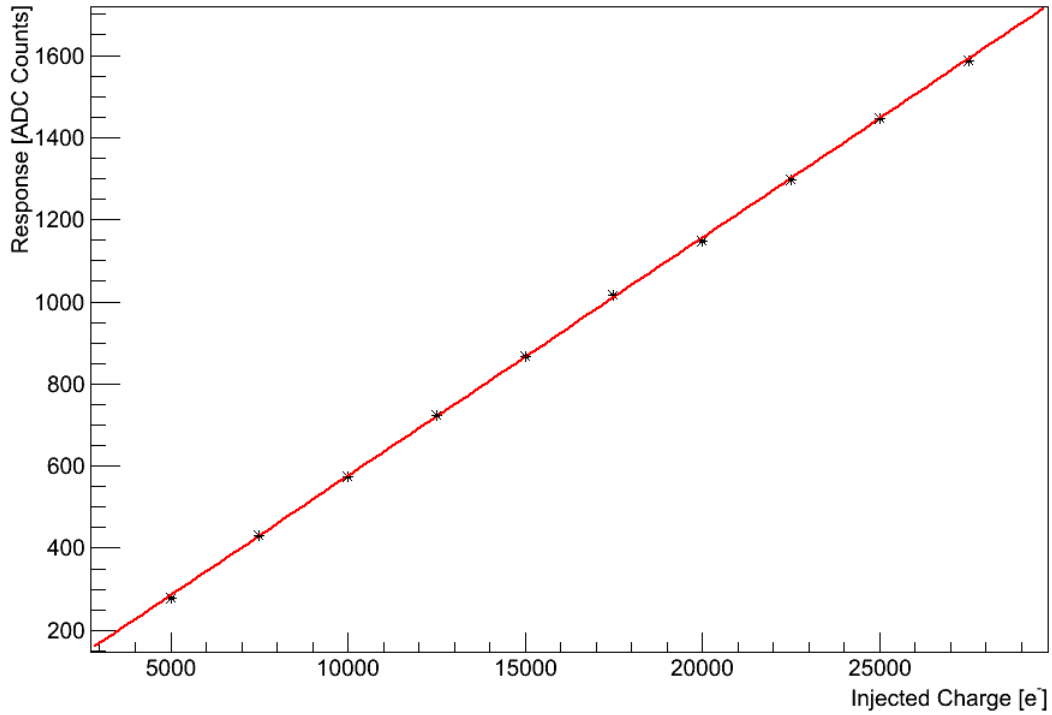


FIG. 49. Fit of response as a function of charge over a range of 0 to 27,000 electrons. Over this region the behavior had been previously found to be linear.

### 6.3.2. SVT Performance

The first data taken with the HPS Test Run Experiment has already demonstrated that the Silicon Vertex Tracker is working well. Preliminary data is shown below. By the time of the PAC 39 meeting, we hope to have thorough studies of the tracker performance, including tracking efficiencies, occupancies, and momentum and vertexing resolutions.

In Section 6.3.1 on SVT Calibrations above, we have already shown distributions of pedestals, noise, and pulse shapes from calibration signals, roughly matched in amplitude to detected charged particles. In rough terms, a typical pedestal rms is 30-35 ADC counts, and the peak signal from a minimum ionizing particle (MIP) in the data is roughly 700, which demonstrates good signal to noise. Internal calibrations of the gain show very good linearity up to about 3 MIPs. This performance should guarantee full efficiency and excellent spatial resolution in the tracker.

The average pulse shape development in our test run data, determined from the 6 separate time bins which are read out for each hit, is shown in Figure 50 below. Besides showing the size of the MIPS signal, it also demonstrates that the FADC trigger has been timed correctly to capture the silicon microstrip data. It is possible to determine the time of passage of a particle, called  $t_0$ , by fitting the observed shape to the known response function. A time resolution of a few nanoseconds should be possible, which will provide a powerful rejection of out of time hits in the tracker. Figure 51 shows the observed values of  $t_0$  for channels in one hybrid in the SVT.

In the photon run data, the average number of silicon hits per layer in the top half of the detector (the top half of the ECal provided the trigger for this data) is shown in Figure 52. The distribution of observed cluster sizes is given in Figure 53. Most clusters have one or two strips hits, but there is a small tail of clusters which have many strips hit.

Track reconstruction in the early data does not yet have the benefit of good detector alignment constants, but is already detecting and fitting tracks and estimating track momenta and angles. With our first trigger, which simply requires an energy deposition in the top half of the Ecal, we find tracks in roughly 25% of events, and two tracks in 0.5% of events. The present trigger rate is largely due to photons and electrons which are produced upstream of our nominal target (the pair spectrometer foil) in the upstream collimators, and may include many photons which would explain these low fractions.

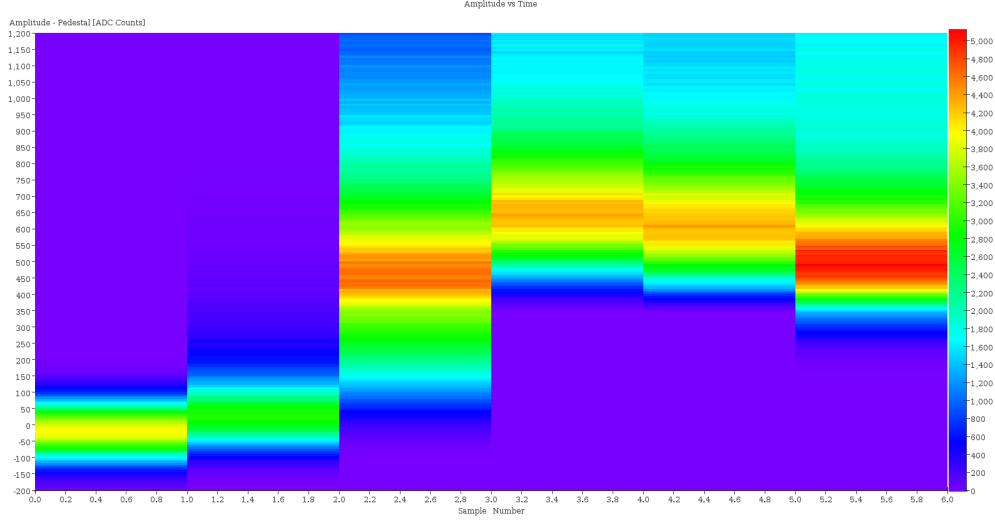


FIG. 50. Time development of the observed silicon output pulse, showing the pulse heights of six consecutive time buckets from the SVT, pedestal subtracted.

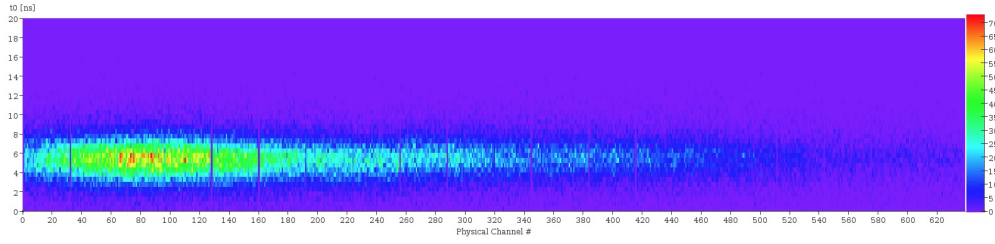


FIG. 51.  $t_0$  vs channel number in one silicon module in the test run data. Notice the good resolution and uniform response across the entire module.

Figure 54 shows the reconstructed momentum of tracks observed in the SVT. The fall-off below 0.4 GeV is likely due to the fact that lower momentum electrons or positrons will be swept past the Ecal acceptance. Much of the photon flux is concentrated at 2 GeV, because coherent bremsstrahlung is generated on the diamond crystal radiator. This may account for the fall off in the charged particle spectrum above 2 GeV. An event picture of a reconstructed track is shown in Figure 55. One sees hits in both the axial and stereo layers in the YZ view, and a single hit, corresponding to the intersection of the axial and stereo hits, in the XZ view, which clearly shows the trajectory bending in the magnetic field.

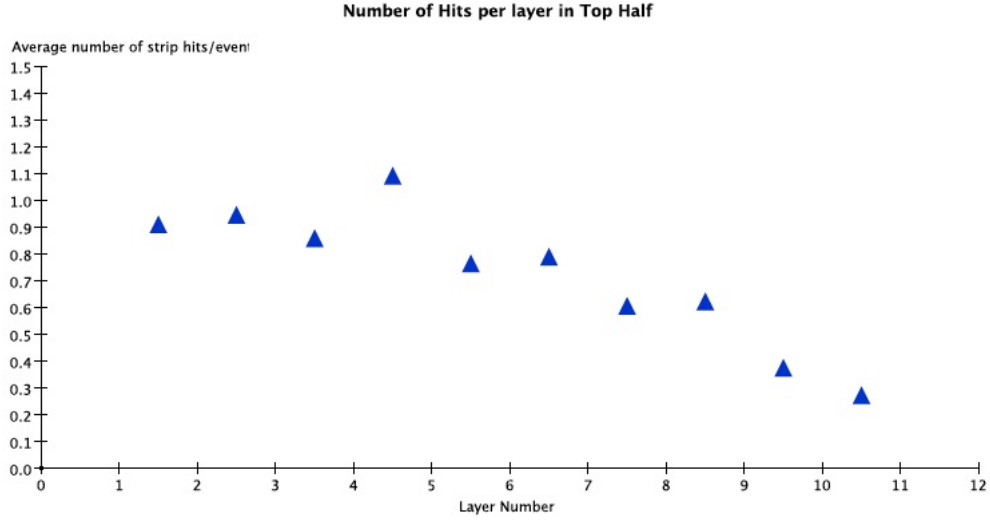


FIG. 52. Average number of strip hits per layer vs layer number in the top half of the SVT.

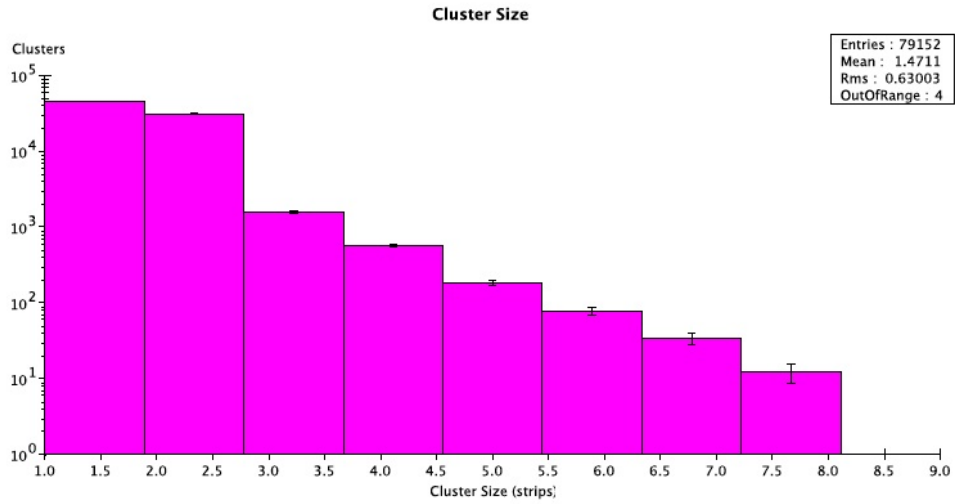


FIG. 53. Distribution of the cluster size, i.e. the number of strips/cluster, in the SVT.

### 6.3.3. ECal Calibration and Monitoring

ECal data are readout from FADCs in the so-called window mode, in which the 12-bit ADC values (0.25mV/ADC-channel) are summed together for 35 consecutive 4ns bins for each channel. Summation starts when the pulse crosses a given threshold value, which is entered as an external parameter. The program sums 30 samples after the crossing and 5



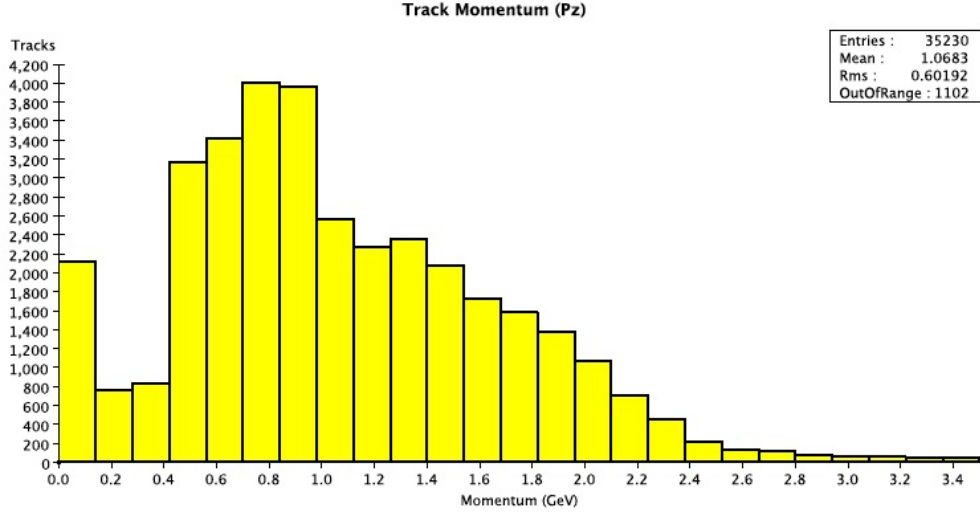


FIG. 54. Distribution of the cluster size, i.e. the number of strips/cluster, in the SVT.

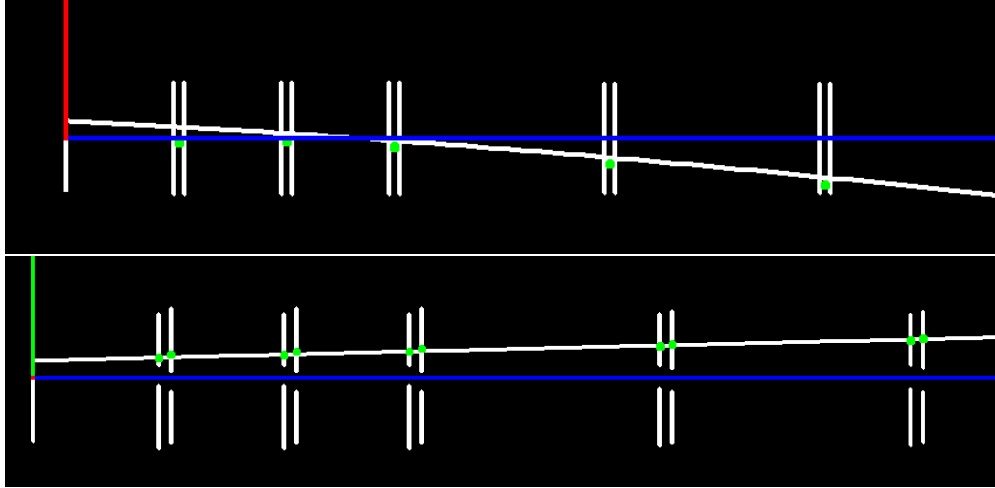


FIG. 55. Display of a single track fitting in the SVT.

before. In order to set the readout window width and the location (relative to the trigger time), data were taken with a pulser. In this mode, a fixed window of 100 samples relative to the trigger is read out for every crystal, see Figure 56. As can be seen from the figure, pulses are within the window size of 30-samples. By observing the pulse position in the window, this data can be used to adjust the trigger latency. Using a window before the trigger time, these data are used to calibrate the pedestals and noise of the ECal channels. In Figure 57, the RMS (top) and mean (middle) of fitted pedestal distributions for each channel are

shown. The pulse height in a particular channel is displayed on the bottom. Note that some of the ECal channels were disabled at the time of this data taking.

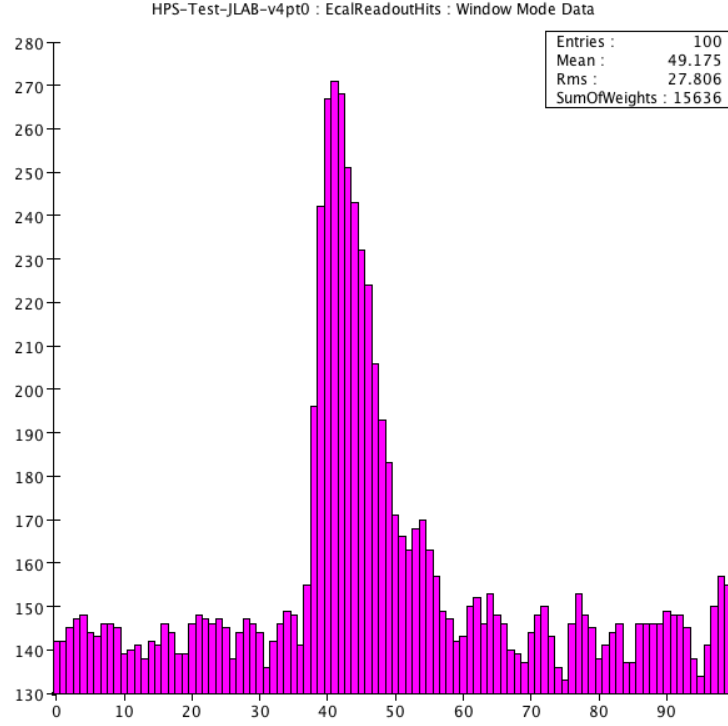


FIG. 56. ECal pulse viewed in window mode (100-sample window, corresponding to 400 ns). This data, which can be displayed live in the monitoring software, contains information on pedestal, noise, pulse shape, and trigger latency.

Calibration of the ECal FADCs (integrated ADC values vs. GeV) will be done offline using the fitted momentum of electron and positron tracks from the SVT.

#### 6.3.4. ECal trigger calibration

Studies of the trigger system have been performed using different trigger parameter settings. The most critical of these are the thresholds of the ADC value for a single hit that gets reported to the CTP and of the value of the cluster energy. Several online monitoring tools have been developed to aid these studies. In Figure 58 an occupancy map for the ECal is shown. Event-by-event display of cluster position and energy is presented in Figure 59 (top), and energy distributions for individual channels (bottom).

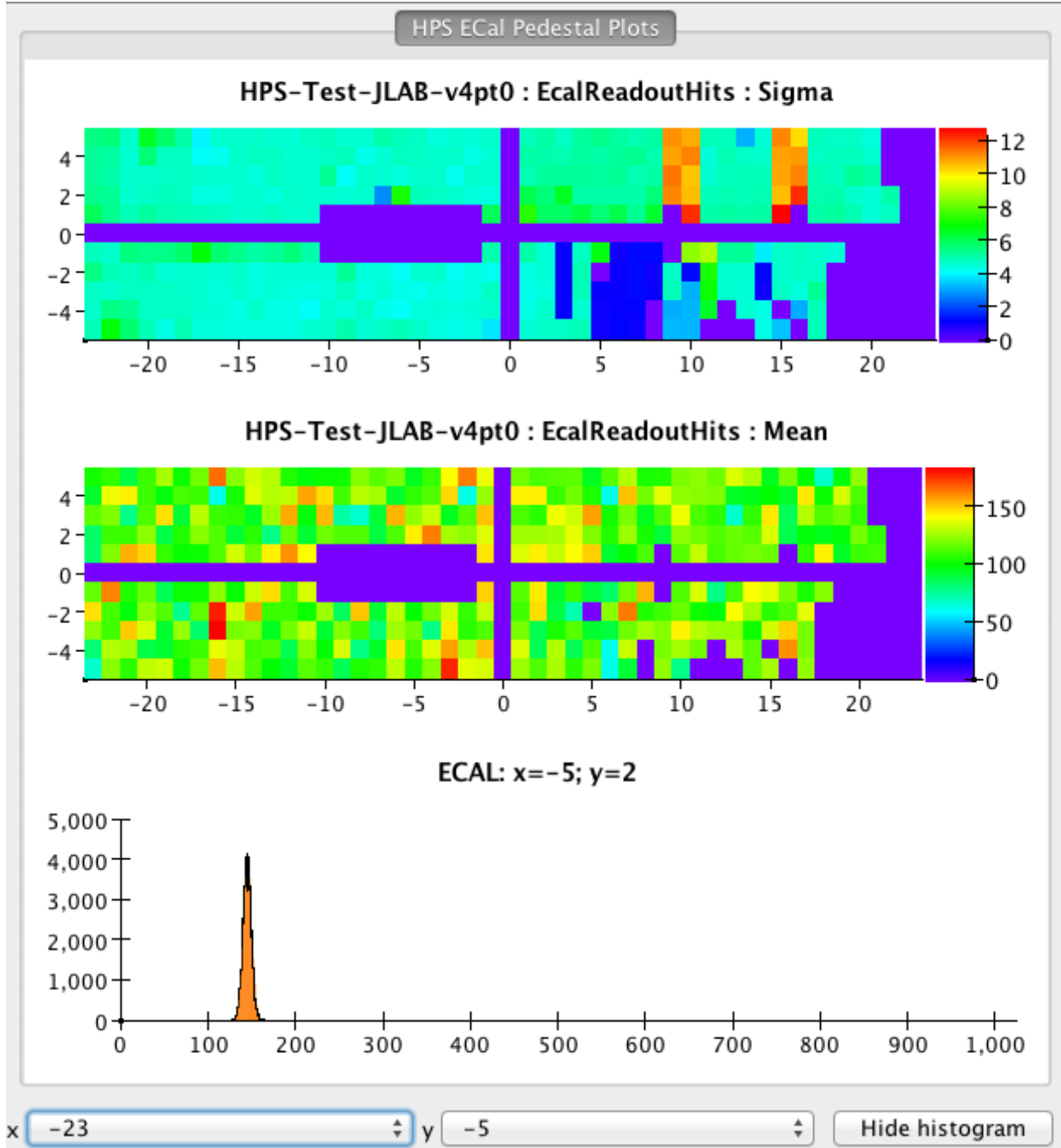


FIG. 57. On-line display shows the mean and standard deviation of window-mode data. Only samples from before the trigger are histogrammed, so this gives the pedestal and noise of the ECal channels. These values can be used in the FADC thresholds.

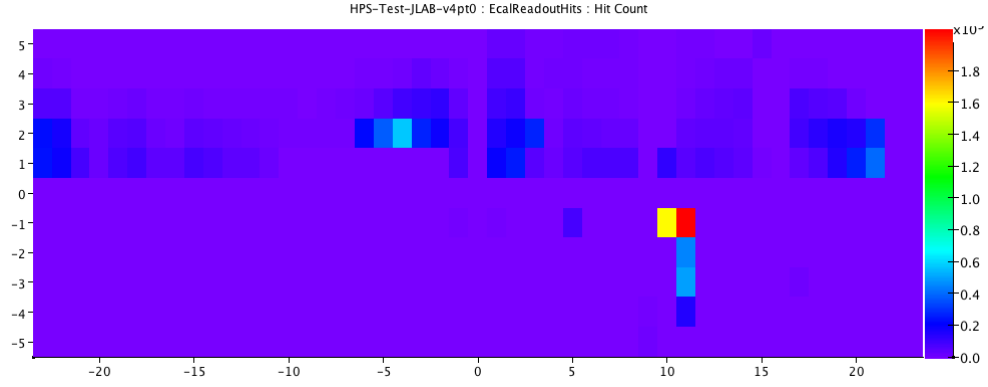


FIG. 58. Live display of ECal hit counts.

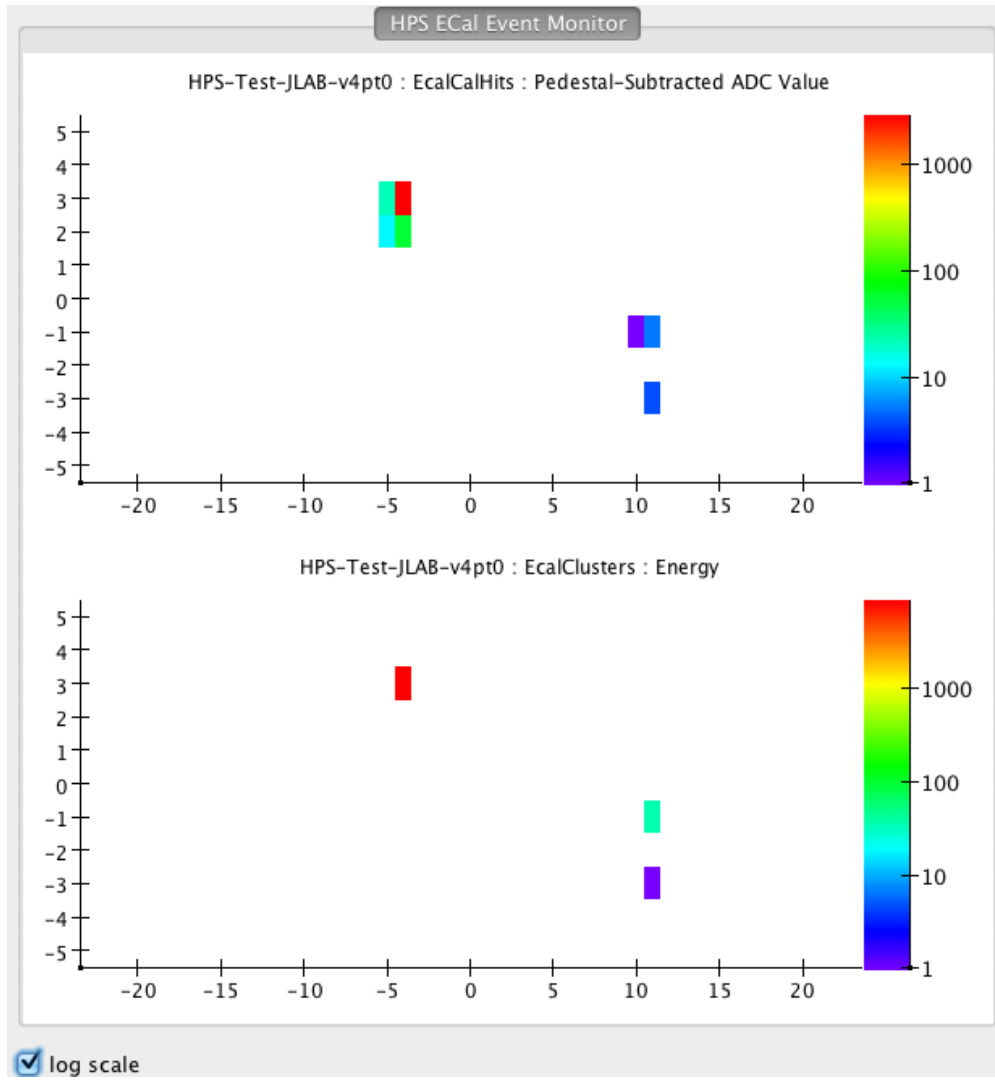


FIG. 59. Live event display — ECal hits on top, clusters on bottom.

## 7. REQUESTED ACTION AND FUTURE PLANS

We have made excellent progress since PAC 37's approval of the HPS Test Run in designing, building, installing, commissioning, and running the experiment. At the time of writing, we have just moved to successful data taking in the HDice photon beam and are beginning to study the HPS Test Run experiments performance in detail.

Some of the conditions placed on us by PAC 37 before granting full approval have already been addressed. We have fully demonstrated technical readiness of what is a rather sophisticated and high tech detector and data acquisition system. Silicon modules have been produced in record time, tested, qualified, and incorporated into the Silicon Vertex Tracker. A new high speed DAQ for the SVT has been developed and commissioned and is now fully operable, including the development of a new hybrid for the APV25 readout chip. The tracker has been adapted to work in vacuum and inside a magnetic field, with special attention to vacuum and magnet compatible materials, and with a cooling system and motion controls operable in vacuum as well. The entire SVT system has been successfully commissioned, and early demonstrations of its performance are included in this report. Triggering HPS is an equally challenging problem, which has also reached full and successful demonstration. A new  $PbWO_4$  electromagnetic calorimeter has been assembled and read out with JLAB's new 250MHz FADC system. A sophisticated new trigger, which makes full use of the FADC amplitude and timing information and the fine spatial segmentation of the calorimeter, has been developed, tested, and implemented. It is successfully triggering the experiments first data taking. Finally, a simulation/reconstruction/analysis framework has been put into place which allows online monitoring of HPS Test and analysis of our first data. Tracking and calorimeter reconstruction codes already exist, a full trigger simulation has been developed, and analysis is underway.

HPS requires very small and stable beam spots, and beams with very little halo so the silicon detectors can be placed close to the beams and acceptance maximized. At the time of our PAC 37 proposal, such beams had not been demonstrated in Hall B. Since then however, as described above in Section 4, optics codes have generated the required beamline magnet settings, and extremely high quality electron beams delivered in Hall B. The beam size, beam halo, and beam stability requirements have been demonstrated, removing another technical contingency.

The HPS data acquisition systems for the ECal and SVT transfer data at very high rates in normal operation. The ECal FADCs record data at 250 MHz and the SVT DAQ at 40 MHz. We have demonstrated that the full ECal + SVT system can read, transfer, and write data at few kHz trigger rates, but demonstrating that 30-40kHz rates are possible is still ahead of us. We believe this demonstration is easily within reach and expect to show this capability by the time of the PAC 39 meeting, removing another technical hurdle.

The major remaining experimental uncertainties concern the occupancy rates in the silicon detectors and the trigger rates in the ecal. As discussed above in the Introduction, these issues are most compellingly addressed with electron beam running, but scheduling conflicts have not yet permitted such running. In electron running, the tails of the multiple Coulomb scattering of beam electrons is responsible for the bulk of the occupancy in the silicon microstrip detectors and that in the ECal. These high occupancies contribute to tracking pattern recognition errors in the SVT and high trigger rates in the Ecal. These effects have been thoroughly studied with both EGS5 and GEANT4, which have been used to assess the HPS reach, but they disagree at the level of a factor of 2, and we would like to check them experimentally. With photon running conditions, it will be possible to study the scattering of the electrons and positrons that are pair-produced in the pair spectrometer foil targets, make detailed comparisons with EGS5 and GEANT4 predictions, and understand the role multiple Coulomb scattering plays. Electron-positron pairs are primarily produced in the plane perpendicular to the pair spectrometers magnetic field, and it is only by virtue of small opening angle effects in their production and multiple Coulomb scattering in the target, that they enter the HPS Test Run acceptance. So studies of their angular distributions will provide us valuable information. We plan to present this analysis at the PAC 39 meeting.

With technical feasibility already shown, and with new data in hand at the time of the PAC 39 meeting which demonstrates our understanding of detector occupancy and trigger rates, we will have satisfied the contingencies placed on approving full HPS by PAC 37 and will request full approval of HPS.

Once the contingencies have been addressed, it is important that full approval be granted in a timely way. There is likely an opportunity to run in Hall B early in the 12 GeV era, before CLAS12 is ready to install. HPS would like to be ready to take advantage of this opportunity. To proceed to full HPS, the HPS Collaboration must submit a full and detailed

proposal to DOE HEP which must be reviewed and funded before work can start in earnest. With PAC approval granted in June, a proposal could be submitted this Fall, reviewed next Winter 2013, and funded next Spring. That would leave us two years for engineering design, construction, testing, and installation for a 12 GeV run in 2015, which is adequate. Timely approval would also let HPS maintain the considerable momentum developed over the past year as we produced a technically sophisticated detector and conducted a successful test run in a very short time. Perhaps most importantly, timely approval is needed to remain competitive in what has become an exciting and competitive search for new physics at the Intensity Frontier.

- 
- [1] A. Grillo *et al.* [HPS Collaboration], HPS Proposal to JLab PAC37 PR-11-006, [http://www.jlab.org/exp\\_prog/PACpage/PAC37/proposals/Proposals/](http://www.jlab.org/exp_prog/PACpage/PAC37/proposals/Proposals/)
  - [2] A. Grillo *et al.* [HPS Collaboration], HPS Test Run Proposal to DOE, <https://confluence.slac.stanford.edu/display/hpsg/Project+Overview>
  - [3] M. Kamionkowski, S. M. Koushiappas and M. Kuhlen, Phys. Rev. D **81**, 043532 (2010) [arXiv:1001.3144 [astro-ph.GA]].
  - [4] R. Essig, P. Schuster, N. Toro and B. Wojtsekhowski, JHEP **1102**, 009 (2011) [arXiv:1001.2557 [hep-ph]].
  - [5] S. Abrahamyan *et al.* [APEX Collaboration], Phys. Rev. Lett. **107**, 191804 (2011) [arXiv:1108.2750 [hep-ex]].
  - [6] H. Merkel *et al.* [A1 Collaboration], Phys. Rev. Lett. **106**, 251802 (2011) [arXiv:1101.4091 [nucl-ex]].
  - [7] M. Freytsis, G. Ovanessian and J. Thaler, “Dark Force Detection in Low Energy E-P Collisions,” JHEP **1001** (2010) 111 [arXiv:0909.2862 [hep-ph]].
  - [8] B. Holdom, “Two U(1)’s and Epsilon Charge Shifts,” Phys. Lett. B **166** (1986) 196.
  - [9] P. Galison and A. Manohar, “Two Z’s Or Not Two Z’s?,” Phys. Lett. B **136** (1984) 279.
  - [10] R. Essig, P. Schuster and N. Toro, “Probing Dark Forces and Light Hidden Sectors at Low-Energy  $e^+e^-$  Colliders,” Phys. Rev. D **80** (2009) 015003 [arXiv:0903.3941 [hep-ph]].
  - [11] M. Goodsell, J. Jaeckel, J. Redondo and A. Ringwald, “Naturally Light Hidden Photons in LARGE Volume String Compactifications,” JHEP **0911**, 027 (2009) [arXiv:0909.0515 [hep-ph]].
  - [12] M. Cicoli, M. Goodsell, J. Jaeckel and A. Ringwald, “Testing String Vacua in the Lab: From a Hidden CMB to Dark Forces in Flux Compactifications,” JHEP **1107**, 114 (2011) [arXiv:1103.3705 [hep-th]].
  - [13] M. Goodsell, S. Ramos-Sanchez and A. Ringwald, “Kinetic Mixing of U(1)s in Heterotic Orbifolds,” JHEP **1201**, 021 (2012) [arXiv:1110.6901 [hep-th]].
  - [14] M. Goodsell and A. Ringwald, “Light hidden-sector U(1)s in string compactifications,” Fortsch. Phys. **58**, 716 (2010) [arXiv:1002.1840 [hep-th]].
  - [15] P. Candelas, G. T. Horowitz, A. Strominger and E. Witten, “Vacuum Configurations for



- Superstrings,” Nucl. Phys. B **258**, 46 (1985).
- [16] E. Witten, “New Issues in Manifolds of SU(3) Holonomy,” Nucl. Phys. B **268**, 79 (1986).
  - [17] S. Andreas, M. D. Goodsell and A. Ringwald, “Dark matter and Dark Forces from a supersymmetric hidden sector,” arXiv:1109.2869 [hep-ph].
  - [18] J. Jaeckel and A. Ringwald, “The Low-Energy Frontier of Particle Physics,” Ann. Rev. Nucl. Part. Sci. **60**, 405 (2010) [arXiv:1002.0329 [hep-ph]].
  - [19] P. Fayet, “U-Boson Production in  $E^+ E^-$  Annihilations, Psi and Upsilon Decays, and Light Dark Matter,” Phys. Rev. D **75** (2007) 115017 [arXiv:hep-ph/0702176].
  - [20] C. Cheung, J. T. Ruderman, L. T. Wang and I. Yavin, “Kinetic Mixing as the Origin of Light Dark Scales,” Phys. Rev. D **80** (2009) 035008 [arXiv:0902.3246 [hep-ph]].
  - [21] N. Arkani-Hamed and N. Weiner, JHEP **0812**, 104 (2008) [arXiv:0810.0714 [hep-ph]].
  - [22] D. E. Morrissey, D. Poland and K. M. Zurek, “Abelian Hidden Sectors at a GeV,” JHEP **0907** (2009) 050 [arXiv:0904.2567 [hep-ph]].
  - [23] J. D. Bjorken, R. Essig, P. Schuster and N. Toro, Phys. Rev. D **80**, 075018 (2009) [arXiv:0906.0580 [hep-ph]].
  - [24] M. Pospelov, “Secluded U(1) Below the Weak Scale,” Phys. Rev. D **80** (2009) 095002 [arXiv:0811.1030 [hep-ph]].
  - [25] N. Arkani-Hamed, D. P. Finkbeiner, T. R. Slatyer and N. Weiner, “A Theory of Dark Matter,” Phys. Rev. D **79** (2009) 015014 [arXiv:0810.0713 [hep-ph]].
  - [26] M. Pospelov and A. Ritz, “Astrophysical Signatures of Secluded Dark Matter,” Phys. Lett. B **671** (2009) 391 [arXiv:0810.1502 [hep-ph]].
  - [27] E. Komatsu *et al.* [WMAP Collaboration], Astrophys. J. Suppl. **192**, 18 (2011) [arXiv:1001.4538 [astro-ph.CO]]; D. J. Eisenstein *et al.* [SDSS Collaboration], Astrophys. J. **633**, 560 (2005) [astro-ph/0501171]; S. Perlmutter *et al.* [Supernova Cosmology Project Collaboration], Astrophys. J. **517**, 565 (1999) [astro-ph/9812133]; A. G. Riess *et al.* [Supernova Search Team Collaboration], Astron. J. **116**, 1009 (1998) [astro-ph/9805201]; M. Kowalski *et al.* [Supernova Cosmology Project Collaboration], Astrophys. J. **686**, 749 (2008) [arXiv:0804.4142 [astro-ph]].
  - [28] O. Adriani *et al.* [PAMELA Collaboration], Nature **458**, 607 (2009) [arXiv:0810.4995 [astro-ph]].
  - [29] M. Ackermann *et al.* [Fermi LAT Collaboration], Phys. Rev. D **82**, 092004 (2010)

- [arXiv:1008.3999 [astro-ph.HE]].
- [30] J. Chang, J. H. Adams, H. S. Ahn, G. L. Bashindzhagyan, M. Christl, O. Ganel, T. G. Guzik and J. Isbert *et al.*, *Nature* **456**, 362 (2008).
  - [31] F. Aharonian *et al.* [H.E.S.S. Collaboration], *Phys. Rev. Lett.* **101**, 261104 (2008) [arXiv:0811.3894 [astro-ph]].
  - [32] F. Aharonian *et al.* [H.E.S.S. Collaboration], *Astron. Astrophys.* **508**, 561 (2009) [arXiv:0905.0105 [astro-ph.HE]].
  - [33] O. Adriani *et al.* [PAMELA Collaboration], *Phys. Rev. Lett.* **106**, 201101 (2011) [arXiv:1103.2880 [astro-ph.HE]].
  - [34] M. Ackermann *et al.* [The Fermi LAT Collaboration], *Phys. Rev. Lett.* **108**, 011103 (2012) [arXiv:1109.0521 [astro-ph.HE]].
  - [35] M. Cirelli, M. Kadastik, M. Raidal and A. Strumia, *Nucl. Phys. B* **813**, 1 (2009) [arXiv:0809.2409 [hep-ph]].
  - [36] I. Cholis, D. P. Finkbeiner, L. Goodenough and N. Weiner, *JCAP* **0912**, 007 (2009) [arXiv:0810.5344 [astro-ph]].
  - [37] I. Cholis, G. Dobler, D. P. Finkbeiner, L. Goodenough and N. Weiner, *Phys. Rev. D* **80**, 123518 (2009) [arXiv:0811.3641 [astro-ph]].
  - [38] D. P. Finkbeiner, L. Goodenough, T. R. Slatyer, M. Vogelsberger and N. Weiner, *JCAP* **1105**, 002 (2011) [arXiv:1011.3082 [hep-ph]].
  - [39] T. R. Slatyer, N. Toro and N. Weiner, arXiv:1107.3546 [hep-ph].
  - [40] O. Adriani, G. C. Barbarino, G. A. Bazilevskaya, R. Bellotti, M. Boezio, E. A. Bogomolov, L. Bonechi and M. Bongi *et al.*, *Phys. Rev. Lett.* **102**, 051101 (2009) [arXiv:0810.4994 [astro-ph]].
  - [41] M. Ackermann *et al.* [Fermi-LAT Collaboration], *Phys. Rev. Lett.* **107**, 241302 (2011) [arXiv:1108.3546 [astro-ph.HE]].
  - [42] M. D. Kistler and J. M. Siegal-Gaskins, *Phys. Rev. D* **81**, 103521 (2010) [arXiv:0909.0519 [astro-ph.HE]]. K. N. Abazajian, S. Blanchet and J. P. Harding, *Phys. Rev. D* **85**, 043509 (2012) [arXiv:1011.5090 [hep-ph]].
  - [43] M. Papucci and A. Strumia, *JCAP* **1003**, 014 (2010) [arXiv:0912.0742 [hep-ph]].
  - [44] G. Hutsi, A. Hektor and M. Raidal, *JCAP* **1007**, 008 (2010) [arXiv:1004.2036 [astro-ph.HE]].
  - [45] A. A. Abdo *et al.* [Fermi-LAT Collaboration], *JCAP* **1004**, 014 (2010) [arXiv:1002.4415 [astro-

- ph.CO]]. J. Zavala, M. Vogelsberger, T. R. Slatyer, A. Loeb and V. Springel, Phys. Rev. D **83**, 123513 (2011) [arXiv:1103.0776 [astro-ph.CO]].
- [46] X. Huang, G. Vertongen and C. Weniger, JCAP **1201**, 042 (2012) [arXiv:1110.1529 [hep-ph]].
- [47] S. Galli, F. Iocco, G. Bertone and A. Melchiorri, Phys. Rev. D **80**, 023505 (2009) [arXiv:0905.0003 [astro-ph.CO]]; T. R. Slatyer, N. Padmanabhan and D. P. Finkbeiner, Phys. Rev. D **80**, 043526 (2009) [arXiv:0906.1197 [astro-ph.CO]]; S. Galli, F. Iocco, G. Bertone and A. Melchiorri, Phys. Rev. D **84**, 027302 (2011) [arXiv:1106.1528 [astro-ph.CO]]; D. P. Finkbeiner, S. Galli, T. Lin and T. R. Slatyer, Phys. Rev. D **85**, 043522 (2012) [arXiv:1109.6322 [astro-ph.CO]].
- [48] L. Pieri, J. Lavalle, G. Bertone and E. Branchini, Phys. Rev. D **83**, 023518 (2011) [arXiv:0908.0195 [astro-ph.HE]].
- [49] M. D. Kistler and J. M. Siegal-Gaskins, Phys. Rev. D **81**, 103521 (2010) [arXiv:0909.0519 [astro-ph.HE]].
- [50] R. Bernabei *et al.* [DAMA and LIBRA Collaborations], Eur. Phys. J. C **67**, 39 (2010) [arXiv:1002.1028 [astro-ph.GA]].
- [51] C. E. Aalseth *et al.* [CoGeNT Collaboration], Phys. Rev. Lett. **106**, 131301 (2011) [arXiv:1002.4703 [astro-ph.CO]].
- [52] C. E. Aalseth, P. S. Barbeau, J. Colaresi, J. I. Collar, J. Diaz Leon, J. E. Fast, N. Fields and T. W. Hossbach *et al.*, Phys. Rev. Lett. **107**, 141301 (2011) [arXiv:1106.0650 [astro-ph.CO]].
- [53] G. Angloher, M. Bauer, I. Bavykina, A. Bento, C. Bucci, C. Ciemniak, G. Deuter and F. von Feilitzsch *et al.*, arXiv:1109.0702 [astro-ph.CO].
- [54] Z. Ahmed *et al.* [CDMS-II Collaboration], Phys. Rev. Lett. **106**, 131302 (2011) [arXiv:1011.2482 [astro-ph.CO]]. Z. Ahmed *et al.* [CDMS Collaboration], arXiv:1203.1309 [astro-ph.CO].
- [55] J. Angle *et al.* [XENON10 Collaboration], Phys. Rev. Lett. **107**, 051301 (2011) [arXiv:1104.3088 [astro-ph.CO]].
- [56] E. Aprile *et al.* [XENON100 Collaboration], Phys. Rev. Lett. **107**, 131302 (2011) [arXiv:1104.2549 [astro-ph.CO]].
- [57] C. Kelso, D. Hooper and M. R. Buckley, Phys. Rev. D **85**, 043515 (2012) [arXiv:1110.5338 [astro-ph.CO]].
- [58] J. D. Bjorken *et al.*, “Search for Neutral Metastable Penetrating Particles Produced in the

- SLAC Beam Dump,” *Phys. Rev. D* **38** (1988) 3375.
- [59] E. M. Riordan *et al.*, “A Search for Short Lived Axions in an Electron Beam Dump Experiment,” *Phys. Rev. Lett.* **59** (1987) 755.
  - [60] A. Bross, M. Crisler, S. H. Pordes, J. Volk, S. Errede and J. Wrbanek, “A Search for Shortlived Particles Produced in an Electron Beam Dump,” *Phys. Rev. Lett.* **67** (1991) 2942.
  - [61] KLOE-2 Collaboration, “Search for a Vector Gauge Boson in Phi Meson Decays with the KLOE Detector,” *Phys. Lett. B* **706** (2012) 251 [arXiv:1110.0411 [hep-ex]].
  - [62] M. Reece and L. T. Wang, “Searching for the Light Dark Gauge Boson in GeV-Scale Experiments,” *JHEP* **0907** (2009) 051 [arXiv:0904.1743 [hep-ph]].
  - [63] B. Aubert *et al.* [BABAR Collaboration], *Phys. Rev. Lett.* **103**, 081803 (2009) [arXiv:0905.4539 [hep-ex]].
  - [64] J. B. Dent, F. Ferrer and L. M. Krauss, “Constraints on Light Hidden Sector Gauge Bosons from Supernova Cooling,” arXiv:1201.2683 [astro-ph.CO].
  - [65] M. Deutsch, *Phys. Rev.* **82**, 455 (1951).
  - [66] J. I. Friedman and V. L. Telegdi, *Phys. Rev.* **105**, 1681 (1957).
  - [67] V. W. Hughes, D. W. McColm, K. Ziock and R. Prepost, *Phys. Rev. Lett.* **5**, 63 (1960).
  - [68] E. Holvik and H. A. Olsen, *Phys. Rev. D* **35**, 2124 (1987).
  - [69] N. Arteaga-Romero, C. Carimalo and V. G. Serbo, *Phys. Rev. A* **62**, 032501 (2000) [hep-ph/0001278].
  - [70] S. J. Brodsky and R. F. Lebed, *Phys. Rev. Lett.* **102**, 213401 (2009) [arXiv:0904.2225 [hep-ph]].
  - [71] S. M. Bilenky, V. H. Nguyen, L. L. Nemenov and F. G. Tkebuchava, *Yad. Fiz.* **10**, 812 (1969).
  - [72] V. W. Hughes and B. Maglic, *Bull. Am. Phys. Soc.* **16**, 65 (1971).
  - [73] J. Malenfant, *Phys. Rev. D* **36**, 863 (1987).
  - [74] S. G. Karshenboim, U. D. Jentschura, V. G. Ivanov and G. Soff, *Phys. Lett. B* **424**, 397 (1998).
  - [75] D. A. Owen and W. W. Repko, *Phys. Rev. A* **5**, 1570 (1972).
  - [76] U. D. Jentschura, G. Soff, V. G. Ivanov and S. G. Karshenboim, hep-ph/9706401.
  - [77] U. D. Jentschura, G. Soff, V. G. Ivanov and S. G. Karshenboim, *Phys. Rev. A* **56**, 4483 (1997) [physics/9706026].
  - [78] S. G. Karshenboim, V. G. Ivanov, U. D. Jentschura and G. Soff, *J. Exp. Theor. Phys.* **86**, 226

- (1998) [Zh. Eksp. Teor. Fiz. **113**, 409 (1998)].
- [79] G. W. Bennett *et al.* [Muon G-2 Collaboration], Phys. Rev. D **73**, 072003 (2006) [hep-ex/0602035].
- [80] R. Pohl, A. Antognini, F. Nez, F. D. Amaro, F. Biraben, J. M. R. Cardoso, D. S. Covita and A. Dax *et al.*, Nature **466**, 213 (2010).
- [81] A. Banburski, and P. Schuster “Primary and Secondary True Muonium Production Yields for Fixed-Target Experiments” (to appear)
- [82] A. Banburski, “Discovering True Muonium Physics with Fixed-Target Experiments” APS Talk, March 31 2012, APR12-2012-020018
- [83] M. Borland, A Flexible SDDS-Compliant Code for Accelerator Simulation, ANL, Argonne, IL 60439, USA
- [84] <http://www.lcsim.org/software/slic/>
- [85] P. Billoir, R. Fruhwirth, and M. Regler, Nucl. Instr. And Meth. A241 (1985) 115.
- [86] . P. Billoir and S. Qian, Nucl. Instr. And Meth. A311 (1991) 139.
- [87] L. Jones, APV25-S1: User guide version 2.2, RAL Microelectronics Design Group, 2011.
- [88] M. Raymond et al., APV25 production testing and quality assurance, 8th Workshop on Electronics for LHC Experiments, Colmar, France, 9-13 Sep 2002